



DETERMINATION OF CLOUD  
PROPERTIES FROM BISPECTRAL  
SATELLITE MEASUREMENTS

LP-92

FINAL REPORT  
TWDB CONTRACT NO. 14-80026

Prepared by:

JERRY JURICA AND SHWE-YI CHI  
ATMOSPHERIC SCIENCE GROUP  
TEXAS TECH UNIVERSITY  
LUBBOCK, TEXAS

Prepared for:

TEXAS DEPARTMENT OF WATER RESOURCES  
AUSTIN, TEXAS

Funded by:

DEPARTMENT OF THE INTERIOR, BUREAU OF RECLAMATION  
TEXAS DEPARTMENT OF WATER RESOURCES

MARCH 1979

DETERMINATION OF CLOUD PROPERTIES  
FROM BISPECTRAL SATELLITE MEASUREMENTS

Gerald M. Jurica and Shwe-Yi Chi  
Texas Tech University  
Lubbock, Texas 79409

Final report prepared under TDWR Contract  
No. 14-06-D-7587 IAC(78-79) 1055

Prepared for  
Texas Department of Water Resources  
Austin, Texas  
and  
Bureau of Reclamation, Department of Interior  
Denver, Colorado

Texas Department of Water Resources  
LP-92  
March 1979

## ABSTRACT

An analysis technique is presented to determine cloud parameters from geostationary satellite data. The principal data source is visible and infrared radiance measurements from the Geostationary Operational Environmental Satellite (GOES). A critical brightness value to distinguish clouds from underlying non-cloud surfaces is determined as a primary factor to identify the cloud measurement spot. Percentage of cloud cover and number of clouds are analyzed and compared with results derived from photographic images. Through a cloud summary computer program, cloud size, maximum brightness, as well as mean and standard deviation of brightness value for every individual cloud are found, categorized, and compared in time series.

Infrared radiance data are used to determine the cloud top temperature, allowing cloud height to be obtained from corresponding rawinsonde data. Cloud movement is estimated by a subjective method based upon computer-generated plots of the satellite data. Comparing simultaneous visible and infrared data sets, cirrus clouds are detected as regions with high infrared radiance value and low visible radiance value. The analysis is done with all of these data sources to study the properties and patterns of clouds for a case study on 22 June 1976 in the Texas High Plains area.

Key words: Weather Modification, Cloud Properties, Satellite Measurement

TABLE OF CONTENTS

	Page
LIST OF TABLES . . . . .	iii
LIST OF FIGURES . . . . .	iv
1. INTRODUCTION . . . . .	1
1.1 Historical Background . . . . .	3
1.2 Literature Survey . . . . .	5
2. DATA PROCESSING PROCEDURES . . . . .	8
2.1 Data Transmission and Acquisition . . . . .	8
2.2 Visible Radiance Measurements . . . . .	19
2.3 Infrared Radiance Measurements. . . . .	26
2.4 Alignment of Visible and Infrared Data. . . . .	28
3. DATA ANALYSIS . . . . .	38
3.1 Cloud Properties . . . . .	38
3.1.1 Cloud populations and percent cloud cover . . . . .	39
3.1.2 Cloud brightness analysis . . . . .	51
3.2 Cloud Albedo Determination . . . . .	68
3.3 Cloud Height and Cirrus Detection . . . . .	73
3.4 Satellite-tracked Cloud Movement . . . . .	89
4. SUMMARY AND CONCLUSIONS . . . . .	96
LIST OF REFERENCES . . . . .	99

LIST OF TABLES

<u>Table</u>		<u>Page</u>
2-1	Solar zenith angle and visible radiance values used to distinguish clouds from the non-cloud background . . . . .	23
2-2	Time-averaged isotherm heights for the four rawinsonde stations in the study area. Also given are the averaged heights, the standard deviation of height and the maximum deviation from the average . . . . .	34
2-3	Weighting factors used in stretching infrared radiance data . . . . .	37
3-1	Comparison of numbers of clouds and percentage of cloud cover from satellite radiance data and imagery . . . . .	41
3-2	Number of clouds in various size categories .	46
3-3	Cumulative distribution of cloud size as a function of time during the study period . . .	47
3-4	Total percent cloud cover and the relative contribution from clouds of various diameters D (km) . . . . .	50
3-5	Mean brightness for total clouds and four different categories of clouds . . . . .	55
3-6	Cumulative distribution of cloud mean brightness above the critical cloud/non-cloud value.	59
3-7	Parameters for a regression line, of the form $y=a+bx$ , between standard deviation of brightness $y$ , and mean brightness, $x$ . . . . .	64
3-8	Satellite-derived values of maximum and minimum temperature and maximum cloud top height in the study area. Also given are observed maximum radar echo heights . . . . .	84
3-9	Percentage of study area having radiance temperatures (T) in various intervals (C). Corresponding heights (h) are given in meters.	86
3-10	The comparison of velocity components from images (Im), radiance data (Ri), radar summary charts (Rr), and sounding data (Sd). . . . .	92

LIST OF FIGURES

<u>Figure</u>		<u>Page</u>
2-1	Location and approximate operational coverage of the two satellite data sources: GOES WEST at 135° W and GOES EAST 75° W longitude . . . . .	9
2-2	The area of study. The sector at the center is the Texas HIPLEX study region . . . . .	11
2-3	Surface synoptic chart at 1200 GMT on 22 June 1976 . . . . .	14
2-4	500 mb weather map at 1200 GMT on 22 June 1976. Contours (solid lines) are given in decameters and isotherms (dashed lines) are given in Celsius degrees . . . . .	15
2-5	Radar summary charts from 1735 GMT 22 June to 0135 GMT 23 June 1976 . . . . .	15
2-6	Comparison of the theoretical and adjusted visible critical values . . . . .	24
2-7	Standard albedo curve corresponding to visible radiance values at zero solar zenith angle. . . . .	25
2-8	NESS standard calibration curve for temperature versus infrared radiance value. . . . .	27
2-9	Altitude and time variation of temperature on 22 June 1976 at Big Spring, Texas. . . . .	29
2-10	Same as Figure 2-9 for Midland, Texas . . . . .	30
2-11	Same as Figure 2-9 for Post, Texas. . . . .	31
2-12	Same as Figure 2-9 for Robert Lee, Texas. . . . .	32
2-13	The "average" sounding for the study area on 22 June 1976 . . . . .	33
2-14	Pictorial representation of data points used in stretching infrared radiance data. ■ represents an original data point and • represents an interpolated sub-point. . . . .	37
3-1	Variation of the number of clouds in three different size categories derived from radiance measurements. . . . .	43
3-2	The percentage of cloud cover for total cloud area, widespread clouds and isolated clouds . . . . .	49

<u>Figure</u>		<u>Page</u>
3-3	Curves of the frequency distribution of visible radiance values. All curves are plotted relative to the critical visible radiance value, cloud points to the right and non-cloud points to the left of this value . . . . .	53
3-4	Difference between the mean brightness value ( $\overline{VIS}$ ) and the critical brightness value ( $VIS_{crit}$ ) for several categories of clouds. .	56
3-5	The ratio of the difference between mean brightness of small isolated clouds and mean brightness of non-cloud. . . . .	58
3-6	The comparison of cloud mean brightness and cloud size at 1745 and 2245 GMT on 22 June 1976 . . . . .	61
3-7	The comparison of standard deviation of cloud brightness and cloud size at 1745 and 2245 GMT on 22 June 1976. . . . .	63
3-8	The comparison of standard deviation of cloud brightness and cloud mean brightness above its corresponding critical value at 1745 and 2245 GMT on 22 June 1976 . . . . .	65
3-9	The comparison between the ratio of standard deviation of brightness (S.D. of $\overline{VIS}$ ) to the difference of mean brightness ( $\overline{VIS}$ ) and critical visible value ( $VIS_{crit}$ ) and difference of $\overline{VIS}$ and $VIS_{crit}$ at 1745 and 2245 GMT on 22 June 1976 . . . . .	67
3-10	Albedo curves for solar zenith angles ( $\theta_0$ ) equal to $0^\circ$ , $71.5^\circ$ , and $83.5^\circ$ . . . . .	71
3-11	The maximum and minimum albedo of a single pixel as well as the maximum mean albedo of a cloud . . . . .	72
3-12	Computer-generated plots of visible and infrared radiance patterns from 1745 GMT 22 June to 0115 GMT 23 June 1976. An explanation of the symbols used is given following the plots for 0115 GMT on 23 June 1976. . . .	75
3-13	Percentages of cirrus and deep vertical development clouds observed within the study area. . . . .	88

CHAPTER I  
INTRODUCTION

With the rapid development of scientific technology in atmospheric science, the satellite has become a very valuable tool to study the atmosphere. The launches of the TIROS (1960-1965), ESSA (1966-1969), Nimbus (1964-1975) and NOAA (1970-1976) series of satellites have provided radiant energy data from the visible to the CO<sub>2</sub> region of the infrared. These measurements have been developed to determine vertical temperature and water vapor profiles, liquid water content, surface temperature, cloud height and movement, and total outgoing longwave radiation flux. This study utilizes visible and infrared radiance data obtained from a Geostationary Operational Environmental Satellite (GOES) for cloud studies. An analysis technique is presented to determine cloud amount, distribution, temperature, height and movement through the utilization of sets of simultaneous satellite visible and infrared radiance data and the contemporaneous rawinsonde data.

To identify the cloud cover region, a critical brightness value to distinguish cloud from underlying non-cloud background is found as a primary factor in this study. Because the solar radiation is attenuated by scattering and absorption in proportion to the path length traveled through the atmosphere, Beer's law is applied to obtain these critical values as they vary with solar zenith angle.

Using the critical brightness value as an input variable, a cloud summary computer program is utilized to obtain the following statistical results for this study:

- (1) Percentage of cloud cover and mean brightness of cloud and non-cloud areas for the entire region;
- (2) Size, maximum brightness, mean and standard deviation of brightness and location of brightness, and geometric centers of every individual cloud;
- (3) Tables of the frequency distribution of brightness of individual data points, the frequency distribution of mean brightness of clouds and the frequency distribution of cloud size.

All of these data sources are used to analyze the cloud properties and patterns and their variations with time.

Albedo values are determined for different categories of clouds. Cloud height is determined through the top temperature of a cloud. The cirrus clouds are identified as a region with low albedo value and low cloud top temperature. The movements of clouds are investigated. Comparing the cloud characteristics with the assistance of computer-generated cloud pictures, cloud movement can be obtained by following the overall motion of the cloud pattern as well as that of individual brightness centers. These estimates are compared with the vertical wind profile from sounding data. Fifteen consecutive sets of simultaneous satellite visible and infrared radiance data on 22

June 1976 have been selected for this study in the West Texas High Plains area. The objective of this study is to develop techniques for the determination of cloud properties using bispectral radiance measurements obtained by meteorological satellites. The research has been undertaken in support of weather modification efforts in this region.

### 1.1 Historical Background

On 1 April 1960, the first weather satellite, TIROS 1, was launched successfully for atmospheric research purposes. TIROS 1 was the first satellite of a series of ten (1960-1965) which carried television cameras to provide cloud cover photographs of the earth. Besides television cameras, the other nine TIROS satellites also carried infrared sensors and were able to estimate temperature on a worldwide basis. Nimbus 1 was launched on 28 August 1964. It was equipped with an Advanced Vidicon Camera Subsystem (AVCS), Automatic Picture Transmission (APT) and a High Resolution Infrared Radiometer (HRIR), and was the first satellite able to provide both daytime and nighttime pictures. Nimbus 3, launched in 1969, provided the first vertical temperature profile data of the atmosphere on a global basis. Nimbus 6 launched on 12 June 1975, carried the High Resolution Infrared Radiation Sounder (HIRS) which is a third-generation instrument with new features, one of which is measurement in the  $4.3 \mu\text{m}$   $\text{CO}_2$  band, allowing temperature soundings up to the 40 km level and improving the

water vapor profiles below the 10 km level (NESS, 1976). Nimbus 4-6 are presently in operation and are providing data for research analysis.

ESSA 1, launched in 1966, was the first satellite designated as an operational system. The satellite carried two wide-angle TV cameras and was able to provide full global cloud coverage in daytime. On 6 December 1966, the Applications Technology Satellite (ATS-1) was launched, carrying a spin-scan cloud camera to provide cloud cover data. This was the first satellite in geosynchronous orbit. On 17 May 1974, the National Aeronautics and Space Administration (NASA) launched the Synchronous Meteorological Satellite (SMS-1), the first prototype for the GOES system. SMS-1 carried a Visible and Infrared Spin-Scan Radiometer (VISSR), a Space Environment Monitor (SEM), a Data Collection System (DCS) and a weather facsimile broadcast system (Dismachek, 1977). The satellite was placed in a geostationary orbit that is 35,788 km over the equator at 75°W longitude. SMS-2, the second prototype of the GOES system, was launched on 6 February 1975 at 115°W longitude. On 16 October 1975, NOAA launched GOES-1, the first operational geostationary satellite, into a geostationary orbit, 35,783 km above the equator at 55°W longitude. GOES-1 carried the same equipment and communication systems as SMS-1 and SMS-2. On 19 December 1975, SMS-2 was moved to its present location at 135°W as the western operational satellite, and will be

referred to as GOES WEST in this study. On 8 June 1976, GOES-1 was moved to  $75^{\circ}\text{W}$  to replace SMS-1 as an eastern operational satellite, and will be designated as GOES EAST for this study. GOES-2, launched on 16 June 1977, has since replaced GOES-1 as the eastern operational satellite at  $75^{\circ}\text{W}$  (NESS, 1978).

In this study data collected from the GOES have been acquired in two formats: (1) radiance measurements from GOES WEST, and (2) photographic imagery from GOES EAST. The imagery is available at 30 min intervals as alternating visible and infrared photographs from 1200 to 0000 GMT. From 0000 to 1200 GMT, the infrared images are provided every half hour. The radiance data are obtained as simultaneous sets of both visible and infrared digital data with a 30 min interval. Both images and radiance data were used to determine the parameters of cloud in this study. Visible and infrared images from both GOES EAST and GOES WEST are used to determine wind vectors from cloud movement. In addition, infrared radiance data are used to determine cloud top temperature from which cloud heights are derived.

## 1.2 Literature Survey

Since the first weather satellite was launched in 1960, cloud cover photographs of the earth have been available. Recently, improved visible and infrared radiance data have become available from satellites for atmospheric studies. Booth and Taylor (1969) have analyzed digitized cloud

imagery received from the ESSA satellite, using data which were produced and stored for subsequent computer investigations. The digitized value at each measurement spot was related to the brightness of a cloud or non-cloud area, or a mixture of the two. An analysis using both cloud images and infrared radiance data was presented by Vonder Haar (1970). This study was based on a global scale and relatively long time intervals. The cloud images and infrared radiance data were used to estimate the height and type of clouds according to qualitative combinations of these two sources of information.

A cloud height determination system has been developed at the University of Wisconsin-Madison and described by Mosher (1974). In order to improve infrared estimates of cloud top height, the emissive properties of the clouds obtained from independent sources were required. The optical thickness can be obtained through the visible brightness. Because both visible reflectance and infrared emissivity are dependent upon the total number of cloud particles in a vertical column through the cloud, knowing the optical thickness permits the emissivity of the cloud to be determined. Using the cloud emissivity and infrared radiance data, the temperature of the cloud top can be obtained. Then, the cloud height can be obtained by comparing the derived cloud top temperature with the vertical temperature profile provided by sounding data.

Park et al. (1974) examined the relationship between cloud thickness and brightness. Nimbus 4 infrared digital data were compared with radiosonde data and radar images to obtain cloud top temperature and cloud thickness. The brightness values were obtained from ATS-3 visible radiance data. A frequency scatter diagram was used to examine the correlation between brightness and cloud thickness in day-time data. The case study showed good correlation between the two, especially for well-developed cumulonimbus clouds.

A bispectral analysis method was introduced by Reynolds and Vonder Haar (1977) for determining cloud heights and amounts through the use of sets of simultaneous visible and infrared NOAA satellite radiance data. Two simultaneous spectral radiance equations are obtained to derive cloud top temperature and cloud amount within the geometric field of view of the sensor. Cloud height then can be obtained by comparing cloud top temperature to upper-air sounding data. Comparisons of satellite-derived cloud top heights and observed radar echo heights have not produced consistent results. Some investigators have reported satellite-derived cloud top heights to be greater (Waters, et al., 1977), while others (Adler and Fenn, 1977) have obtained the opposite result. On the basis of the available information, it appears that agreement is possible within 2 km in most cases. Considerable additional work is needed on this subject, however.

## CHAPTER II

### DATA PROCESSING PROCEDURES

#### 2.1 Data Transmission and Acquisition

The satellite system selected in this study is the Geostationary Operational Environmental Satellite (GOES). The satellites are in geosynchronous orbits with sub-satellite points of  $75^{\circ}\text{W}$  (GOES EAST) and  $135^{\circ}\text{W}$  (GOES WEST) over the equator, viewing the Western Hemisphere as shown in Figure 2-1. From this position the satellite can view all of North and South America and adjacent ocean areas with good resolution, as well as obtain and transmit data messages from any point on the earth within its view.

The Visible and Infrared Spin-Scan Radiometer (VISSR) sensors of GOES scan the surface of the earth, detecting radiant energy with eight visible spectrum channels in the range of 0.55 to 0.75  $\mu\text{m}$ , and with two infrared channels in the range of 10.5 to 12.6  $\mu\text{m}$  (Bristor, 1975).

The GOES data are received and transmitted by the Data Acquisition and Processing System (DAPS) of the National Environmental Satellite Service (NESS). All sensor data for central processing are acquired in a compressed format by the two NESS Command and Data Acquisition (CDA) stations which are at Wallops Island, Virginia and Gilmore Greet, Alaska. The data signals of GOES EAST arrive at Kansas City, Missouri and are recorded on a photofacsimile recorder. The National Weather Service (NWS) Forecast Office at Lubbock

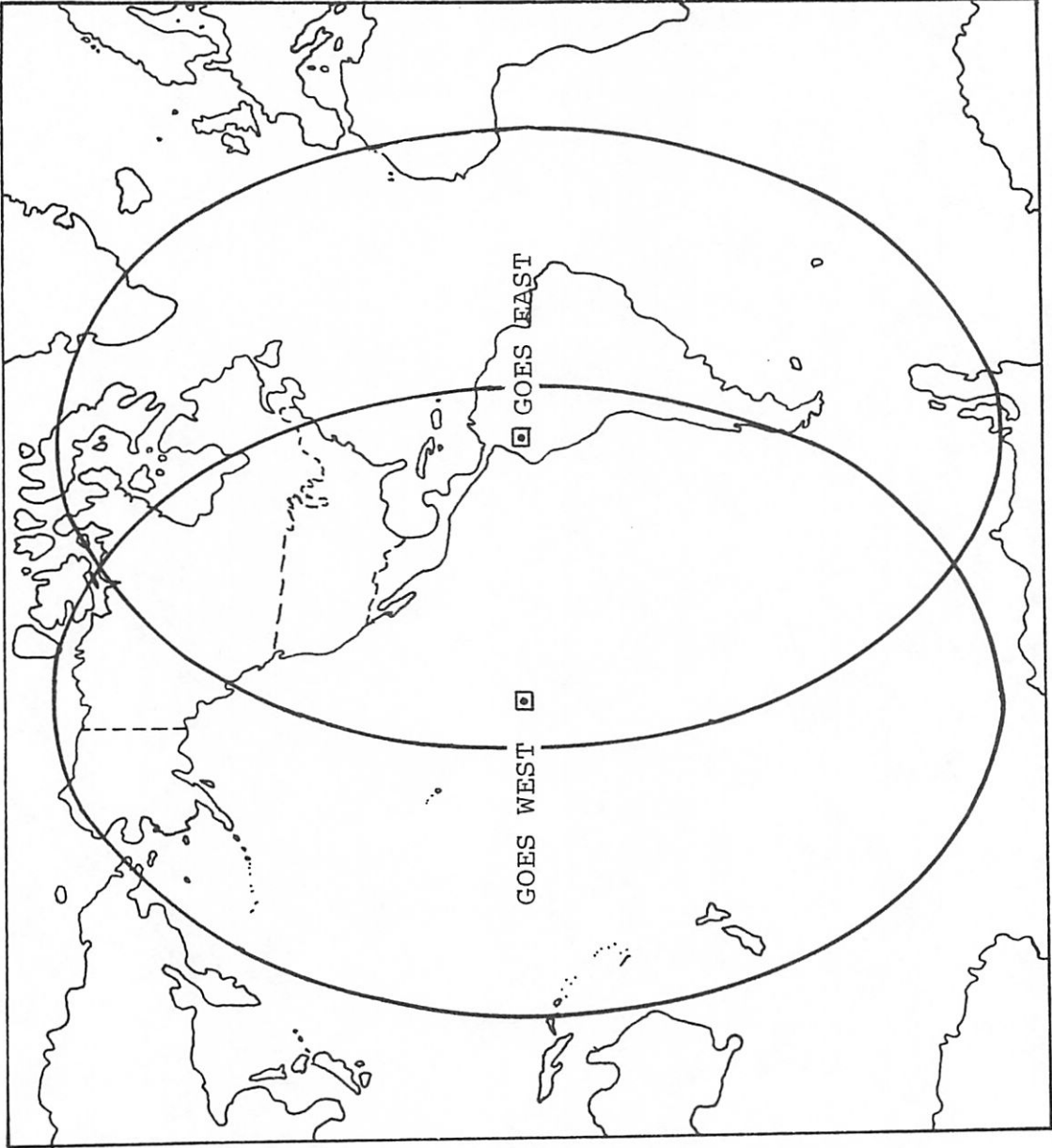


Figure 2-1 Location and approximate operational coverage of the two satellite data sources: GOES WEST at 135° W and GOES EAST at 75° W longitude.

receives the imagery signal and produces the visible and infrared images which are used in this study. Visible images were created during daytime at one hour intervals on the hour and infrared images were also created at one hour intervals throughout the day every 30 min after the hour. The raw data stream from GOES WEST was received at White Sands Missile Range, New Mexico and recorded on magnetic tape from which visible (VIS) and infrared (IR) data were derived by Colorado State University (CSU) for this study. Both visible and infrared radiance data were available at 15 to 45 min after the hour from GOES WEST.

The target area of this study is a 315 by 315 km area, with the corresponding array sizes being 216 by 216 points for VIS data and 27 by 54 points for IR data, each centered at Big Spring, Texas. The spatial size of a single VIS data element, or pixel, in this area is 1.46 by 1.46 km. An IR data element covers an area equivalent to a 4 by 8 array of VIS elements, or a 5.84 by 11.68 km area. Because the GOES WEST satellite is located west of the target region in this study, the data are not aligned in a north-south direction but are displaced by  $11.3^{\circ}$  in the clockwise direction from north, as shown in Figure 2-2.

All available satellite images and selected radiance data have been collected for the period from 1 June to 15 July 1976, the period of operation of the Texas High Plains Experiment (HIPLEX). June 22 was chosen for this study

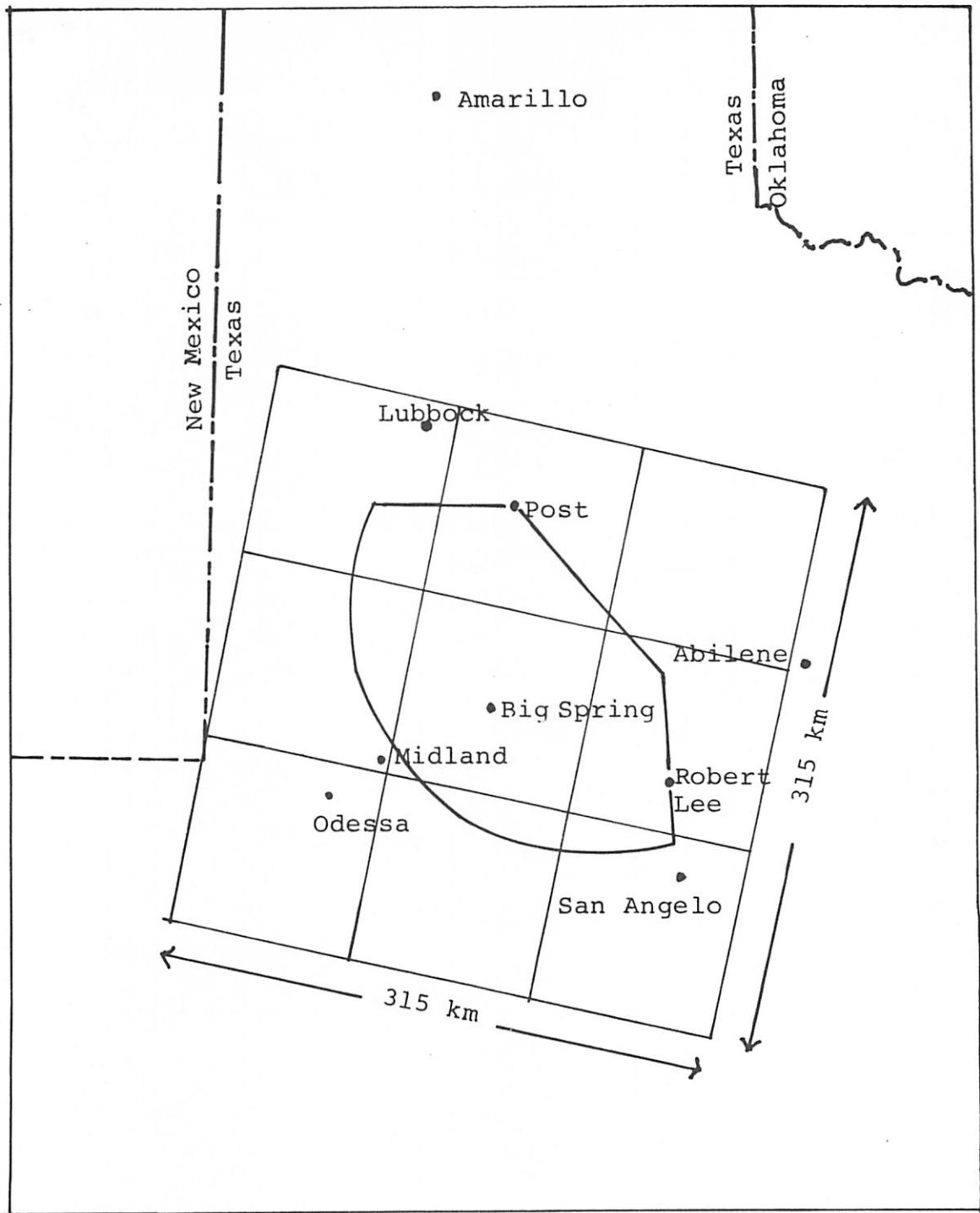


Figure 2-2 The area of study. The sector at the center is the Texas HIPLEX study region.

because of the availability of VIS and IR radiance data, photographic images and rawinsonde data. Fifteen sets of VIS and IR data are used to compute cloud properties.

Both VIS and IR data on 22 June were preprocessed and reformatted from raw data tapes. The possible VIS radiance data value range is from 0 to 255 in intervals of 4 units, and the IR radiance data can vary from 0 to 255 by intervals of 1 unit. Through the use of the CSU ADVISAR (All Digital Video Imaging System for Atmospheric Research) (Smith, 1977a), it was found that extremely bright or dark single data points or lines, produced by data transmission problems, existed in some of the VIS radiance data sets. These were identified as bad data but represented less than 0.5% of the data in the majority of the data sets. At 2245 GMT of June 22 and 0045 GMT of June 23, the existence of several bad data lines increased the percentage of bad data to 1% of the data set. Bad data produced by data transmission errors usually had a value near to 0 or 255, far from the normal data range. Through a detailed analysis of several complete data sets, it was determined that such data points differed by at least 50 from neighboring points. In order to correct these bad data values, every pixel was compared with its surrounding data values. If the data value in question deviated by more than 50 units from the surrounding points, it was replaced by their average. A bad data line was corrected using an interpolated value which was obtained from the pixels

in the lines above and below the bad line. In this manner, good VIS data sets were produced for subsequent analysis.

The surface synoptic chart at 1200 GMT on 22 June 1976 (Figure 2-3) showed a front located west of the Rocky Mountains with a low pressure region in Wyoming moving southeastward. Ahead of this front, there was a weak high pressure center located in northwestern New Mexico. A small low was located near El Paso. Surface winds in most of Texas were southeasterly from the Gulf of Mexico, bringing abundant low-level moisture into the region. Dew point temperature increased gradually from New Mexico toward southeastern Texas. At Waco and Corpus Christi, Texas, dew points reached to 72F (22.2C) near saturation. Precipitation occurred northwest of Junction and shower activity was reported at Fort Worth and in Waco area. Sky cover reports from meteorological observation stations in Texas ranged from scattered to overcast. At Amarillo and Abilene, cirrus and altocumulus were observed. Altocumulus was reported at Midland and low level clouds were at Fort Worth and San Antonio.

The 500 mb pattern at 1200 GMT on 22 June 1976 (Figure 2-4) showed that there was cold air advection west of the mountainous area in Arizona. A warm region (-5C) of high pressure was located over northern Mexico. This region caused the warm area and ridge to extend from Colorado through New Mexico. Upper level winds in Texas were northwesterly at approximately 20 kt.

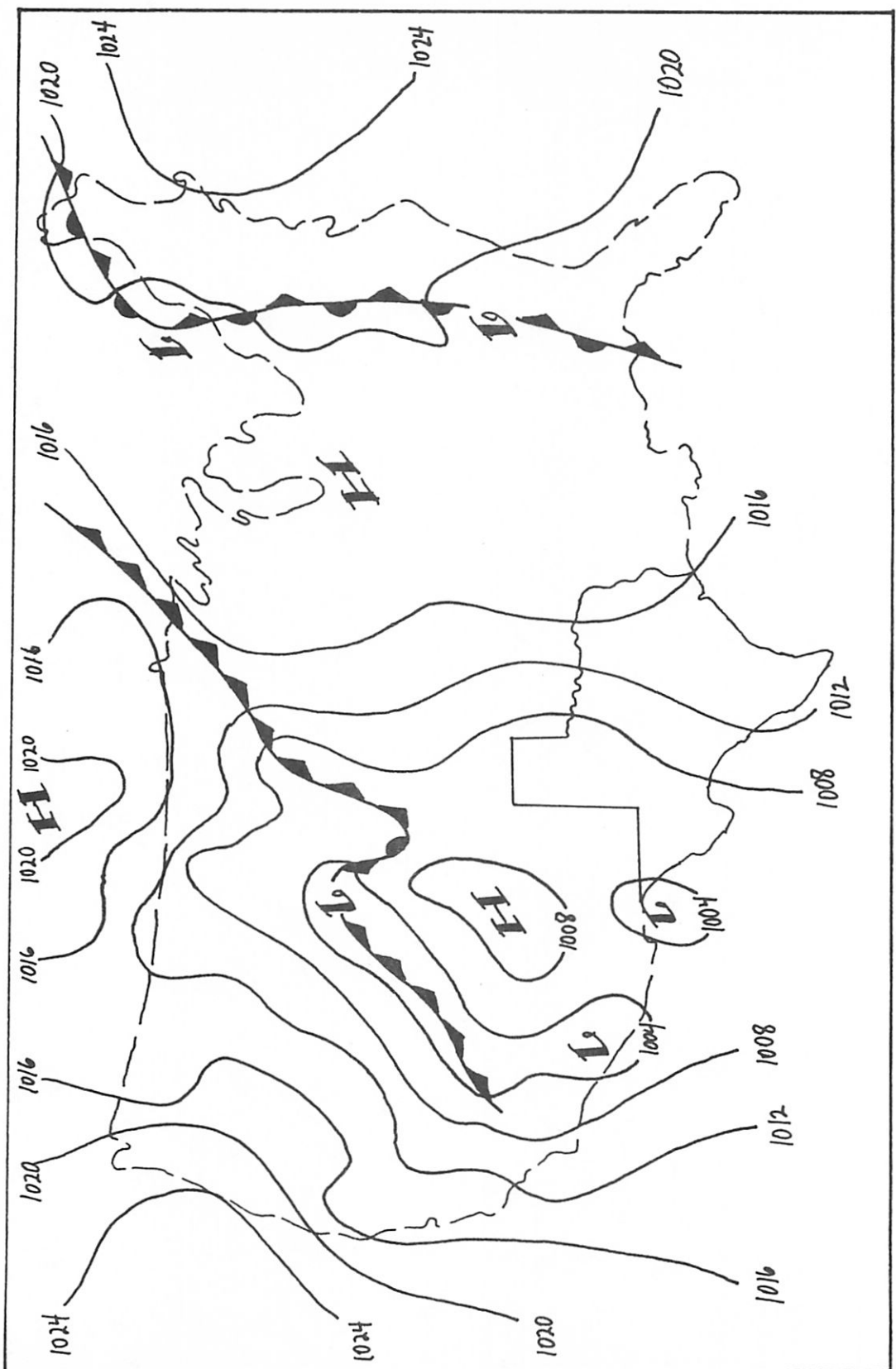


Figure 2-3 Surface synoptic chart at 1200 GMT on 22 June 1976.

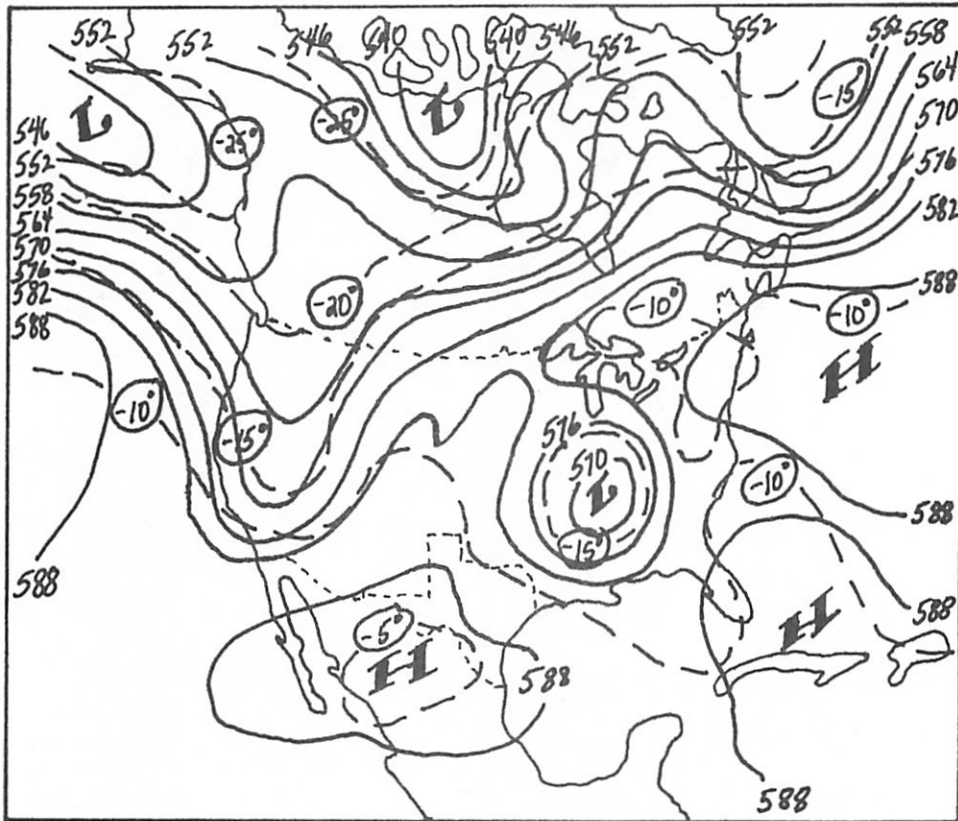
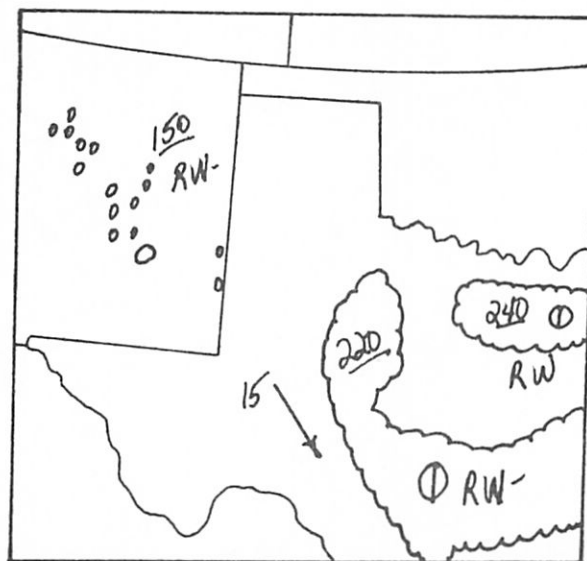


Figure 2-4 500 mb weather map at 1200 GMT on 22 June 1976. Contours (solid lines) are given in decameters and isotherms (dashed lines) are given in Celsius degrees.

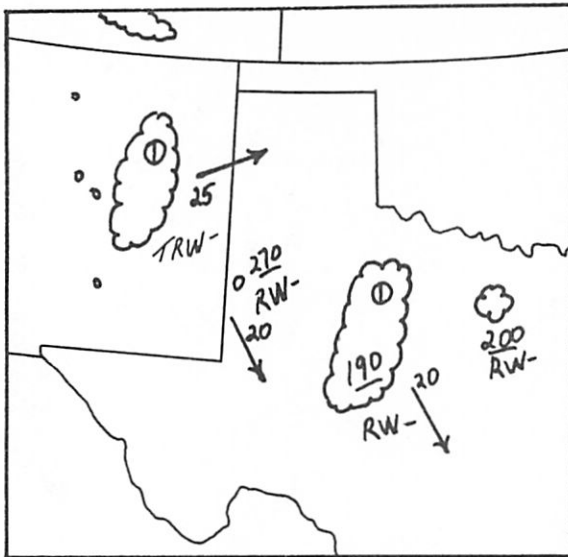


1735 GMT

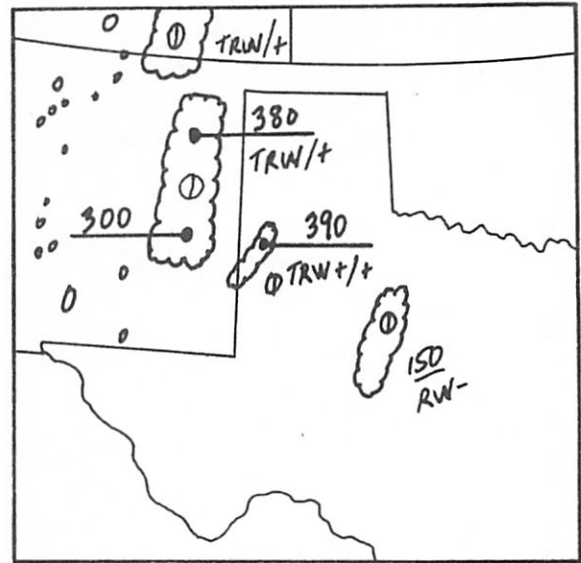
Figure 2-5 Radar summary charts from 1735 GMT 22 June to 0135 GMT 23 June 1976.

The NWS radar summary charts throughout this study period are shown in Figure 2-5. On the radar summary chart at 1735 GMT, precipitation was occurring in the Fort Worth, Abilene, and San Antonio areas. The vertical extent of echoes was not high, reaching only 24,000 ft at Fort Worth and 22,000 ft at Abilene. Meanwhile, some small isolated convective radar echoes associated with light rain showers were reported in the Rocky Mountain area of center New Mexico and two small echoes with light rain showers were located along the Texas-New Mexico border. At 1835 GMT an area of echoes with heavy thunderstorms were found east of the mountain area. The radar echo around Abilene dissipated gradually; the top decreased to 19,000 ft at 1835 GMT and 15,000 ft at 1935 GMT and at 2035 GMT no echo was detected. In the meantime, the band of echoes in New Mexico built up to 45,000 ft by 2035 GMT and moved into Texas with a speed of 20 kt. This echo continued to organize, becoming a squall line with severe thunderstorms and very heavy rain by 0035 GMT on June 23. At 0135 GMT the radar echo was dissipating and heights were significantly reduced.

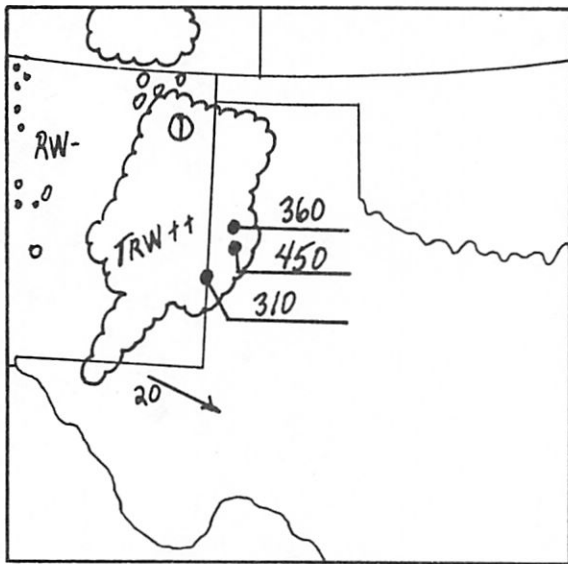
From the above synoptic weather maps and radar summary charts, it was found that thunderstorms developed in the Rocky Mountain area during the afternoon of 22 June 1976. Strong radar echoes built and subsequently moved into the study area. This situation was selected as a case study to determine the cloud properties based on the bispectral



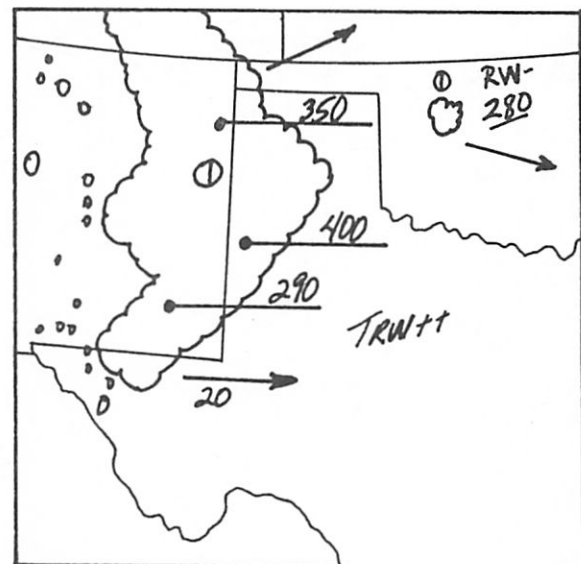
1835 GMT



1935 GMT

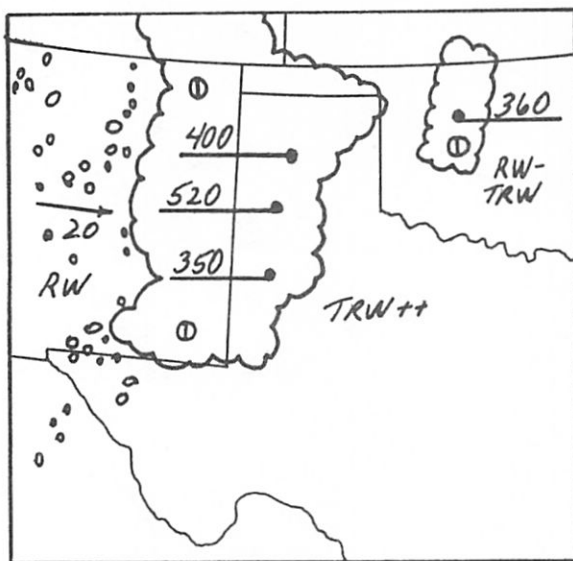


2035 GMT

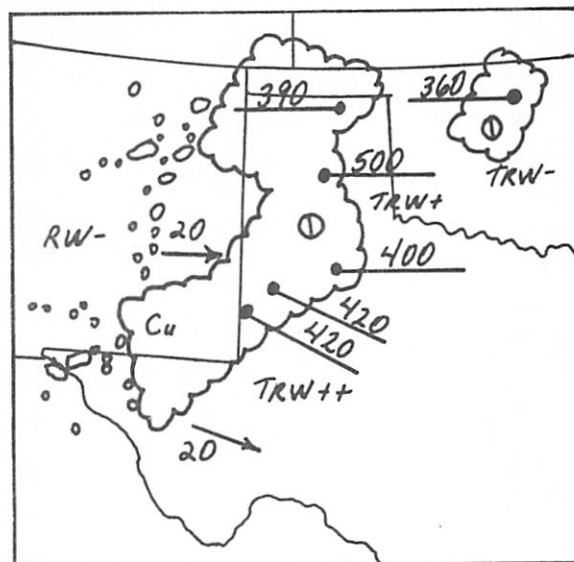


2135 GMT

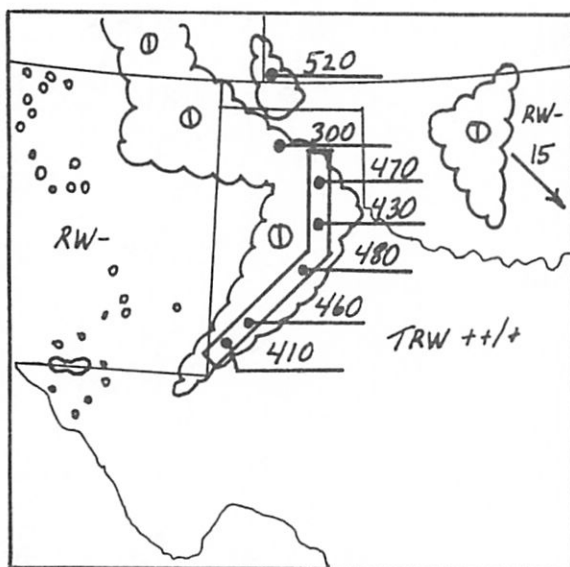
Figure 2-5 Continued.



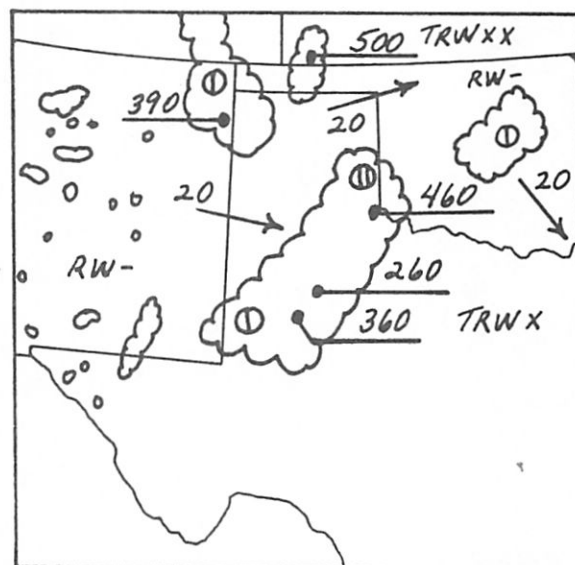
2235 GMT



2335 GMT



0035 GMT



0135 GMT

Figure 2-5 Continued.

satellite radiance data.

## 2.2 Visible Radiance Measurements

A primary factor in the analysis of radiance values for the cloud study is the determination of a critical VIS radiance value to distinguish clouds from the underlying non-cloud surfaces. There are several variables including physical cloud properties (terms a to d below) and non-cloud properties (term e below) which influence the radiance reflected from a cloud (Mosher, 1974):

- a. The droplet size distribution and shape of the cloud particles;
- b. The number density of scattering particles in the cloud;
- c. The cloud thickness;
- d. The shape of the cloud;
- e. The zenith angles of the sun and the satellite and their relative azimuth angle.

Since the objective of this study is to investigate cloud parameters through radiance data analysis, only the non-cloud factors will be used in the computation of the critical values; the approach described below follows Jurica (1978).

At each time of day, a different brightness value corresponds to a given cloud albedo. The main factor is the solar zenith angle; the larger the solar zenith angle the smaller will be the VIS value obtained for a certain

albedo. Because a larger solar zenith angle corresponds to a longer path length through the atmosphere and therefore greater attenuation, Beer's law may be applied to find the atmospheric attenuation variation caused by the change of solar zenith angle with time.

Viewing a measurement spot from the VISSR sensor on the satellite, the measured radiance  $R$  is given by Beer's law as:

$$R = \alpha R_0 e^{-\tau \sec \theta} e^{-\tau \sec \theta_0} \text{ --- ( 1 )}$$

where  $\alpha$  : the albedo of the measurement spot

$\tau$  : effective optical thickness of the atmosphere

$R_0$  : unattenuated irradiance

$\theta_0$  : solar zenith angle

$\theta$  : satellite zenith angle

The satellite zenith angle  $\theta$  is essentially constant for the GOES WEST sensors viewing the area of interest in this study. The effective optical thickness of the atmosphere will be essentially constant for a given day. Therefore, the variation of radiance ( $R$ ) will be influenced by diurnal variations of the solar zenith angle and the albedo of the measurement spot. The ratio of radiances at two different solar zenith angles,  $\theta_{01}$  and  $\theta_{02}$ , is

$$\frac{R_{\theta_{02}}}{R_{\theta_{01}}} = \frac{\alpha_2 R_0 e^{-\tau \sec \theta} e^{-\alpha \sec \theta_{02}}}{\alpha_1 R_0 e^{-\tau \sec \theta} e^{-\alpha \sec \theta_{01}}}$$

$$= \frac{\alpha_2 e^{-\tau \sec \theta_{02}}}{\alpha_1 e^{-\tau \sec \theta_{01}}} \text{ - - - - - ( 2 )}$$

In order to determine the variation with time of the critical value of VIS brightness, locations with similar cloud amounts and properties are used as test points. Therefore, the value of albedo at the measurement spot can be assumed constant with time. Neglecting albedo variations at the measurement spot, equation (2) can be written as

$$R_{\theta_{02}} = R_{\theta_{01}} e^{-\tau(\sec \theta_{02} - \sec \theta_{01})} \text{ - - - - - ( 3 )}$$

or

$$\ln R_{\theta_{02}} = \ln R_{\theta_{01}} - \tau(\sec \theta_{02} - \sec \theta_{01}) \text{ - - - - - ( 4 )}$$

Because the VISSR digital value is proportional to radiance, equation (4) can be written

$$\ln \text{VIS}_2 = \ln \text{VIS}_1 - \tau(\sec \theta_{02} - \sec \theta_{01}) \text{ - - - - - ( 5 )}$$

where  $\text{VIS}_1$  : visible digital value at solar zenith angle  $\theta_{01}$ ,

$\text{VIS}_2$  : visible digital value at solar zenith angle  $\theta_{02}$ .

The ADVISAR display was used to determine two visible digital values,  $\text{VIS}_1$  and  $\text{VIS}_2$ , at two different times on 22 June 1976. A pair of VIS values were selected to determine the value of  $\tau$ , the effective optical thickness of the atmosphere. In applying Beer's law the assumption is made that the atmosphere is isotropic, that is, it consists of a series of homogeneous plane parallel layers. This

assumption introduces an error which becomes important only for solar zenith angles greater than  $70^{\circ}$  (Fleagle and Businger, 1963). Therefore, the times selected to obtain  $\tau$  were 1845 GMT, corresponding to a solar zenith angle of  $8.5^{\circ}$  (which is the minimum) and 2345 GMT, corresponding to a solar zenith angle of  $65.5^{\circ}$  (which is the largest not exceeding  $70^{\circ}$ ). The critical VIS radiance values are 120 and 92, respectively. The corresponding value of effective optical thickness was computed to be 0.19. Substituting the values  $VIS_1$ ,  $\tau$ , and different solar zenith angles into equation (5), critical cloud/non-cloud values on 22 June were obtained as shown in Table 2-1. Because the VIS digital values range from 0 to 255 in increments of 4, some adjustments were made. Late in the day (0115 GMT 23 June) a large deviation occurred between the theoretical and adjusted values for the low sun condition (Figure 2-6). Using the ADVISAR system, the adjusted critical values were examined to check their accuracy and will be used for subsequent analysis.

As discussed earlier, the intensity of the reflected solar radiance depends on the albedo of earth and atmosphere and on the zenith angle of the incoming solar radiation. Knowing the solar zenith angle and the reflected short-wave radiance, the value of albedo of a measurement spot corresponding to a given VIS digital value was obtained based on a critical value of 120 at 1845 GMT (Figure 2-7). Because

Table 2-1 Solar zenith angle and visible radiance values used to distinguish clouds from the non-cloud background.

Time (GMT)	Solar zenith angle ( $\theta_0$ )	$\sec\theta_{02} -$ $\sec\theta_{01}$	Theoretical critical value	Adjusted critical value
22 June 1745	16.0	0.029	119.3	120
1815	11.0	0.008	119.8	120
1845	8.5	0.000	120.0	120
1915	11.0	0.008	119.8	120
1945	16.0	0.029	119.3	120
2015	21.5	0.064	118.6	120
2045	27.5	0.116	117.4	120
2115	33.5	0.188	115.8	120
2145	40.0	0.294	113.5	116
2215	46.5	0.442	110.3	112
2245	53.0	0.650	106.0	108
2315	59.5	0.959	100.0	100
2345	65.5	1.400	92.0	92
23 June 0015	71.5	2.140	79.9	80
0045	77.5	3.609	60.4	64
0115	83.5	7.823	27.1	48

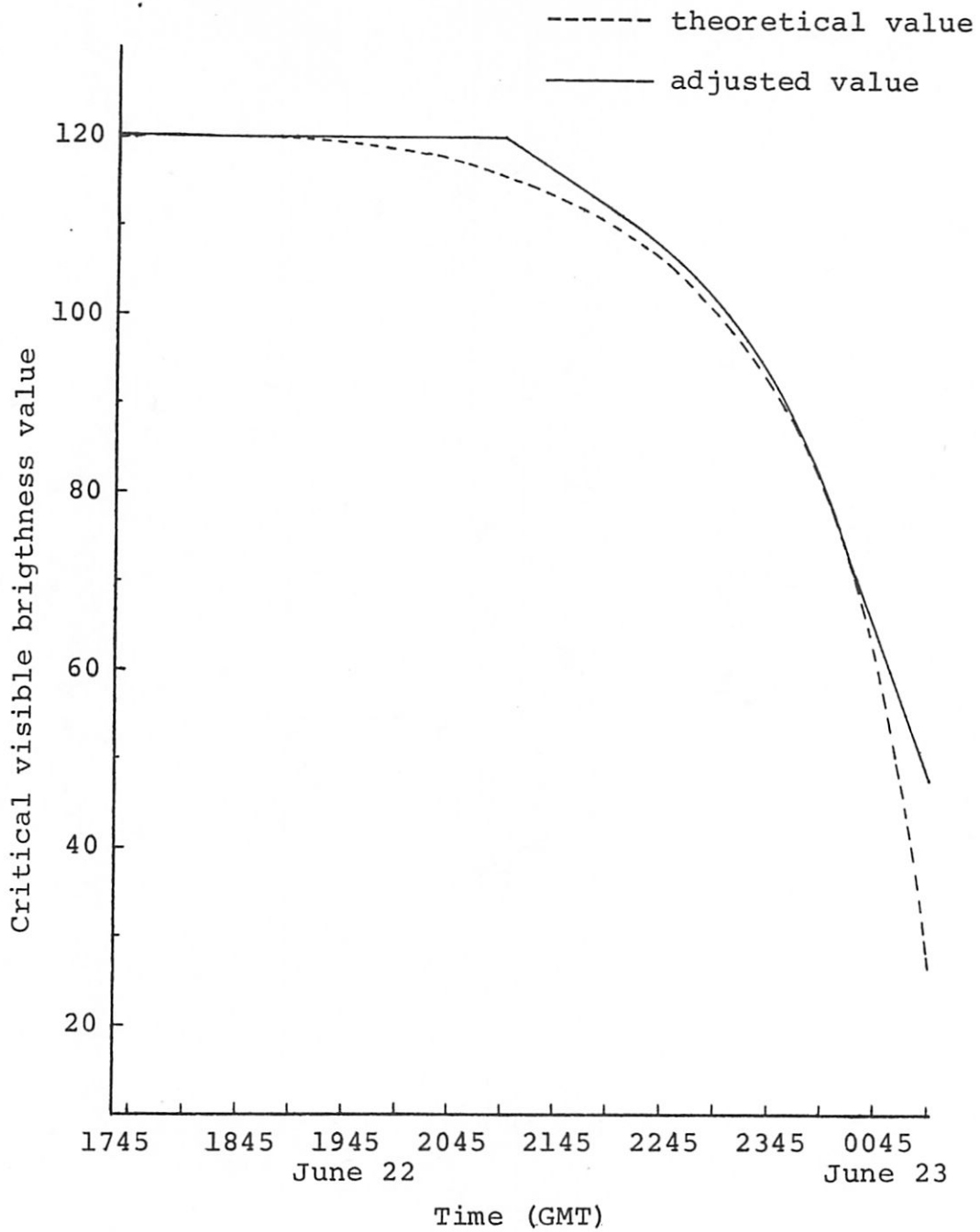


Figure 2-6 Comparison of the theoretical and adjusted critical visible values.

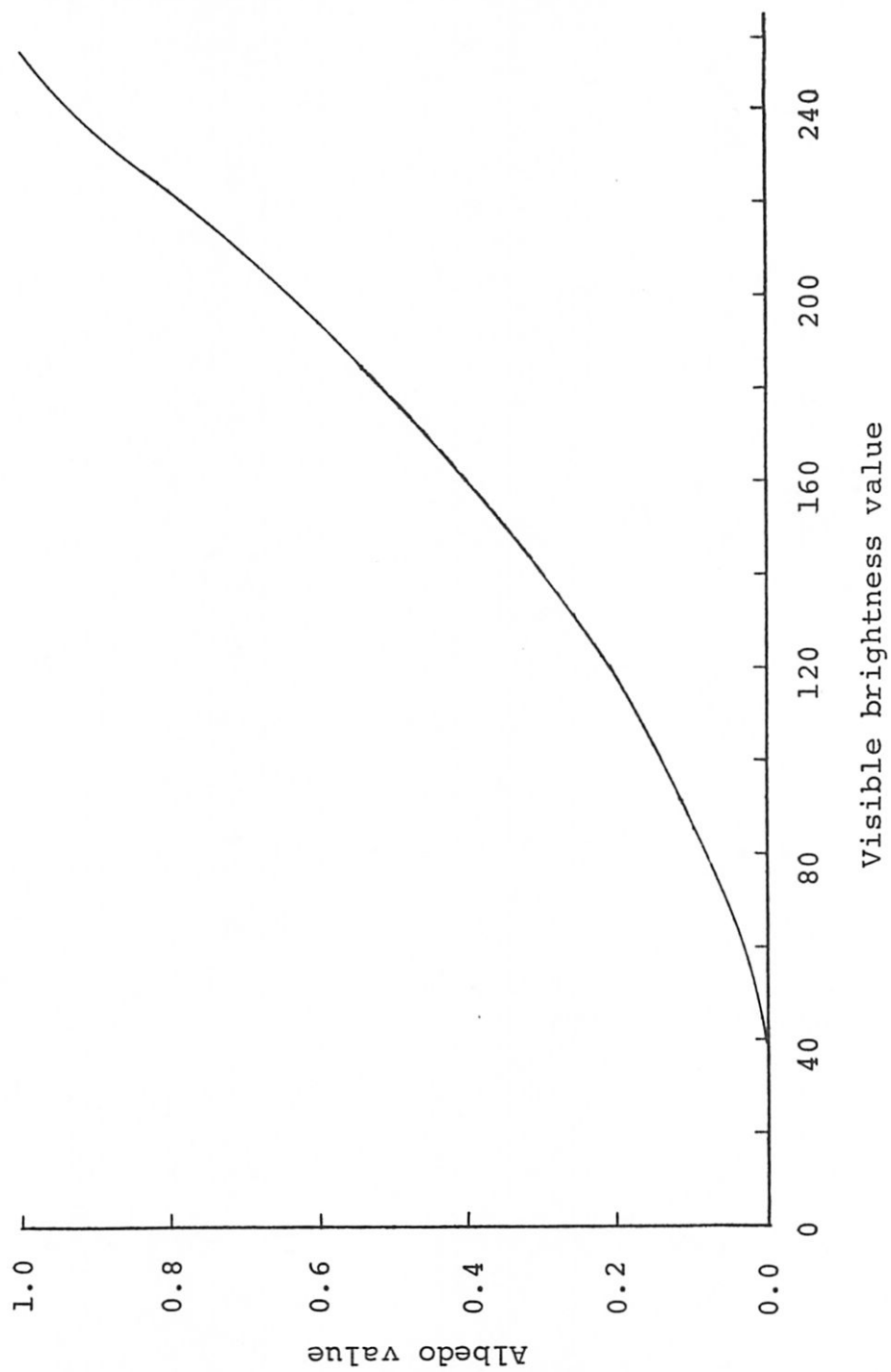


Figure 2-7 Standard albedo curve corresponding to visible radiance values at zero solar zenith angle.

solar zenith angle variations change the critical value for cloud detection, the brightness value versus albedo scale will change with time in direct proportion to the critical value.

### 2.3 Infrared Radiance Measurements

The VISSR sensor of GOES WEST also detects the flux of radiation emitted by the observed surface in the infrared portion of the spectrum. The radiance is converted to an IR digital value with a range from 0 to 255. The infrared measurements provide estimates of the earth surface temperature under clear skies and cloud top temperatures under overcast situations. The NESS standard calibration curve (Figure 2-8) has been used to convert the IR values to temperatures. From Figure 2-8 it can be seen that as the IR value increases in unit steps from 0 to 175 the temperature decreases by 0.5 Kelvin degrees from 330.0 to 242.5K. For IR values greater than 175, the temperature decreases by one Kelvin degree per unit step to the lowest value of 163K corresponding to an IR value of 255. Knowing the true temperature of the cloud top, the cloud top height can be determined if the vertical temperature profile is known. This aspect is described in Section 3.3.

In order to convert the cloud top temperature to cloud height, a vertical temperature profile is necessary. On each Texas HIPLEX operational day soundings were obtained by Texas A&M University (Scoggins et al., 1978) at three

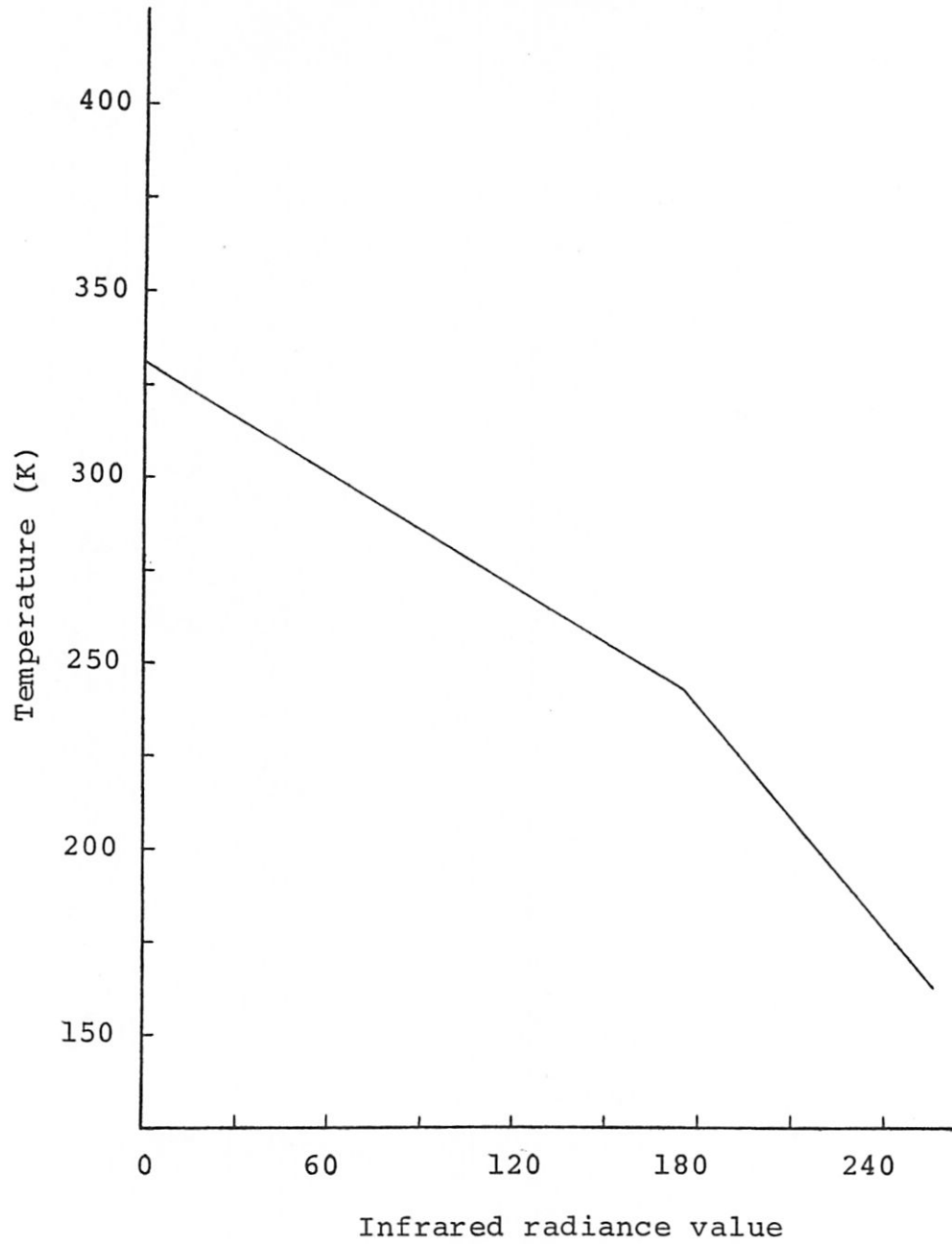


Figure 2-8 NESS standard calibration curve for temperature versus infrared radiance value.

hour intervals at Big Spring, Midland, Post and Robert Lee, Texas. For the case analyzed, soundings are available at 1500, 1800 and 2100 GMT on 22 June and 0000 and 0300 GMT on 23 June. Temperature versus time cross-sections have been constructed for these four stations (Figure 2-9 to 2-12). From these vertical temperature profiles, it may be seen that the isotherms are nearly horizontal, indicating that the quantity of long-wave radiation does not change with time. Since the altitude of each isotherm is very similar from station to station, a single averaged sounding curve (Figure 2-13) can be used throughout the day for cloud height determination. The time-averaged isotherm heights at the individual stations are displayed in Table 2-2. The last two columns of the table display the standard deviation of average height for the given temperatures. Neglecting the inherent inaccuracies of both the rawinsonde and satellite data, the cloud top height can be estimated to within 500 m. The application of cloud top height determination is discussed in detail in Chapter 3.

#### 2.4 Alignment of visible and Infrared Data

The VIS and IR digital data arrays for the target region are 216x216 and 27x54 arrays, respectively. The VIS and IR sensors of GOES simultaneously scan the earth in a west to east direction, then step down and scan again. However, there is a misalignment of the VISSR sensors that causes an east-west offset between VIS and IR data.

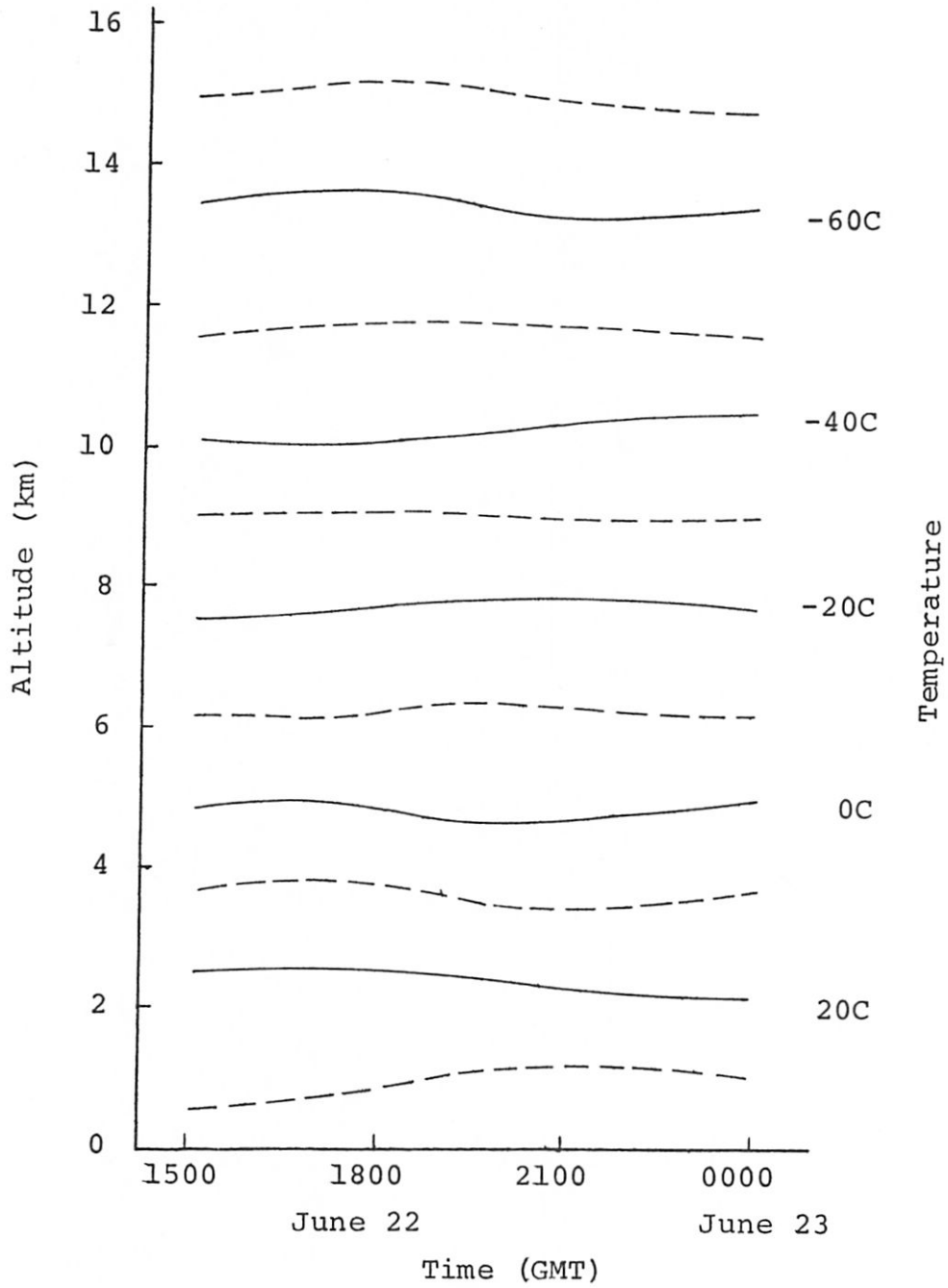


Figure 2-9 Altitude and time variation of temperature on 22 June 1976 at Big Spring, Texas.

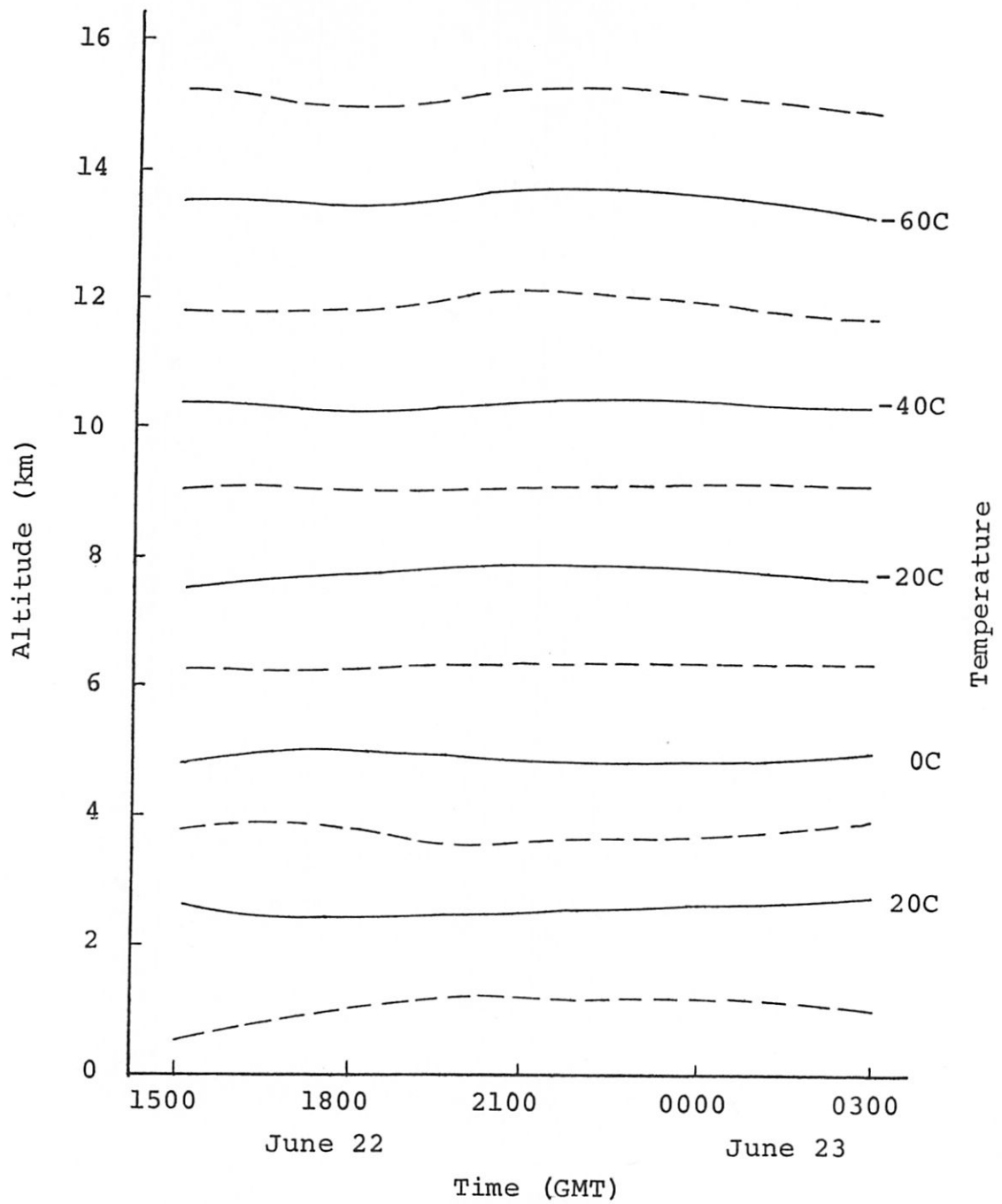


Figure 2-10 Same as Figure 2-9 for Midland, Texas.

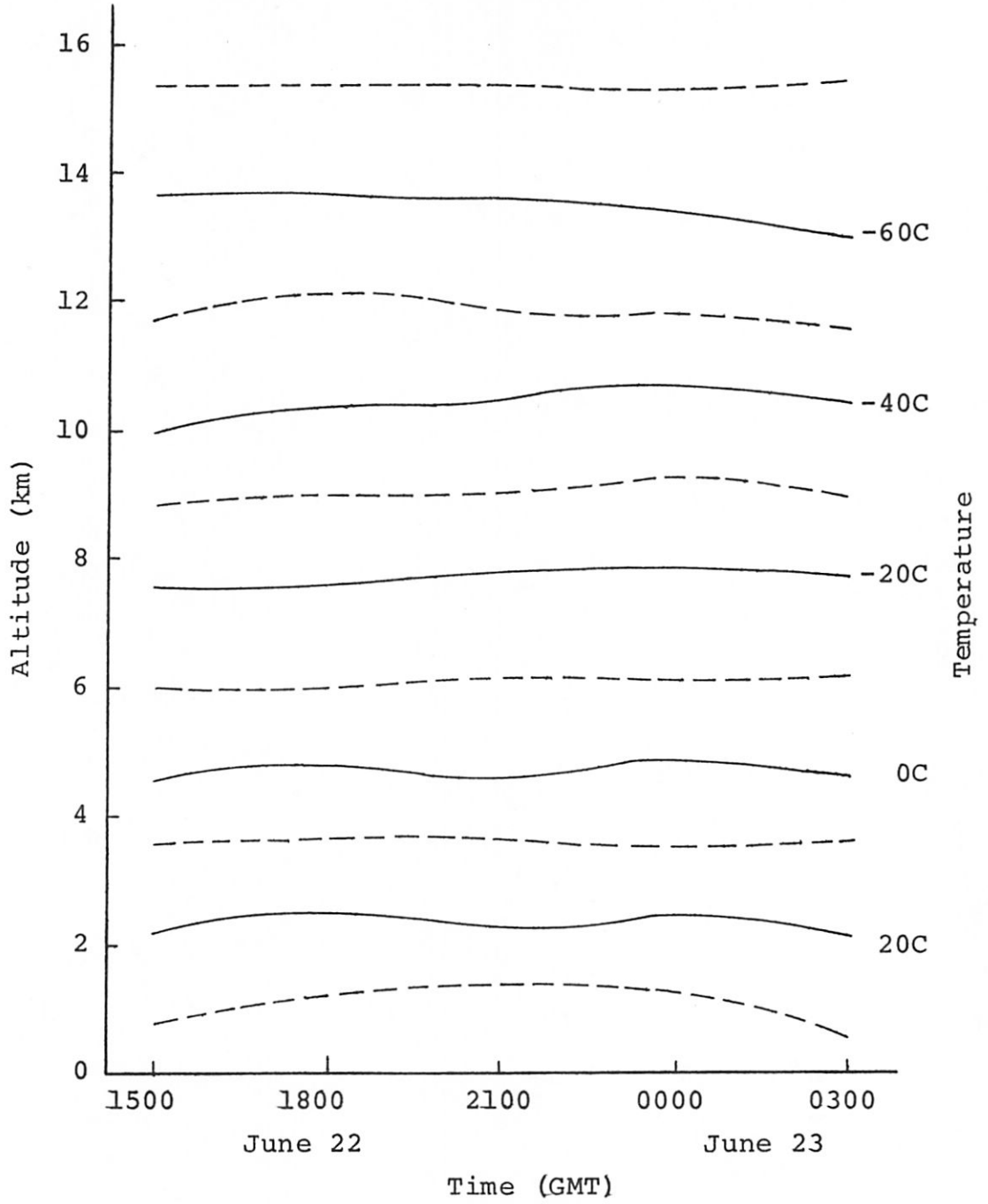


Figure 2-11 Same as Figure 2-9 for Post, Texas.

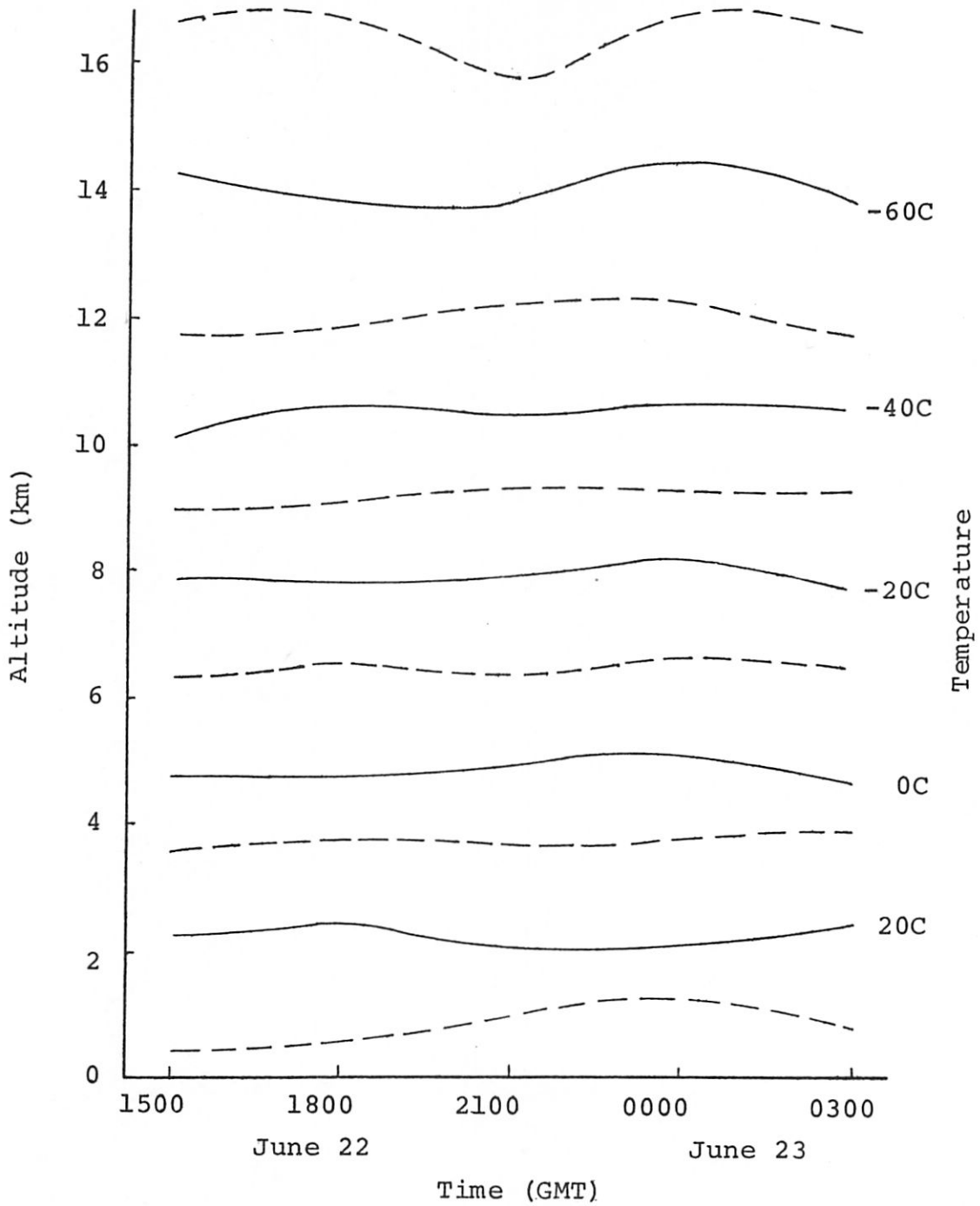


Figure 2-12 Same as Figure 2-9 for Robert Lee, Texas.

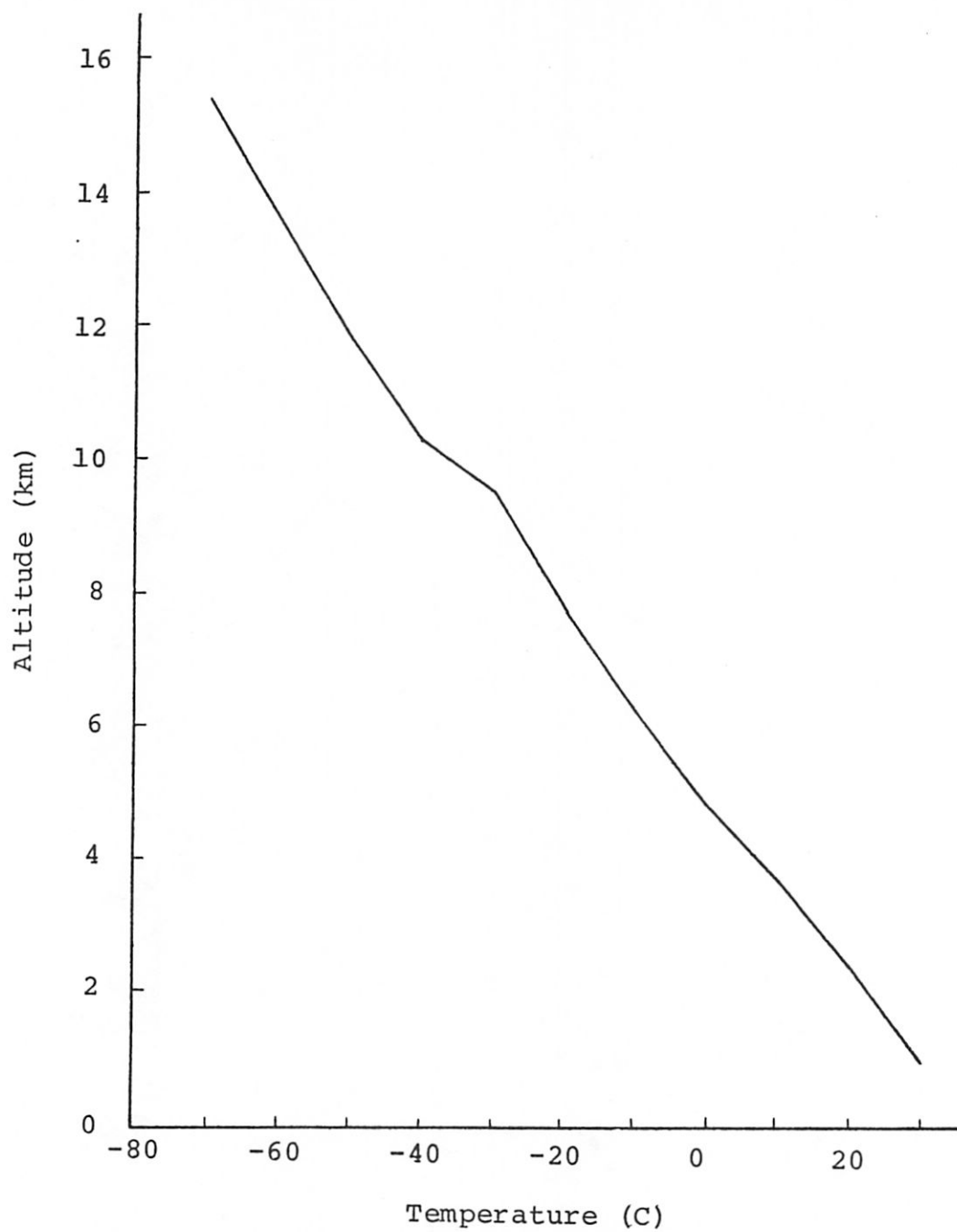


Figure 2-13 The "average" sounding for the study area on 22 June 1976.

Table 2-2 Time-averaged isotherm heights for the four rawinsonde stations in the study area. Also given are the averaged heights, the standard deviation of height and the maximum deviation from the average.

Temperature (C)	Big Spring (m)	Midland (m)	Post (m)	Robert Lee (m)	Averaged height, $\bar{h}$ (m)	Standard deviation (m)	$(h_i - \bar{h})_{\max}$ (m)
0	4,794	4,858	4,726	4,894	4,818	74	88
-10	6,128	6,230	6,132	6,467	6,239	159	228
-20	7,691	7,787	7,685	7,881	7,761	93	120
-30	8,988	9,044	9,010	9,168	9,053	80	115
-40	10,213	10,343	10,348	10,478	10,346	187	133
-50	11,654	11,854	11,811	11,919	11,810	195	156
-60	13,351	13,445	13,434	14,034	13,566	315	468

In order to investigate the offset and accurately match VIS and IR data, two data sets of identical resolution are required. A 216x216 array was considered by dividing each IR pixel into 32 new IR subareas. Although this method would have kept all of the original VIS information, the extensive interpolation of IR data did not produce patterns consistent with the VIS data. In addition, use of the highly expanded IR data set would have greatly increased computation times for analysis. To produce identical resolutions in VIS and IR data sets, a 54x54 array size was also considered. In this method, every new VIS data area would replace a 4x4 array of original VIS pixels. This method was tested by producing computer-generated cloud patterns from the 54x54 VIS data array. However, it was found that many of the small clouds disappeared, indicating that the combination of this many data points resulted in too much smoothing. As a result of the testing, an array of 108x108 pixels (approximately 2.4 km resolution) was selected as the optimum array size. This resolution involved both compressing the VIS data and stretching the IR data. It was found that no important cloud information was lost as a result of compressing the VIS data to an 108x108 array. By utilizing the interpolation technique described below, the stretched 108x108 IR array was able to reproduce cloud patterns which agreed well with the higher resolution VIS data.

The magnitude of radiance at a certain point is inversely

proportional to the square of the distance between the point and light source. For compressing the 216x216 arrays of VIS data, each pixel of the reduced 108x108 array was located at the center of a 2x2 array of four pixels from the original 216x216 VIS array. In the computation to obtain the new VIS data value, all surrounding data points around the new data point were considered. Using the inverse square relationship, it was found that data points beyond the four nearest original data values are at a sufficient distance from the averaging center to have small weighting factor less than 3% and could be neglected. Therefore, the 2x2 averaged VIS data were used to form 108x108 array which became the new VIS data set.

As shown in Figure 2-14, each original IR data area of the 27x54 array is stretched into eight subareas to form a new 108x108 array. Neglecting any original pixels whose contribution to the subpoint brightness is less than 8%, the weighting factors are given in Table 2-3 for the two different relative positions A and B of data sub-points.

Utilizing the VIS and IR pictures which were displayed on the ADVISAR and other computer-generated plotted maps, it was determined that a misalignment existed between these two data sets. By translating the stretched IR data four pixels to the left and two pixels upward relative to the VIS data, the misalignment was removed. Accordingly, these well-matched VIS and IR digital data sets were utilized for all data analysis described in the next chapter.

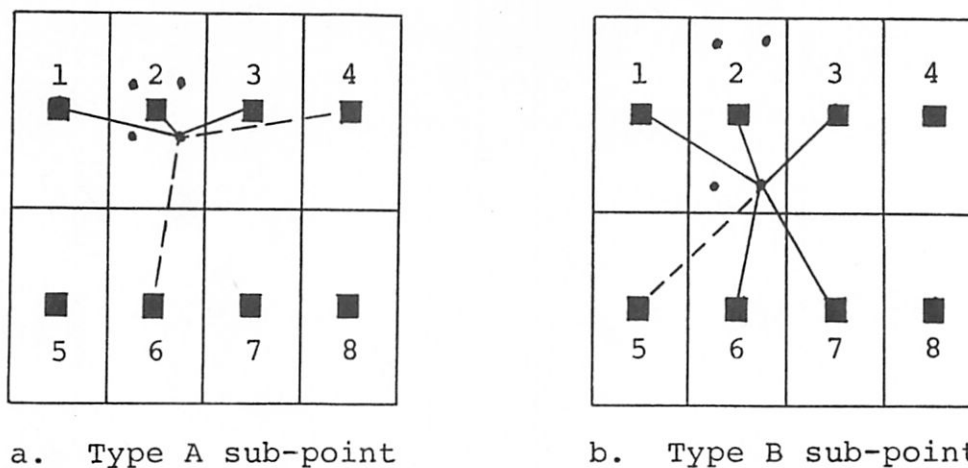


Figure 2-14 Pictorial representation of data points used in stretching infrared radiance data.  
 ■ represents an original data point and  
 • represents an interpolated sub-point.

Table 2-3

Weighting factors used in stretching infrared radiance data

<u>Type A sub-point</u>		<u>Type B sub-point</u>	
<u>Point</u>	<u>Weight</u>	<u>Point</u>	<u>Weight</u>
2	.87838	2	.39551
3	.08784	3	.21973
1	.03378	6	.15212
4	.01757	1	.11632
6	.01757	7	.11632
NOT USED		5	.07910

CHAPTER III  
DATA ANALYSIS

3.1 Cloud Properties Analysis

A computer cloud summary program to analyze cloud radiance data was obtained from Colorado State University (CSU) and has been adapted and modified for the present study. This cloud summary program searches an array of VIS data and locates clouds. A primary input parameter is the critical brightness value,  $VIS_{crit}$ , discussed in Section 2.2, to distinguish cloud from underlying non-cloud background. Based on this value, an isopleth of  $VIS_{crit}$  is found to define the outline of a cloud. The total number of digital points and brightness values within a cloud region are used to determine the mean cloud brightness and size. Using the mean and individual brightness value, the standard deviation of cloud brightness is determined. In order to obtain the geometric cloud center, the cloud pixels are counted row by row until the median point is reached. The process is repeated column by column to find the median column. The intersection of this certain row and column is defined as the geometric center of the cloud. The brightness center is obtained in the same manner, using instead individual brightness values and their sum. Meanwhile, the location of the maximum brightness of the cloud is determined.

After considering all clouds in the data set, the

following values are computed: (1) percentages of cloud and non-cloud within the region, (2) cloud and non-cloud area mean brightness values, (3) the frequency distribution of all data points, (4) the frequency distribution of cloud mean brightness values and (5) the frequency distribution of cloud size.

### 3.1.1 Cloud populations and percent cloud cover

The cloud summary program was employed using the cloud/non-cloud critical values selected for different analysis times to obtain the number of clouds and the percentage of cloud cover. A minimum cloud size of four pixels, equivalent to a circular cloud of 3.3 km diameter, was selected to define the minimum cloud size of interest. Any cloud with the size below 3.3 km diameter was neglected in the cloud population computer program. The total cloud cover region was then compared with the entire area to obtain the percentage of cloud cover.

The smallest clouds were sequentially eliminated from the total number of clouds to obtain a cloud count which best matched the total number of clouds derived from satellite photographic imagery in an earlier study (Jurica, 1977). Because the viewing times of satellite images from GOES EAST and radiance data from GOES WEST are not coincident, an average of the cloud count 15 min before the hour and 15 min after the hour was used to match the cloud-counts derived from imagery at times from 1800 to 2200 GMT on 22

June 1976. Comparisons of the two data sets were made at one hour intervals. A minimum cloud size of eight pixels, with an equivalent circular cloud diameter of 4.7 km was found to correspond best to the smallest isolated cloud recognizable from satellite imagery. The maximum isolated cloud size required in order to match the number of isolated clouds found in the imagery study was found to contain 37 pixels, with a diameter of 10.0 km. Clouds with size larger than 37 pixels were classified as area clouds, which includes large isolated convective clouds and widespread deep convective or stratiform clouds.

Comparisons of numbers of clouds and percentage of cloud cover obtained from satellite radiance data and from imagery are shown in Table 3-1. There is close agreement in cloud coverage between the two methods. Since the photographic imagery study area was divided into nine subareas, the percent cloud cover was observed for each subarea. Therefore, a more accurate estimate of percent cloud cover over the total area was obtained by averaging these nine values. The largest deviation of cloud coverage between radiance data and imagery, 3%, appears at 2100 GMT. At other times only 1 or 2% difference is observed. Table 3-1 also shows that the numbers of isolated and area clouds in the radiance data study are close to that in the imagery study at 1800 and 1900 GMT. At 2000 GMT more isolated clouds were detected from the imagery. Through the ADVISAR display

Table 3-1 Comparison of numbers of clouds and percentage of cloud cover from satellite radiance data and imagery

Time (GMT)	Total number of clouds		Number of medium isolated convective clouds $4.7 \leq D \leq 10^*$		Number of large isolated and widespread clouds $D > 10^*$		Percent cloud cover (%)	
	Radiance Data	Imagery	Radiance Data	Imagery	Radiance Data	Imagery	Radiance Data	Imagery
1800	53	57	29	33	24	24	25	26
1900	46	45	26	25	20	20	25	27
2000	36	50	19	32	17	18	24	23
2100	34	29	24	15	10	14	20	23
2200	45	27	28	13	17	14	17	19

\*D is cloud diameter in km

system, two large cluster-area clouds were found on each of the cloud pictures at 1945 and 2015 GMT located in the eastern and western parts of the study area: one located from Hamlin to Robert Lee, the other located from Seminole to Midland. The sizes of these two cluster-area clouds are about 4,000 pixels, with an equivalent circular diameter of 104 km. The computer cloud summary program treats several small clouds as a large cluster-area cloud if the clouds are linked at even a few boundary points. However, in the imagery study these clouds may be separated. Therefore, more isolated clouds were detected from imagery at 2000 GMT. By 2200 GMT the solar zenith angle had increased to  $45^{\circ}$  the brightness of the scene was reduced and fewer small isolated clouds could be distinguished from the underlying surface in the photographic imagery. However, by adjusting the critical value to distinguish cloud from non-cloud the cloud summary program overcomes this problem, leading to greater numbers of isolated clouds than seen in the imagery.

The contents of Table 3-1 are displayed in Figure 3-1. The three curves indicate the variation of the number of clouds in several different categories: total number of clouds, number of large and widespread clouds, and number of medium isolated convective clouds, computed with the cloud summary program for the study period. Imagery results are also indicated from 1800 to 2200 GMT in this figure

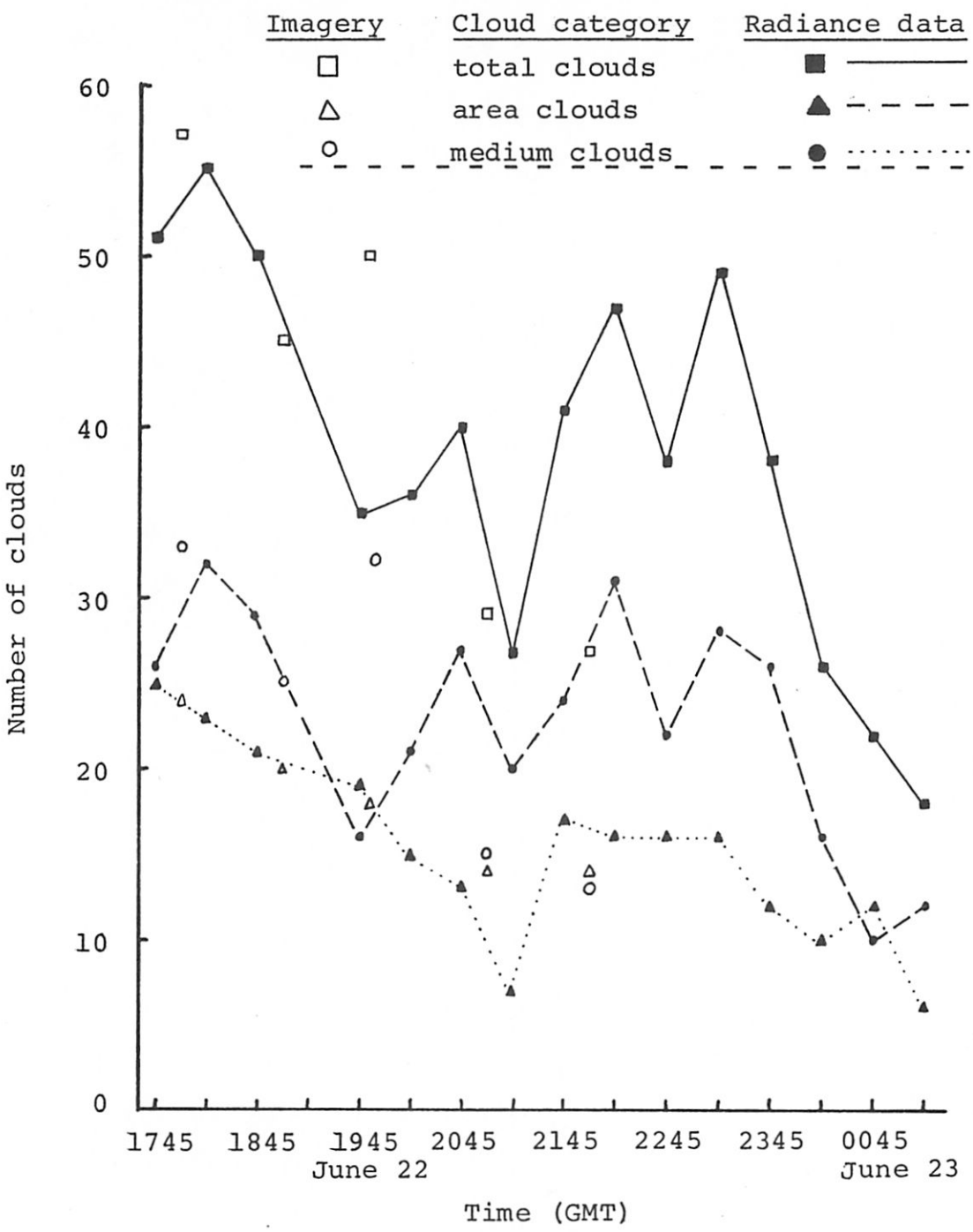


Figure 3-1 Variation of the number of clouds in three different size categories derived from radiance measurements. Results obtained from photographic images are shown with open symbols.

using open symbols for the three categories. Looking at Figure 3-1, it is found that except for a low number at 2115 GMT, when most area clouds merged into a single large cluster-area cloud, the number of large and widespread area clouds decreased with time reaching a minimum value of 6 at 0115 GMT. The number of medium isolated convective clouds varied with time about the value 24 and then decreased rapidly late in the day.

Comparing the cloud size between satellite radiance data and photographic imagery, it is possible to separate clouds into several categories according to their size:

1. Tiny clouds, less than 4 pixels, the corresponding circular cloud diameter (D) less than 3.3 km, neglected in this study;
2. Isolated convective cloud:
  - a. Small clouds, with 4 to 7 pixels,  $3.3 \text{ km} \leq D < 4.7 \text{ km}$ , usually a fair weather cumulus cloud;
  - b. Medium clouds, with 8 to 37 pixels,  $4.7 \text{ km} \leq D \leq 10 \text{ km}$ , mostly cumulus congestus;
  - c. Large clouds, with 38 to 148 pixels,  $10 \text{ km} < D \leq 20 \text{ km}$ , usually identified as cumulonimbus;
3. Widespread deep convective or stratiform cloud with more than 148 pixels,

D > 20 km, identified as a widespread deep convective cloud for high brightness radiance data or as an area of stratiform cloud for low brightness.

The numbers of clouds in the above described categories are shown in Table 3-2 for the entire period. It shows that at most times the number of medium isolated convective clouds dominated the total number of clouds; however, at 0045 and 0115 GMT there are more small isolated clouds. From this table it is seen that there are only a few widespread area clouds, representing one-tenth of the total number of clouds; however, it should be noted that these few clouds contribute 80 to 90% of the cloud cover in the study region. A discussion of this point follows later in this section.

The cloud size frequency distribution was utilized to prepare a table showing the corresponding cloud size for a cumulative percentage of total cloud number at each time in the entire period. Table 3-3 summarizes the results from 1745 to 0115 GMT in 2.5 hr intervals. For example, at 2245 GMT 50% of all clouds consisted of 16 or fewer pixels, corresponding to a diameter of 6.6 km. A similar pattern occurred from 1745 and 0045 GMT. The first 25% of all clouds are small isolated clouds, the next 50% are medium isolated clouds, and the remaining 25% are large isolated or widespread area clouds. At 0115 GMT 55% are small isolated

Table 3-2 Number of clouds in various size categories

Time (GMT)	Small Isolated	Medium Isolated	Large Isolated	Widespread Area	Total
22 JUNE					
1745	14	26	20	5	65
1815	16	32	14	9	71
1845	15	29	14	7	65
1945	10	16	15	4	45
2015	14	21	11	4	50
2045	13	27	4	9	53
2115	16	20	4	3	43
2145	21	24	11	6	62
2215	19	31	8	8	66
2245	12	22	10	6	50
2315	15	28	14	2	59
2345	9	26	9	3	47
23 JUNE					
0015	10	16	6	4	36
0045	12	10	5	7	34
0115	24	12	4	2	42

Table 3-3 Cumulative distribution of cloud size as a function of time during the study period.

% of clouds of given size		1745GMT 65*	2015GMT 50	2245GMT 50	0115GMT 42
Small Isolated	10	5** (3.7)***	5 (3.7)	6 (4.0)	4 (3.3)
	20	7 (4.4)	6 (4.0)	7 (4.4)	4 (3.3)
Medium Isolated	30	10 (5.2)	8 (4.7)	9 (4.9)	4 (3.3)
	40	12 (5.7)	11 (5.5)	12 (5.7)	5 (3.7)
	50	15 (6.4)	14 (6.2)	16 (6.6)	6 (4.0)
	60	23 (7.9)	19 (7.2)	24 (8.1)	8 (4.7)
Large Isolated	70	49 (11.5)	36 (9.9)	39 (10.3)	14 (6.2)
	80	63 (13.1)	58 (12.5)	107 (17.0)	18 (7.0)
	90	137 (19.3)	89 (15.5)	162 (21.0)	91 (15.7)
Widespread Area	100	6415 (131.9)	6382 (131.6)	2890 (88.6)	12722 (185.8)

\* total number of clouds at GMT time above

\*\* number of pixels in cloud

\*\*\* equivalent diameter of circular cloud in km

clouds and only 5% are widespread area clouds.

Through the computer cloud summary program, the percent cloud cover was computed. The percent cloud cover, together with the contributions from widespread clouds and isolated convective clouds are shown in Figure 3-2. A comparison with the hourly radar summaries (Figure 2-5) obtained from the National Weather Service showed that a widespread echo was located in the eastern portion of our study area moving toward the southeast out of the region at 1735 GMT. Meanwhile, a new echo began to develop in the northwest portion of the study area. Therefore, the total percent cloud cover remained nearly constant until 2045 GMT. By 2115 GMT the widespread echo had moved away from the eastern boundary and the cloud cover reaches a minimum value at 2215 GMT. Subsequently, the percent cloud cover increased rapidly as clouds with strong vertical development moved into the region from the west.

Table 3-4 shows the relative contributions to total cloud cover from different size categories of clouds. In Table 3-3 it was seen that 60 to 80% of all clouds have a diameter less than 10 km. Nevertheless, Table 3-4 shows that such small and medium isolated clouds contribute only 2 to 8% of the cloud cover. Despite the fact that there are only a few widespread area clouds, they contribute 80 to 96% of the cloud cover. For example, at 0115 GMT there is one cloud with 12,722 data points, the corresponding diameter

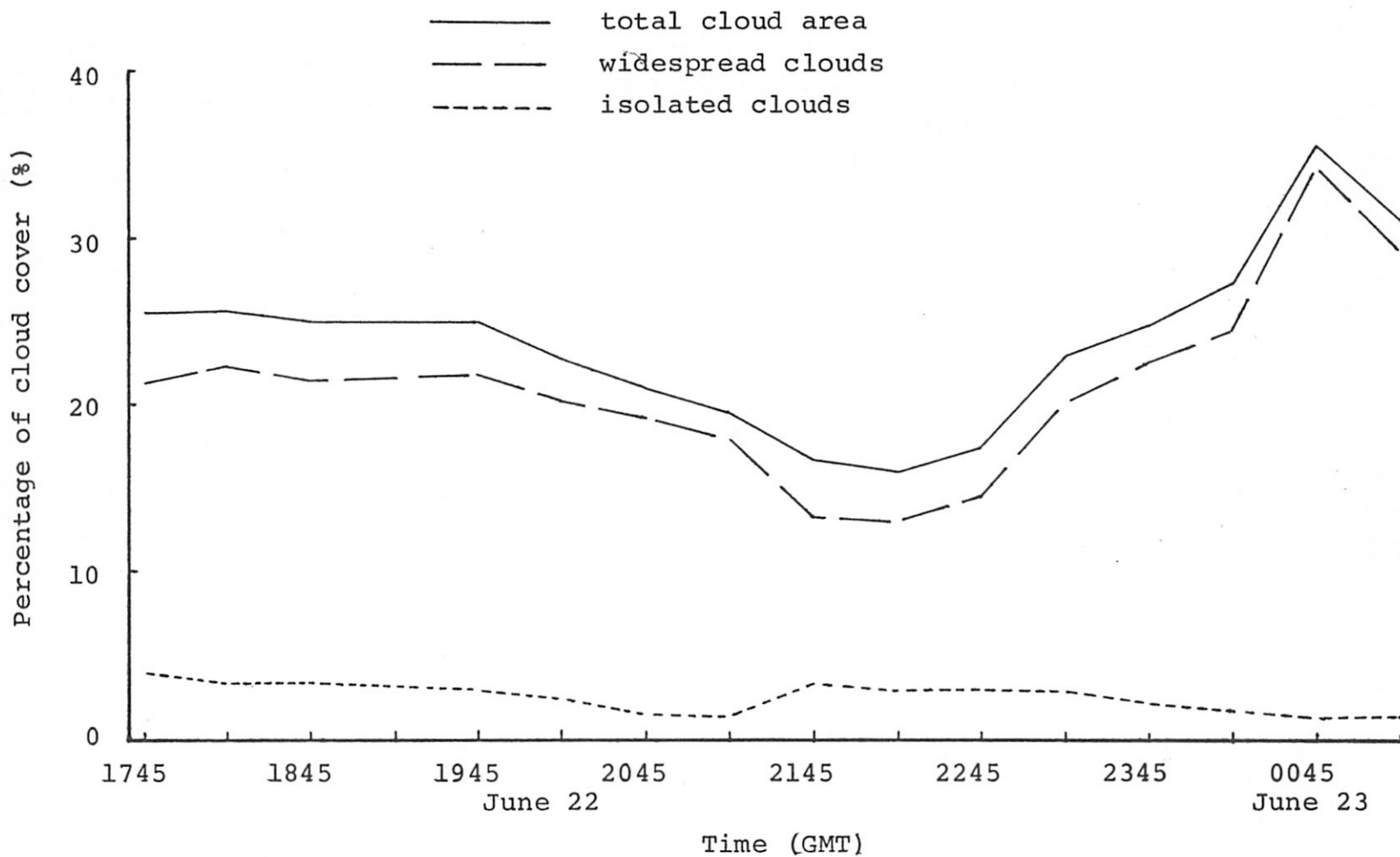


Figure 3-2 The percentage of cloud cover for total cloud area, widespread clouds and isolated clouds.

Table 3-4 Total percent cloud cover and the relative contribution from clouds of various diameters D(km).

Time (GMT)	Total percent of cloud cover	Small Isolated $3.3 \leq D < 4.7$	Medium Isolated $4.7 \leq D \leq 10$	Large Isolated $10 < D \leq 20$	Widespread Area $D > 20$
22 JUNE					
1745	25.4%	0.6%	3.0%	12.5%	83.9%
1815	25.7	0.7	4.6	7.9	86.8
1845	25.0	0.7	4.1	9.3	85.9
1945	25.0	0.4	2.1	9.7	87.7
2015	22.7	0.7	3.3	7.0	89.0
2045	21.0	0.7	4.1	3.2	92.0
2115	19.5	1.0	3.8	3.3	92.0
2145	16.7	1.5	5.9	12.7	79.9
2215	16.0	1.4	6.9	10.4	81.3
2245	17.6	0.8	4.9	11.7	82.6
2315	23.0	0.8	4.2	7.4	87.6
2345	24.8	0.5	3.5	4.7	91.4
23 JUNE					
0015	26.3	0.4	2.2	4.3	93.1
0045	35.7	0.4	1.1	2.3	96.3
0015	31.0	0.8	1.3	2.7	95.2

for a circular cloud being 186 km, among 46,656 total data points; this one cloud represented 88% of the total cloud coverage (given as 31% in Table 3-4).

In summary, although most of the clouds in this study are isolated convective clouds, these clouds contribute a low percentage of the total cloud cover. A small number of widespread convective or stratiform clouds contribute 80% (2145 GMT) to 96% (0045 GMT) of the cloud cover. Although the analyses of radiance data and imagery produced nearly the same values of percentage cloud cover, there were differences in the number of clouds obtained from the two data sources. Through a comparison of the differences between the two sets of results, it was found that the radiance data yielded more reliable cloud counts because of the ability to use a time-dependent cloud/non-cloud critical brightness value. One weakness of the radiance data analysis occurs when the cloud summary program identified two clouds whose boundaries touch as a single cloud. Nevertheless, both the good spatial resolution of the radiance data and the consistency of results permitted by an objective analysis method make the radiance data an excellent tool for atmospheric research.

### 3.1.2 Cloud brightness analysis

The appearance of a satellite-observed cloud depends

upon the VIS brightness values which will vary with different solar zenith angles. Late in the day, as the solar zenith angle becomes large, the brightness values decrease as attenuation removes energy as a result of the longer path. A visible brightness frequency distribution table was constructed for the study area at each time during the study period. The visible brightness frequency distribution curves from 1745 to 0115 GMT at two and half hour intervals are given in Figure 3-3. The brightness scale at each time is plotted relative to the cloud/non-cloud critical value for that time. The mode of the brightness frequency distribution at 1745 GMT occurs 28 units below the  $VIS_{crit}$  value. From 1815 to 2345 GMT all modes are at a value of 24 units below  $VIS_{crit}$ . After 2345 GMT, the mode became closer to the  $VIS_{crit}$  value. At 0115 GMT the mode is only 12 units less than the  $VIS_{crit}$  value. Not only was the mode for 0115 GMT closest to its  $VIS_{crit}$  value, but the width of the brightness spectrum was narrower than the curves at other times. From the several frequency distributions, one can conclude that at 0115 GMT, when the non-cloud data points are closely spaced and only slightly below the value of  $VIS_{crit}$ , it will be difficult to distinguish clouds from the underlying non-cloud background.

Cloud points were found based on the cloud/non-cloud brightness critical value. Mean brightness values for both cloud and non-cloud were obtained. To permit a more detailed

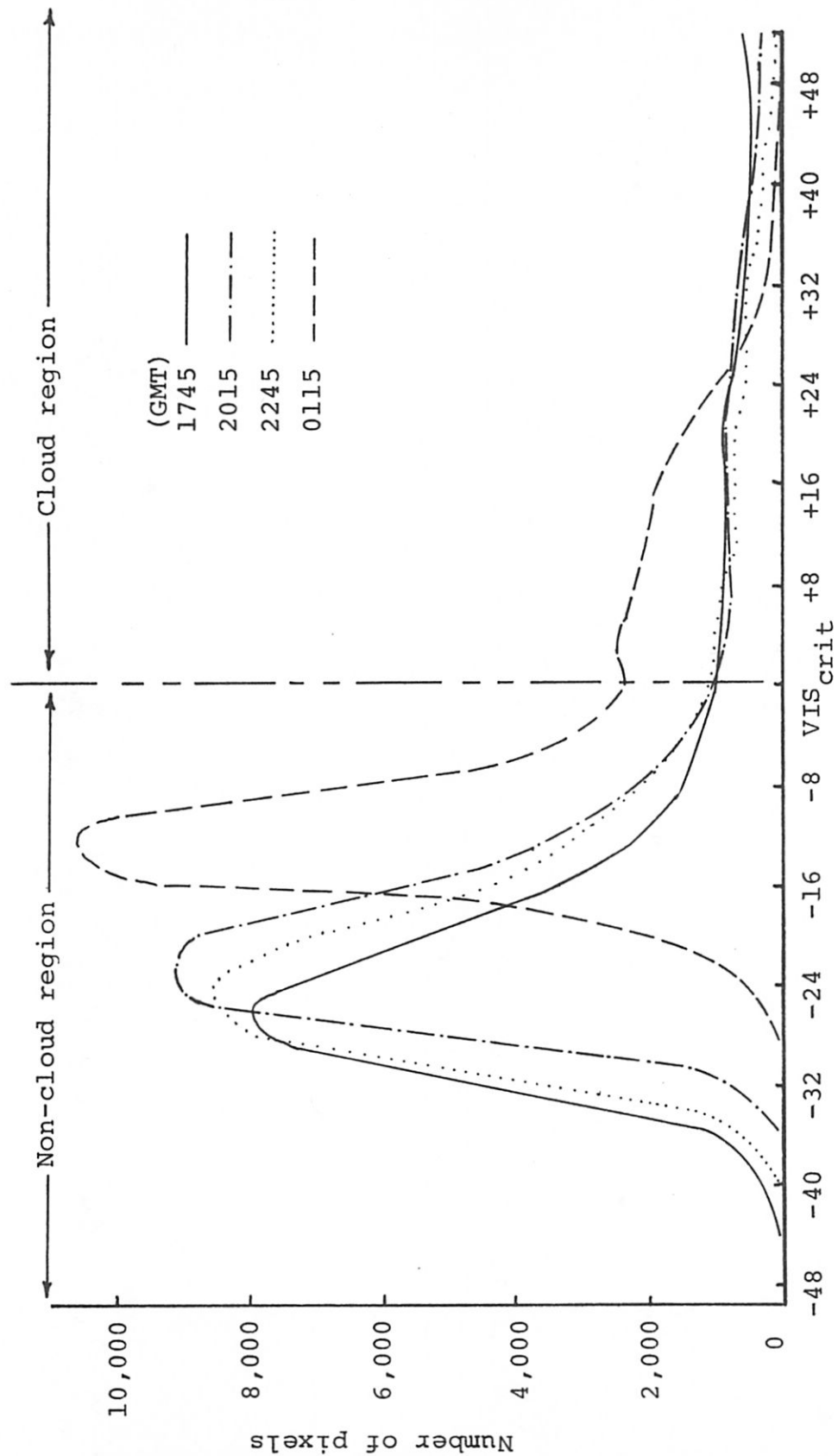


Figure 3-3 Curves of the frequency distribution of visible radiance values. All curves are plotted relative to the critical visible radiance value, cloud points to the right and non-cloud points to the left of this value.

analysis, individual mean brightness values were calculated for four different categories of cloud size. The results are shown in Table 3-5. It can be seen that the mean brightness of all clouds was close to that of a widespread cloud. This phenomenon is quite reasonable considering the previous discussion; widespread area clouds dominate the total cloud coverage. In this case study the widespread clouds are primarily deep convective clouds. Therefore, these widespread clouds will dominate the mean brightness of the entire cloud area. The isolated convective cloud has a low mean brightness value relative to the critical cloud/noncloud value, as can be seen in Figure 3-4. This figure displays the mean brightness  $\overline{\text{VIS}}$  of the four cloud size categories relative to  $\text{VIS}_{\text{crit}}$  as a function of time. In addition, the widespread convective cloud brightness values are the greatest of all four cloud-size classes. This remains true even though the relative brightness of the widespread convective clouds undergoes the most decrease from 1745 to 0115 GMT. These relationships appear to be directly related to cloud size. The small clouds will have a greater proportion of boundary points, with values near  $\text{VIS}_{\text{crit}}$ , than the larger clouds. As a result, the brightness of the small isolated clouds is nearly constant and near to the  $\text{VIS}_{\text{crit}}$  value at all times of day.

Because the principal interest in this study is with isolated clouds, the overall mean brightness value for

Table 3-5 Mean brightness for total clouds and four different categories of clouds

Time (GMT)	Total cloud	Small isolated convective cloud	Medium isolated cloud	Large isolated cloud	Widespread cloud
22 June 1745	147	123	127	133	150
1815	146	123	129	135	148
1845	144	123	127	131	146
1945	146	122	127	134	148
2015	144	122	127	133	146
2045	144	122	127	131	145
2115	141	123	128	131	142
2145	135	119	126	128	137
2215	128	115	118	121	130
2245	126	112	116	119	128
2315	120	103	106	109	122
2345	108	95	96	98	109
23 June 0015	94	82	83	86	95
0045	79	65	67	68	79
0115	60	50	50	52	61

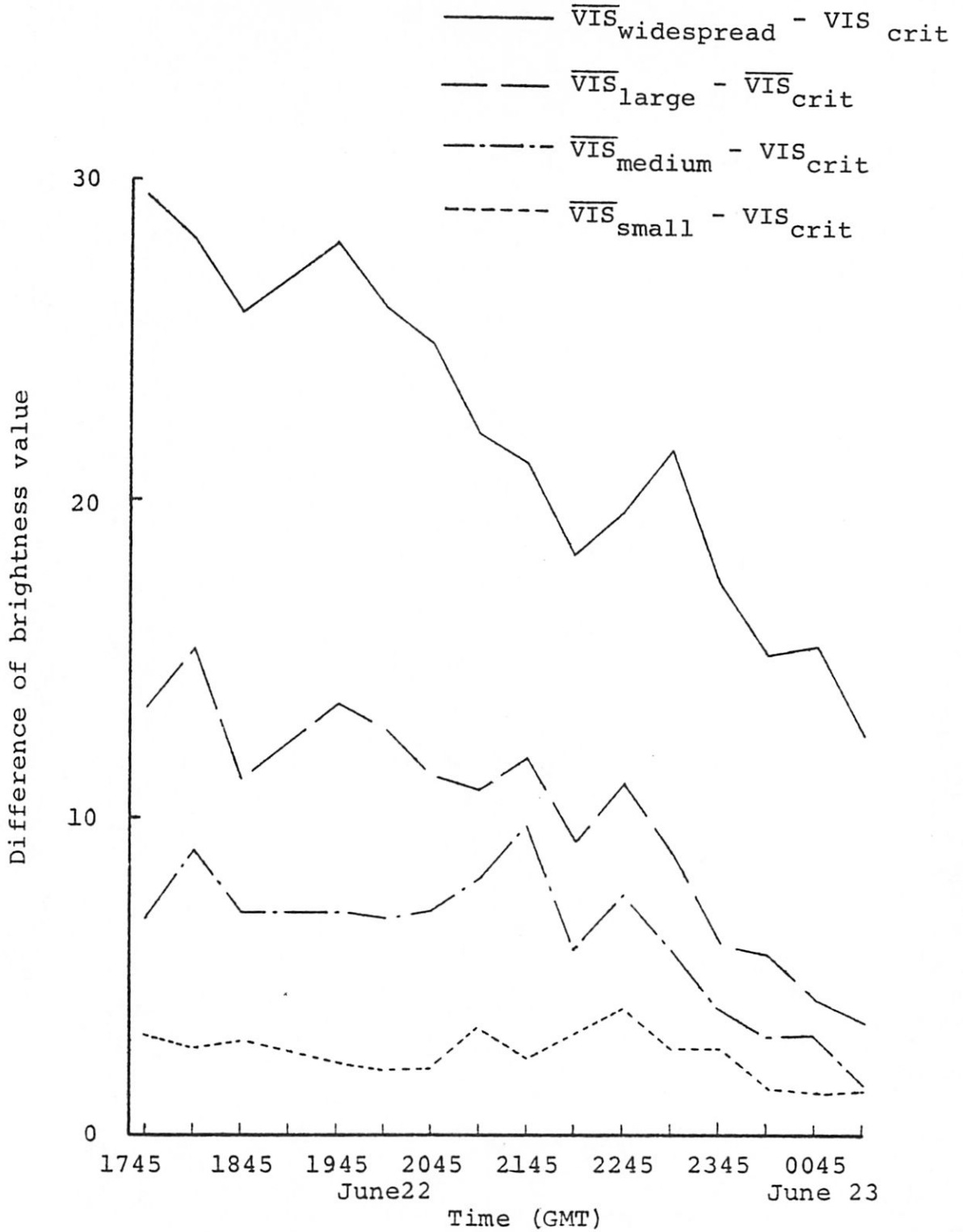


Figure 3-4 Differences between the mean brightness value ( $\overline{VIS}$ ) and the critical brightness value ( $VIS_{\text{crit}}$ ) for several categories of clouds.

clouds with size from 3.3 to 20 km diameter was compared with the underlying non-cloud mean brightness value. Both the ratio and difference of these two parameters were computed and are shown in Figure 3-5. It is found that the ratio of the mean brightness of an isolated cloud to that of non-cloud background decreased from 1745 to 2045 GMT and then increased until reaching a maximum value of 1.41 at 0115 GMT. The difference curve decreases slightly at first until 1845 GMT and then remains nearly constant until 2245 GMT. After 2245 GMT the difference decreases until the final time, reaching a minimum value of 15. From Figure 3-5 it appears that late in the day the brightness ratio can be used to distinguish the cloud from non-cloud background. However, the small differences between isolated cloud and non-cloud brightness demonstrate the difficulty involved in identifying clouds at low sun angles. The brightness frequency distribution curve in Figure 3-3 shows that the frequency mode at 0115 GMT is close to its critical value and that the brightness data have a narrow spread. These facts further support the contention that it is difficult to distinguish cloud from non-cloud background late in the day.

A cumulative distribution of mean cloud brightness was obtained for every time in the study period and is summarized in Table 3-6. It was found that 50% of all clouds have a mean brightness value 6 to 8 units above the

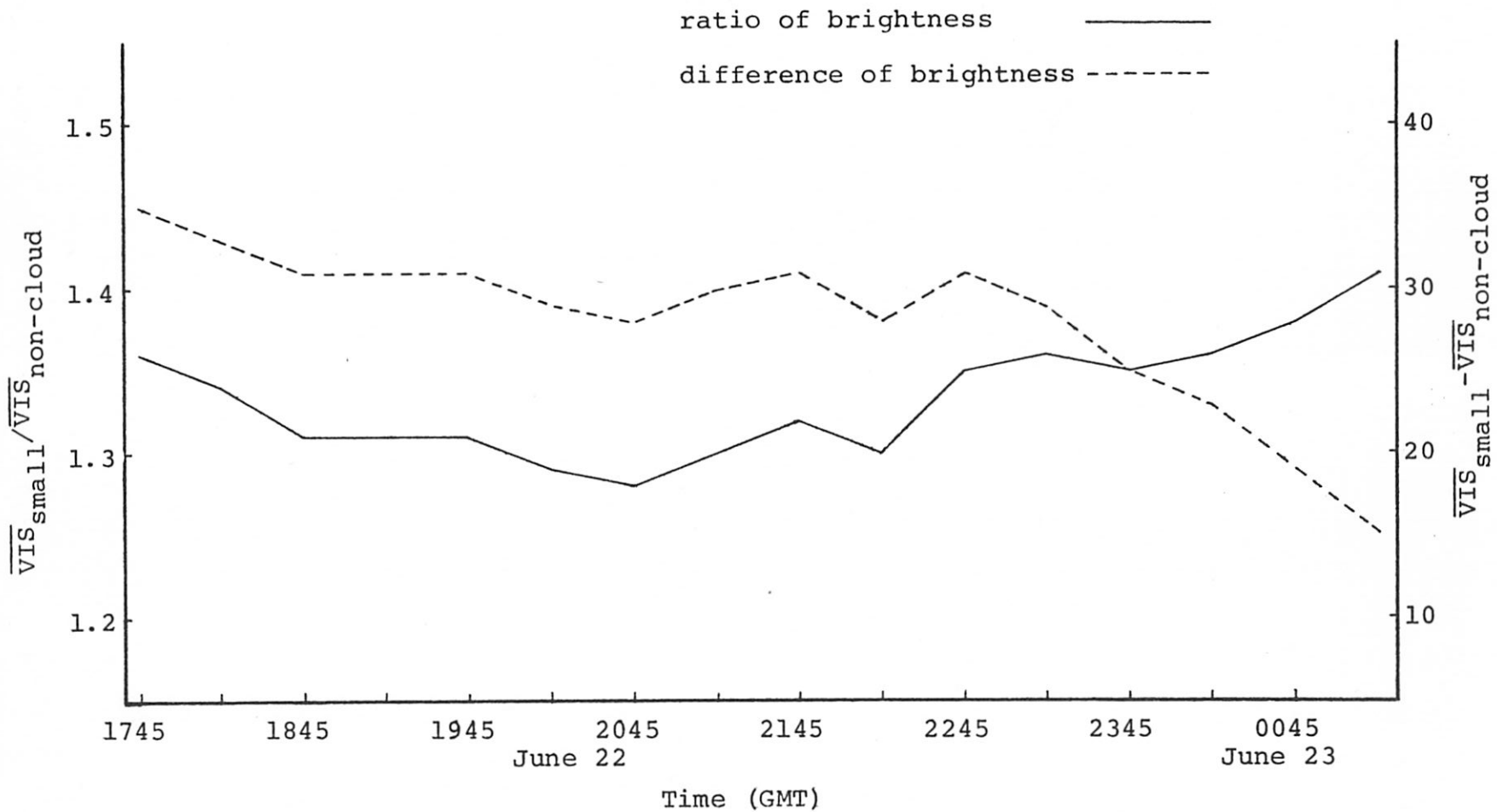


Figure 3-5 The ratio of and difference between mean brightness of small isolated clouds and mean brightness of non-cloud.

Table 3-6 Cumulative distribution of cloud mean brightness above the critical cloud/non-cloud value

% of cloud given mean brightness	1745GMT	2015GMT	2245GMT	0115GMT
10	+ 2*	+ 1	+ 2	+ 0
20	3	2	3	1
30	5	2	4	1
40	7	4	6	1
50	8	6	7	1
60	9	8	9	2
70	11	9	10	2
80	12	11	13	3
90	16	19	16	4
100	34	27	21	13

\* the number of counts relative to the appropriate visible critical value

$VIS_{crit}$  value from 1745 to 2245 GMT. However, by 0115 GMT 50% of all clouds have a mean brightness only one unit above  $VIS_{crit}$ . Comparing the cloud size frequency distribution table (Table 3-3) and cloud summary statistics at 0115 GMT, it was found there are many small isolated clouds with low brightness values located near Odessa and Snyder, making cloud identification more difficult even with the ADVISAR display. However, the distinct advantage of the video display technique is made particularly clear in this instance. The cloud/non-cloud critical brightness value is selected using several marginal but distinguishable isolated clouds, and then is applied to the whole scene without any subjective interpretation needed.

The mean brightness of each individual cloud was determined time by time for the whole period. The mean brightness of each isolated cloud of less than 149 pixels was compared with its size. Figure 3-6 was chosen as representative of the results and shows the distribution pattern at 1745 and 2245 GMT, the first and middle hours of the period. It was seen earlier, in Figure 3-4, that cloud brightness increased with size. However, Figure 3-6 shows that the correlation between these two parameters is small, indicated by the large scatter of points. In both figures it is seen that any cloud containing less than 20 pixels will have a mean brightness no more than 12 units above its critical value. However, for the larger

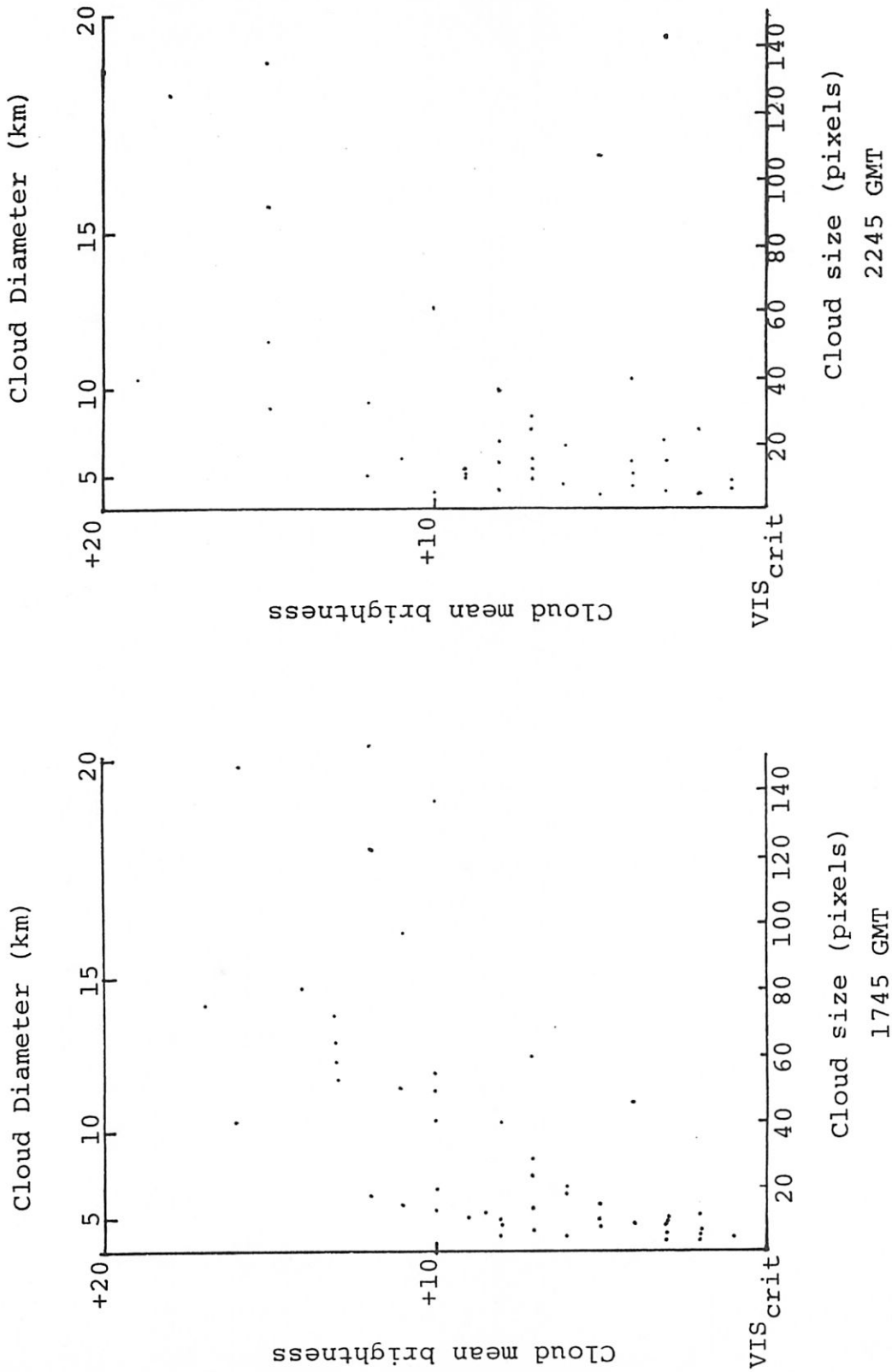
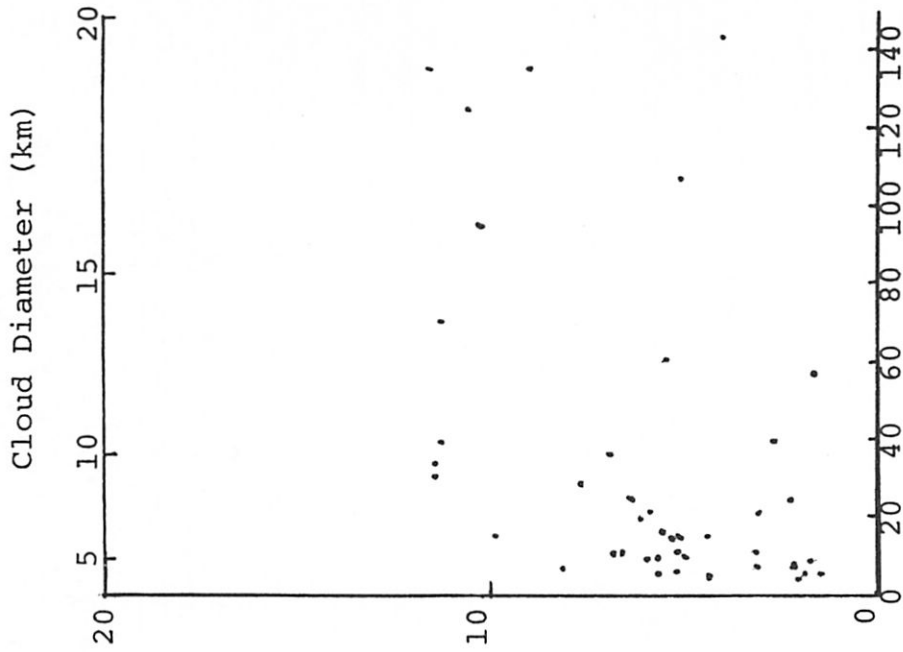


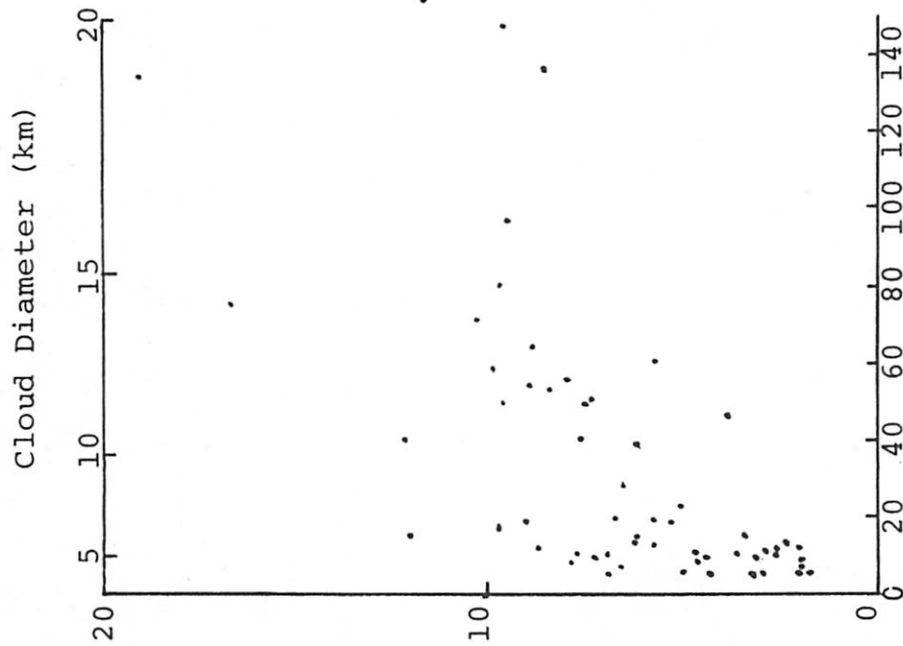
Figure 3-6 The comparison of cloud mean brightness and cloud size at 1745 and 2245 GMT on 22 June 1976

clouds the mean brightness values are widely scattered. For example, at 2245 GMT, a cloud with the size of 143 pixels has a mean value only 3 units above its visible critical value, while another cloud with 135 pixels has a mean brightness value 18 units above its visible critical value.

The standard deviation of brightness for all isolated clouds with size less than 149 pixels was compared with the cloud size. Figure 3-7 shows these comparisons at 1745 and 2245 GMT. Obviously, the correlation between the standard deviation of brightness and cloud size is poor. Although the standard deviation of brightness does not have good correlation with its size, it appears to be highly correlated with its mean brightness value. A linear regression line and the correlation coefficient between the standard deviation of the brightness and the difference between cloud mean brightness,  $\overline{VIS}$ , and its visible critical value were found and are given in Table 3-7. From this table, very consistent values of slope and intercept of the regression line are found through the whole period. A high correlation coefficient was found as well, varying from 0.99 at 2015 GMT. Figure 3-8 shows the standard deviation of brightness versus mean brightness value at 1745 and 2245 GMT; the regression lines are drawn in the figure. It shows that the higher the cloud mean brightness above the critical cloud/non cloud value, the higher the standard deviation of brightness.



Cloud size (pixels)  
2245 GMT



Cloud size (pixels)  
1745 GMT

Figure 3-7 The comparison of standard deviation of cloud brightness and cloud size at 1745 and 2245 GMT on 22 June 1976.

Table 3-7 Parameters for a regression line, of the form  $y = a + bx$ , between standard deviation of brightness,  $y$ , and mean brightness,  $x$ .

Time (GMT)	Intercept (a)	Slope (b)	Correlation coefficient
June 22			
1745	1.18	0.65	0.96
1815	1.21	0.61	0.97
1845	1.12	0.67	0.97
1945	1.03	0.69	0.98
2015	1.06	0.66	0.99
2045	1.16	0.65	0.98
2115	1.04	0.67	0.97
2145	0.68	0.72	0.98
2215	0.94	0.70	0.96
2245	1.17	0.64	0.94
2315	1.43	0.64	0.96
2345	1.06	0.65	0.97
June 23			
0015	0.76	0.71	0.97
0045	0.73	0.77	0.96
0115	0.84	0.63	0.91

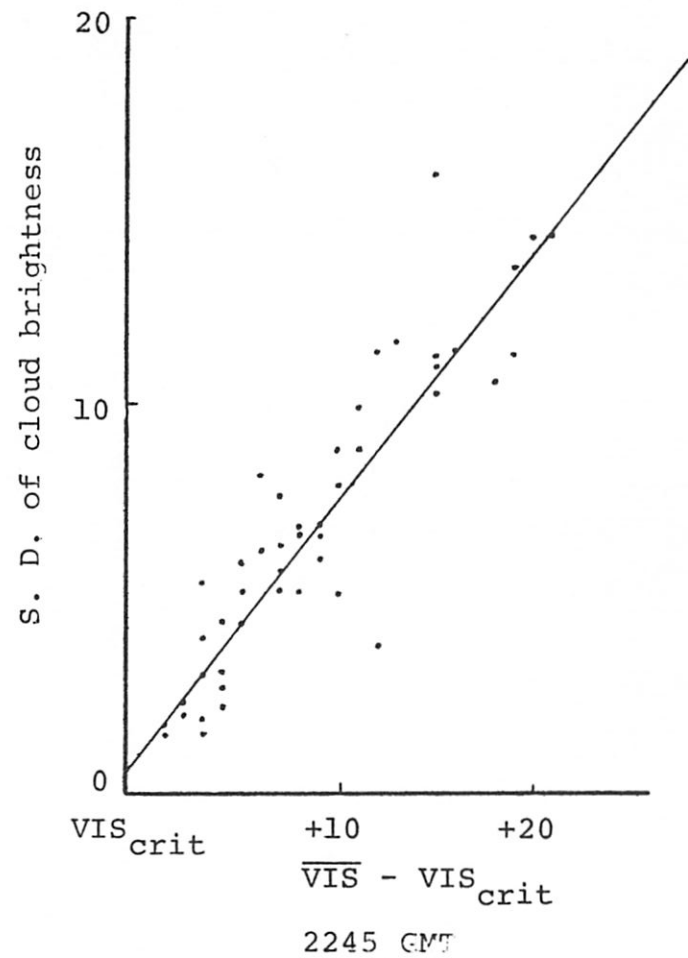
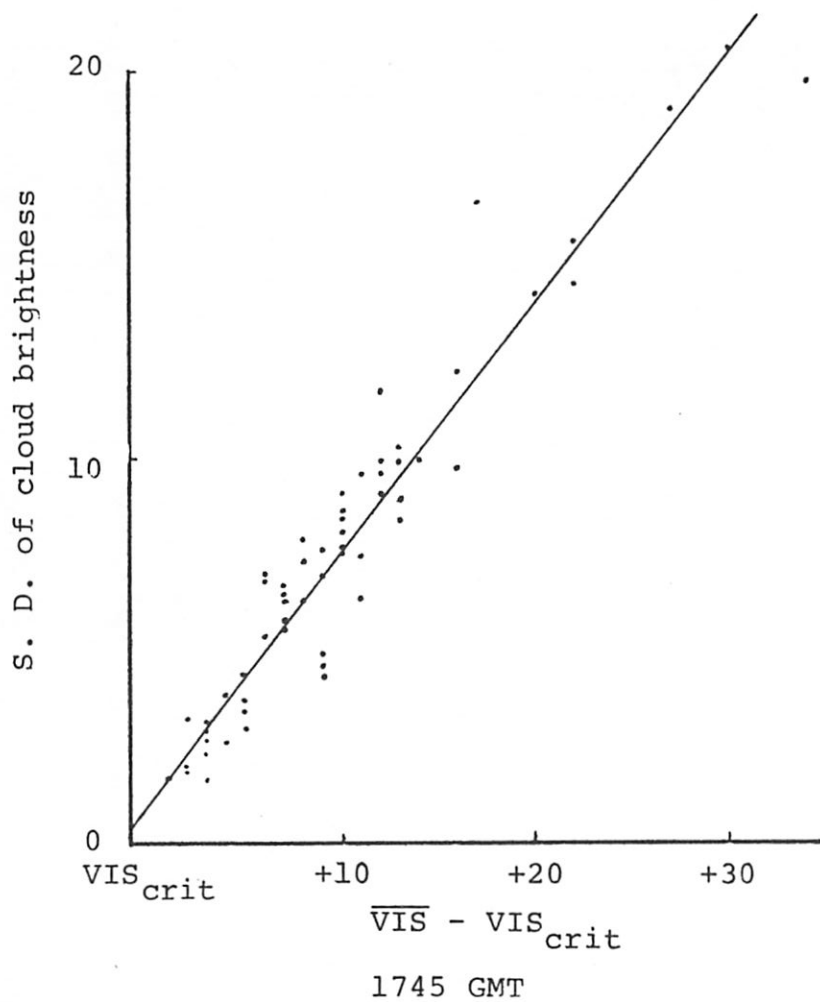


Figure 3-8 The comparison of standard deviation of cloud brightness and cloud mean brightness above its corresponding critical value at 1745 and 2245 GMT on 22 June 1976.

The coefficients of variation were compared with their mean brightness values. The coefficient of variation ( $V$ ) is defined as  $V = 100s/\bar{x}$  where  $\bar{x}$  is the mean and  $s$  the standard deviation of the sample. The magnitude of  $V$  gives a normalized measure of the width of a distribution relative to its mean value. Because visible brightness values are interpreted relative to the  $VIS_{crit}$  value in this study, this difference will be used for the mean value ( $\bar{x}$ ) to compute the coefficient of variation. Figure 3-9 shows these comparisons at 1745 and 2245 GMT. The regression line shown in these diagrams also yields that for a cloud with low mean brightness value, less than 3 units above  $VIS_{crit}$  value, the standard deviation of visible brightness is larger than the mean brightness value. The coefficient of variation then decreases as the mean brightness increases to a value of 15 units above  $VIS_{crit}$ ; after that point the ratio of standard deviation of brightness to its mean brightness remains almost constant. From Figure 3-9 we obtain an indication of the variation in scatter of the brightness values with mean cloud brightness.

From the discussion in this section, it can be concluded that the mean brightness of an individual cloud and its size are not well correlated (Figure 3-6). There are a few large clouds with low mean brightness value, such as thin stratus clouds, and some small clouds with high mean brightness values, such as developing convective clouds. Because of the varying character of clouds, a widely varying relation-

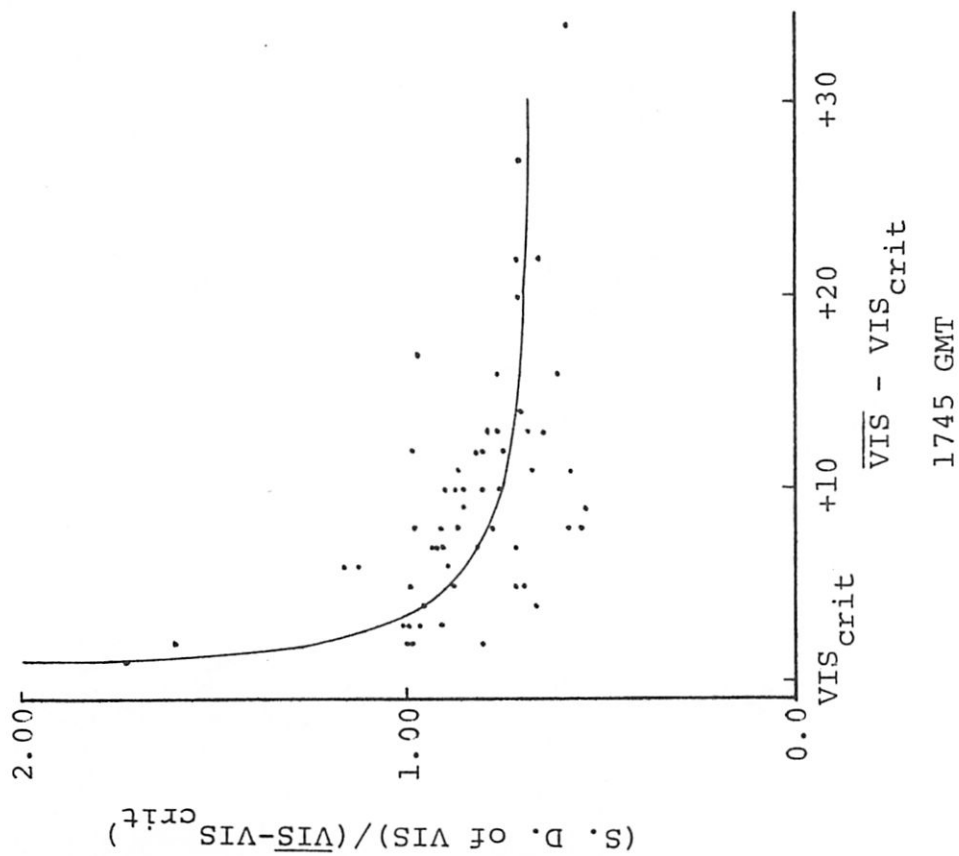
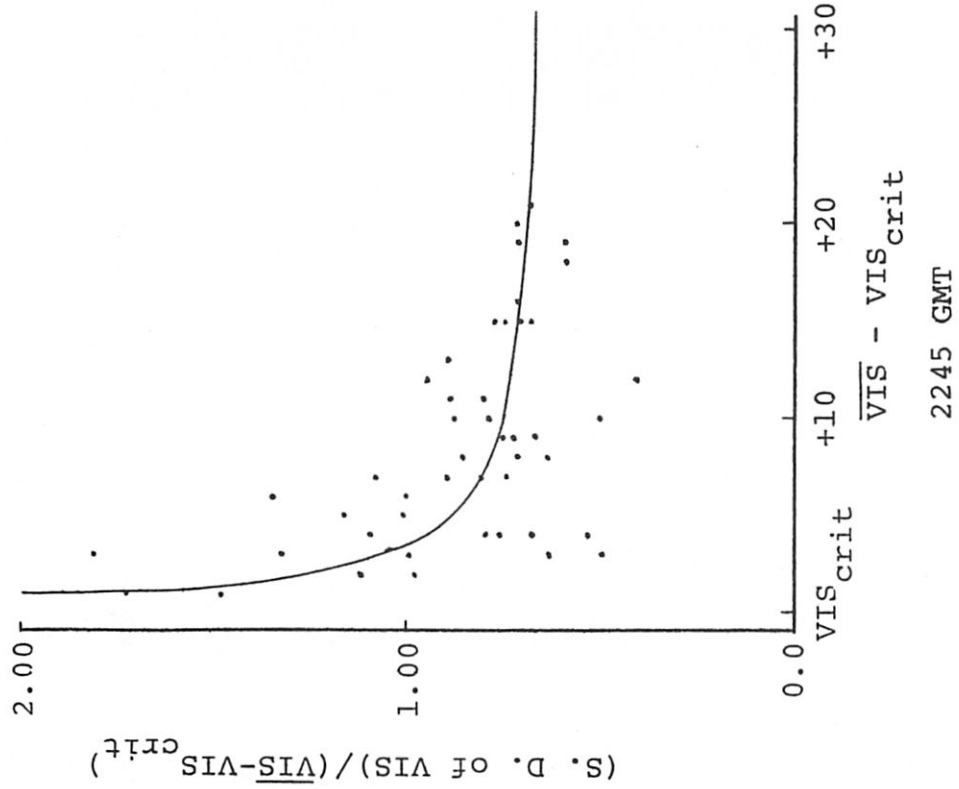


Figure 3-9 The comparison between the ratio of standard deviation of visible brightness (S.D. OF VIS) to the difference of mean brightness (VIS) and critical visible value (VIS<sub>crit</sub>) and the difference of VIS and VIS<sub>crit</sub> at 1745 and 2245 GMT on 22 June 1976.

ship between individual mean brightness of cloud and size can be expected. The same situation occurs regarding the correlation between standard deviation of brightness and cloud size (Figure 3-7). In some cases, the small isolated developing convective clouds have high standard deviations of brightness. In addition, some large clouds with low mean brightness value were found to be composed primarily of VIS radiance values close to the  $VIS_{crit}$  value. As a result, the standard deviation of brightness will be expected to be lower for such uniform clouds.

In addition, the standard deviation of brightness of clouds was correlated with the difference between the cloud mean brightness and its critical VIS value (Table 3-7). High correlation coefficients were obtained, showing that clouds with high mean brightness values will be associated with a high value of standard deviation of brightness. Thus, clouds with high mean brightness values are composed of a wide range of individual brightness values, an indication of a non-uniform appearance of the cloud top.

### 3.2 Cloud Albedo Determination

Albedo is the ratio of the radiation reflected by a surface to that incident upon it. Albedo is normally expressed as a fraction, ranging from 0 for a perfect absorber to 1 for a perfect reflector. A variety of satellite measurements of albedo have been reviewed. Different values of albedo have been obtained by using different

satellites as well as by different investigators using the same satellite data (Gruber, 1973). Typical albedo values for various surfaces given in the Smithsonian Meteorological Tables (List, 1966) are: 0.03 to 0.10 for rivers and seas, 0.07 to 0.20 for ground, and 0.05 to 0.84 for clouds. In this study, a calibration computer program was obtained from CSU (Smith, 1977b) for the basic albedo value determination. A modified technique was utilized for determining albedo values throughout the study period.

The intensity of the reflected solar radiation depends on the albedo values as well as on the solar zenith angle ( $\theta_0$ ). The albedo value corresponding to a given VIS count at the time of zero solar zenith angle ( $\theta_0 = 0^\circ$ ) was given in Figure 2-7 in Section 2.2. In this study period, the smallest solar zenith angle ( $\theta_0 = 8.5^\circ$ ) occurred at 1845 GMT on June 22. Since the albedo value is inversely proportional to the  $\cos\theta_0$  at different times, a difference of only 1% existed between 1845 GMT and the time with zero solar zenith angle ( $\cos 0^\circ / \cos 8.5^\circ = 1.01$ ). Therefore, Figure 2-7 will be used to determine albedo values from VIS counts at standard time. That figure shows that the  $VIS_{crit}$  value of 120 at 1845 GMT corresponds to an albedo value of 0.2. The same type of cloud, a small isolated cumulus, was used to determine  $VIS_{crit}$  at all study times. All of these should have the same cloud properties, and their albedo value should not change with time. Therefore,

all critical visible cloud radiance counts will be assumed to correspond to an albedo value of 0.2 throughout the entire period.

Visible radiance count versus albedo value curves have been obtained based upon this assumption. In addition, the minimum and maximum VIS counts, 0 and 255, will correspond to the minimum and maximum albedo values of 0 and 1.0. Using these two fixed minimum and maximum points as well as the third variable VIS critical value point, the adjusted albedo curve was computed at each time, matching the form of the albedo curve for zero zenith angle. Two of these albedo curves at 0015 and 0115 GMT, corresponding to solar zenith angles of  $71.5^{\circ}$  and  $83.5^{\circ}$ , are given in Figure 3-10. All albedo values used in this study have been obtained by this technique.

The adjusted maximum and minimum albedo values of one single pixel in the entire region as well as the maximum mean albedo of a single cloud are shown in Figure 3-11. It shows that the maximum albedo value decreases roughly from 0.75 at 1745 GMT to 0.52 at 2345 GMT, and then increases to 0.61 at 0015 GMT and remains constant until 0115 GMT. The minimum albedo of a single pixel is nearly constant from 1745 to 0115 GMT in a small interval between 0.04 and 0.08. The curve of maximum mean albedo of a cloud decreases gradually from 0.37 at 1745 GMT to 0.25 at 0115 GMT. Late in the day, the solar zenith angle becomes larger, and this

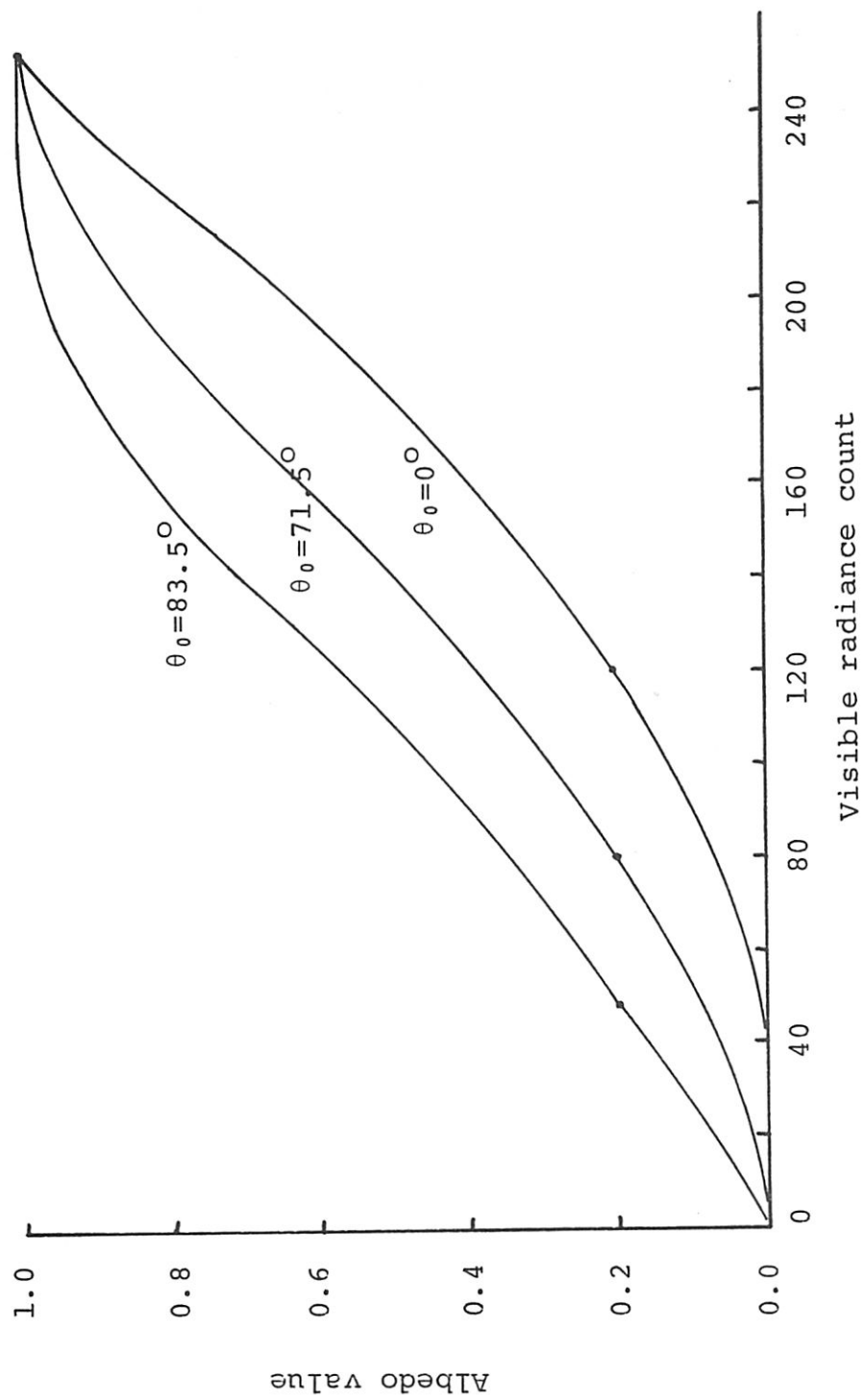


Figure 3-10 Albedo curves for solar zenith angles ( $\theta_0$ ) equal to  $0^\circ$ ,  $71.5^\circ$ , and  $83.5^\circ$ .

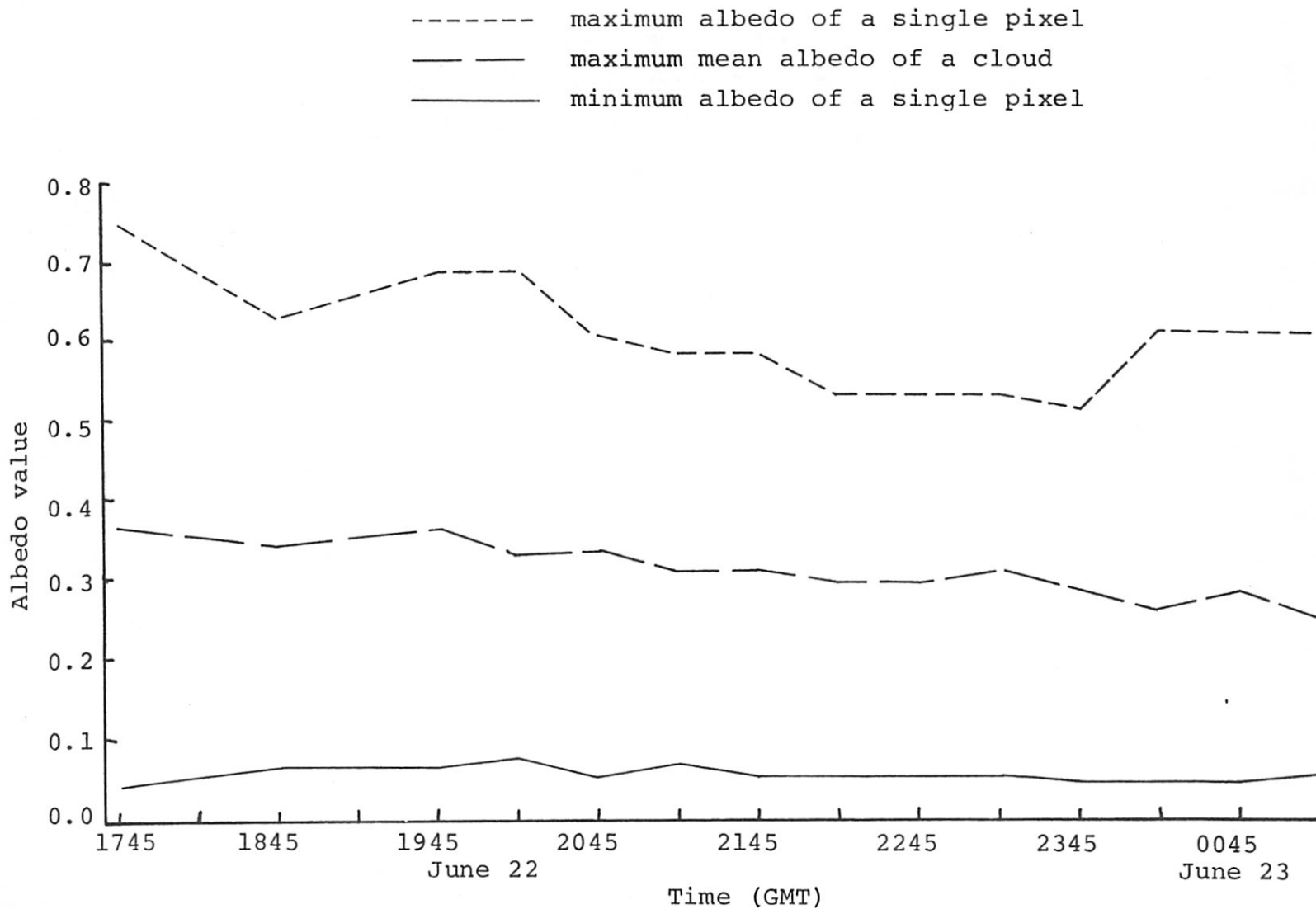


Figure 3-11 The maximum and minimum albedo of a single pixel as well as the maximum mean albedo of a cloud.

low sun angle causes greater shadowing effects in the non-uniform cloud top surface. The cloud shadows will reduce the overall brightness of the cloud and thereby yield a lower albedo value. The appearance of strong convective clouds in the study area late in the day was confirmed by radar observations; shadowing of adjacent lower cloud could be significant. At 0115 GMT, when the maximum solar zenith angle occurred, the strongest shadow effect could be noticed; at this time, a minimum mean cloud albedo value is observed in the Figure 3-11.

Throughout the day, the non-cloud minimum albedo of a single pixel did not vary with time. The fact that the darkest surface regions maintain constant albedo throughout the course of the day provides evidence that the albedo relationship with radiance values is varying in a reasonable manner as the solar zenith angle changes.

Because the cirrus clouds can be identified with regions of very cold temperature and low albedo values, the investigation of cloud albedo values will be of value in investigating the cirrus cloud distribution during the case study period.

### 3.3 Cloud Height and Cirrus Detection

Because the satellite infrared radiance data represent radiation emitted by the underlying atmosphere, cloud-top temperatures can be obtained through the utilization of the NESS standard calibration curve as discussed in Section 2.3

and given in Figure 2-8. Using the averaged sounding curve of Figure 2-13, cloud-top heights can then be determined. The cloud heights are analyzed and discussed for every half hour throughout the study period.

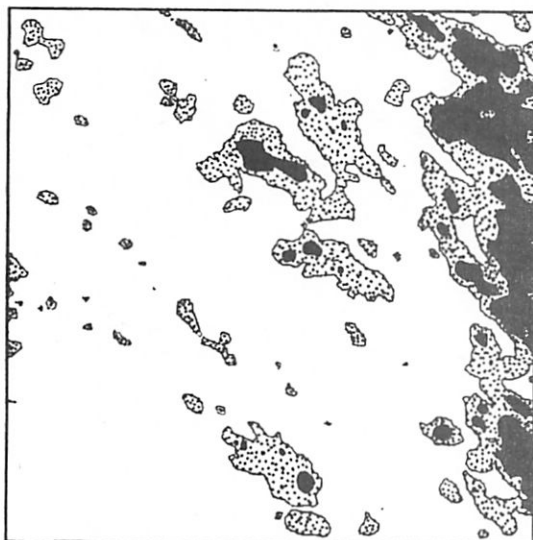
For the convenience of cloud height analysis, all IR data are transferred to temperature values according to the NESS standard calibration curve. Isotherms from 0C to -60C at 10C intervals are drawn for each 108x108 array IR radiance data set. From the averaged sounding for West Texas in this period, the corresponding heights for these specific temperatures are as follows:

Temperature (C)	0	-10	-20	-30
Corresponding (m)	4,800	6,200	7,800	9,100
Height (ft)	(15,500)	(20,500)	(25,500)	(30,000)

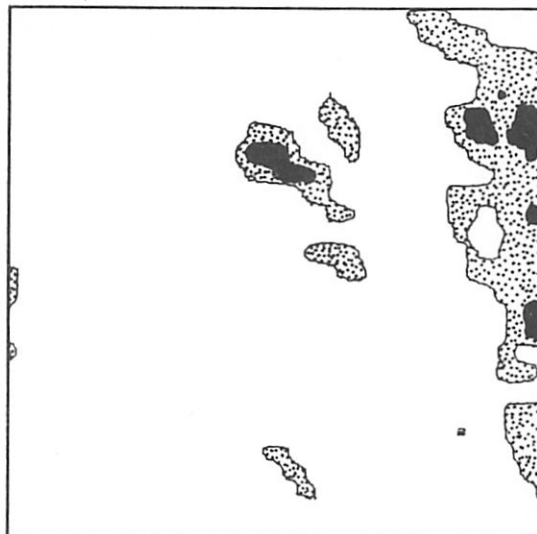
Temperature (C)	-40	-50	-60
Corresponding (m)	10,300	11,800	13,600
Height (ft)	(34,000)	(38,500)	(44,500)

The computer-generated plots of these isotherms throughout the study period are given in Figure 3-12. Each square in Figure 3-12 corresponds to the area of study defined in Figure 2-2. Figure 3-12 also shows a sequence of visible cloud contour plots for albedo values of 0.2, 0.4, 0.6 and 0.8 throughout whole period. They can be compared with infrared isothermal plots to determine cloud properties and heights.

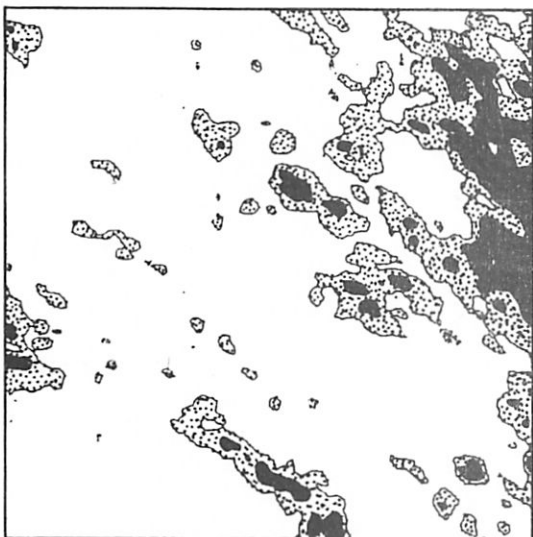
The number of regions with temperature lower than -10C is counted from the infrared radiance data. These numbers



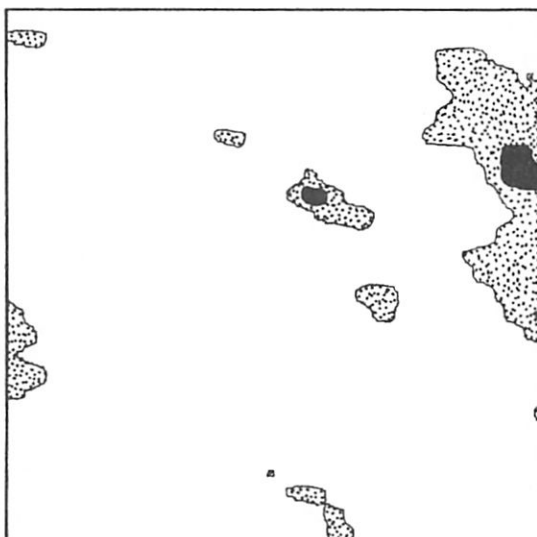
VIS 1745GMT



IR 1745GMT

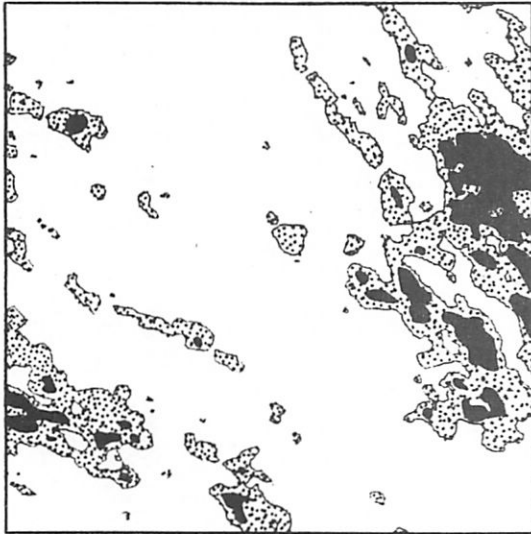


VIS 1815GMT

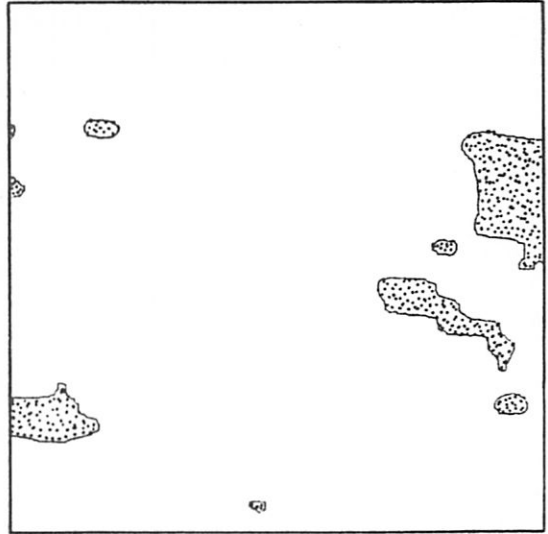


IR 1815GMT

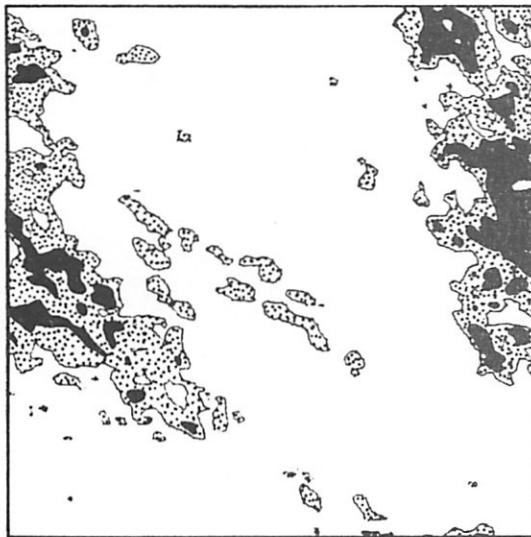
Figure 3-12 Computer-generated plots of visible and infrared radiance patterns from 1745 GMT 22 June to 0115 GMT 23 June, 1976. An explanation of the symbols used is given following the plots for 0115 GMT on 23 June 1976.



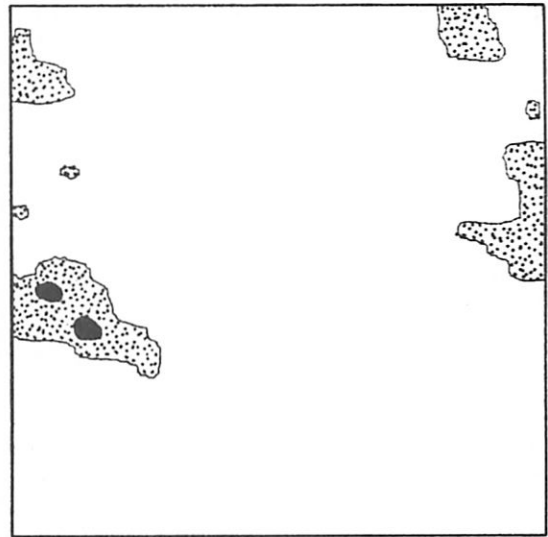
VIS 1845GMT



IR 1845GMT

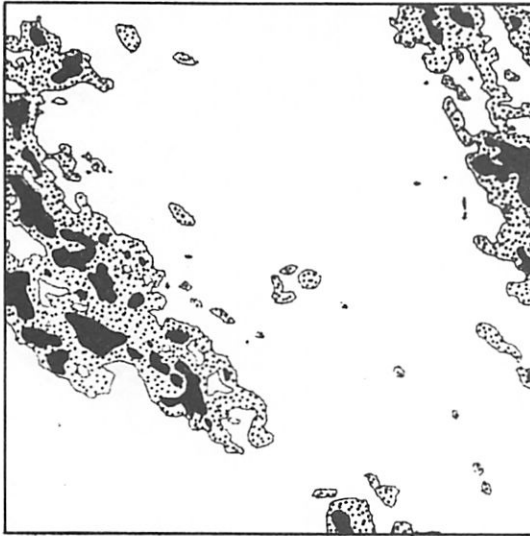


VIS 1945GMT

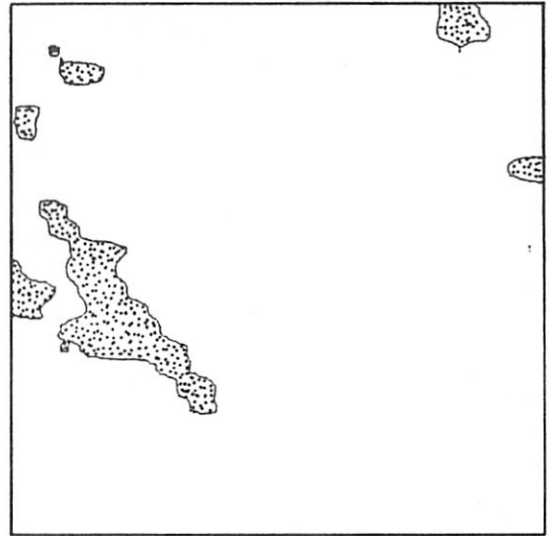


IR 1945GMT

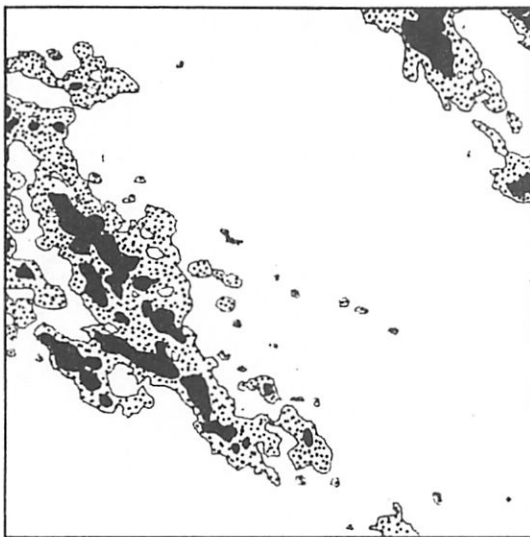
Figure 3-12 Continued.



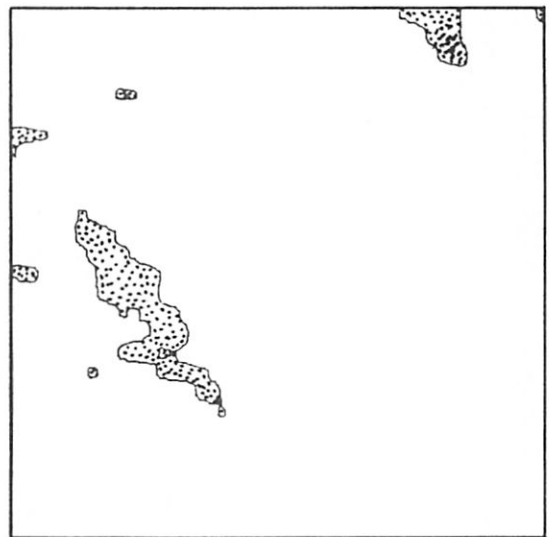
VIS 2015GMT



IR 2015GMT

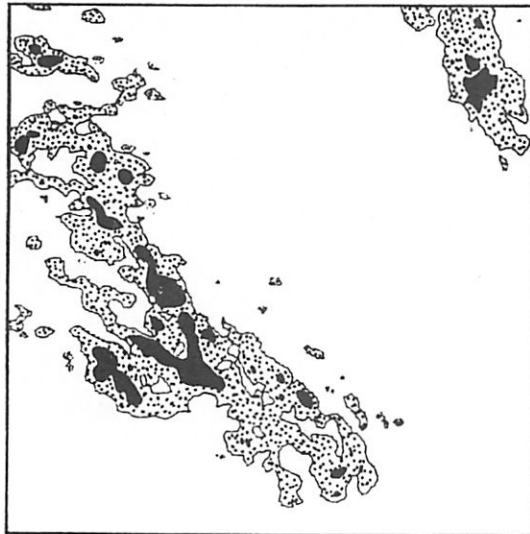


VIS 2045GMT

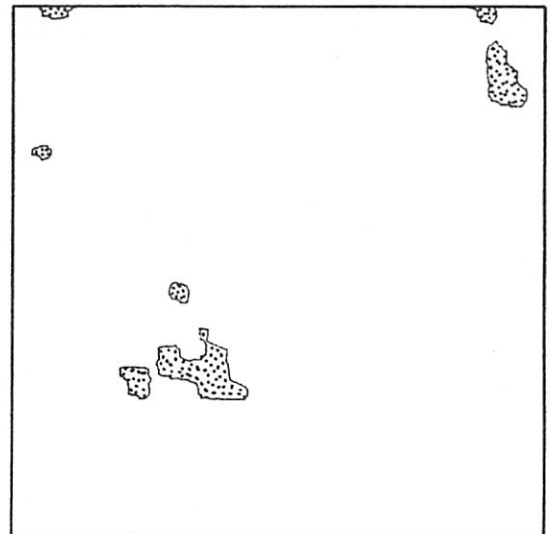


IR 2045GMT

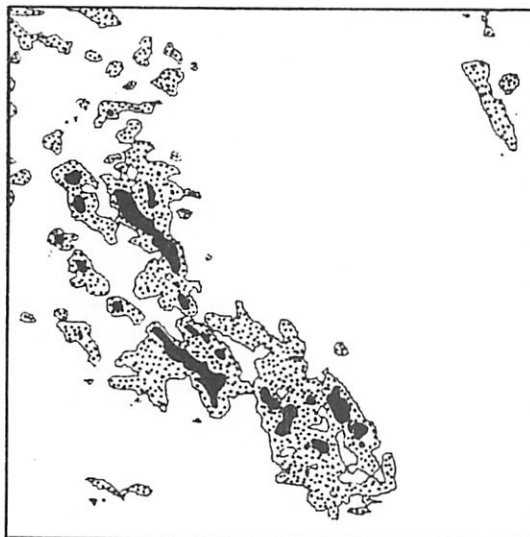
Figure 3-12 Continued.



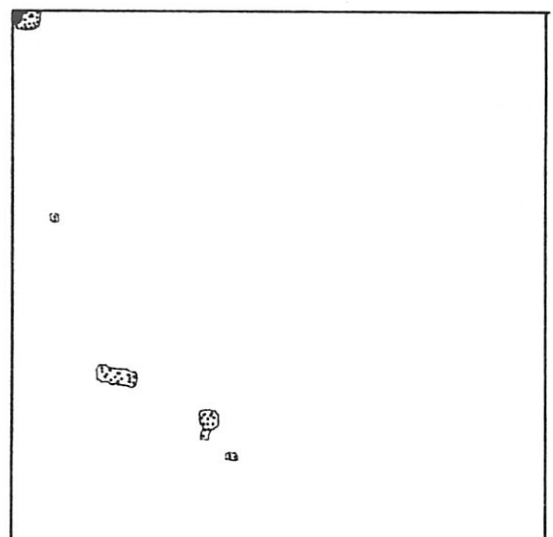
VIS 2115GMT



IR 2115GMT

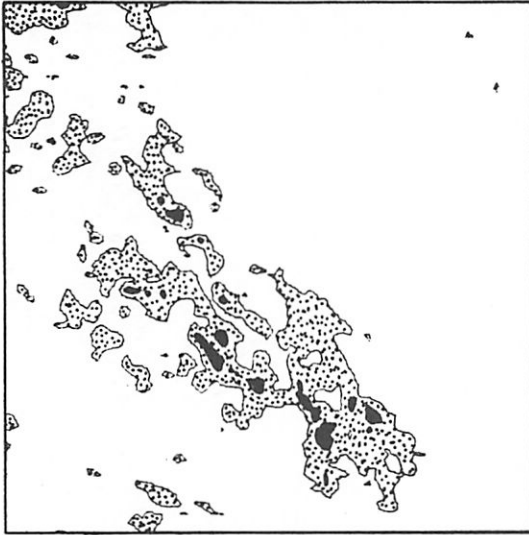


VIS 2145GMT

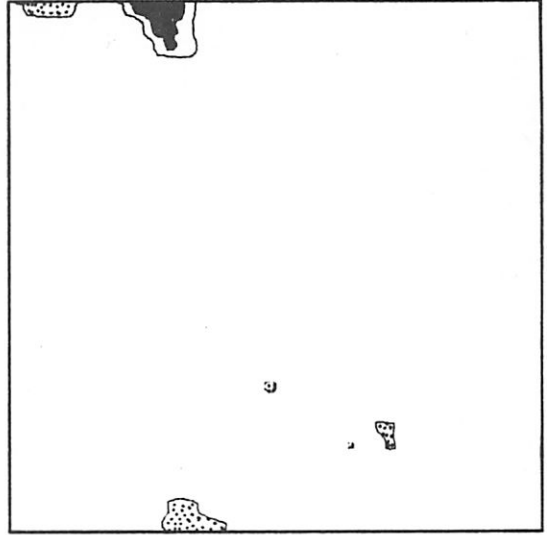


IR 2145GMT

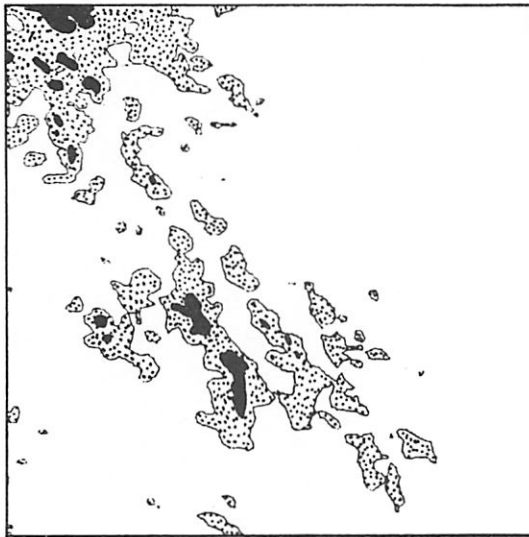
Figure 3-12 Continued.



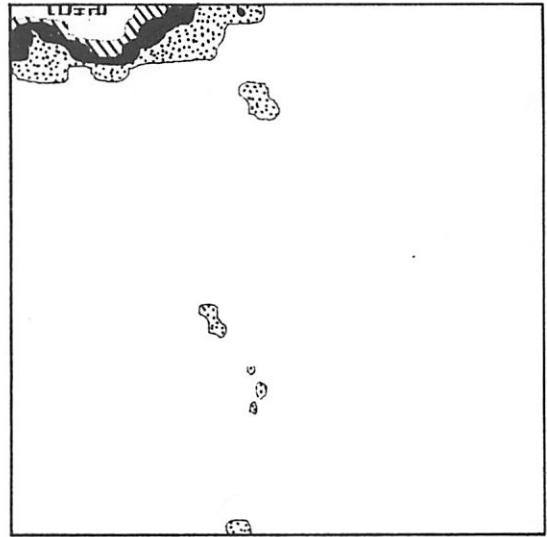
VIS 2215GMT



IR 2215GMT

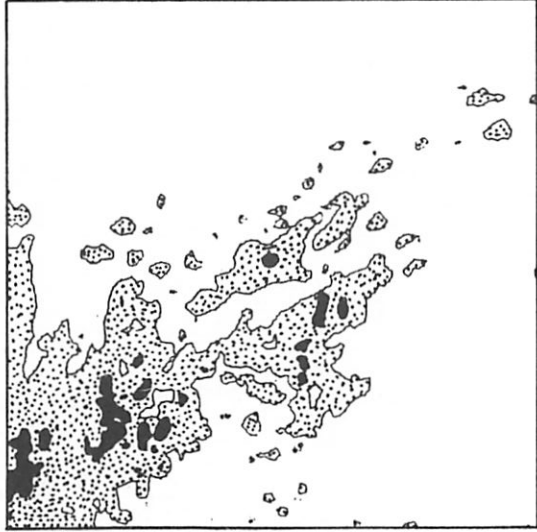


VIS 2245GMT

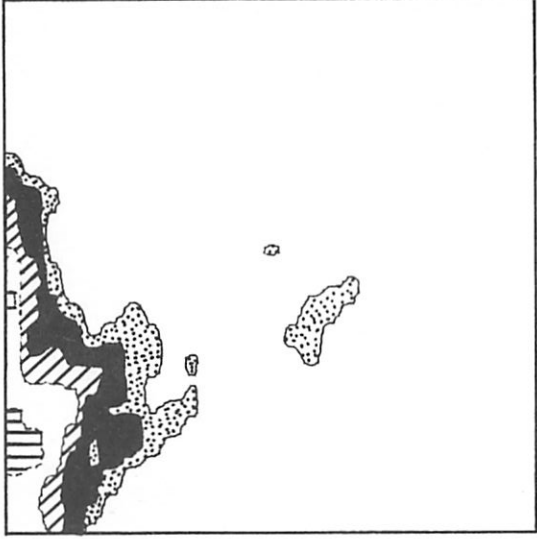


IR 2245GMT

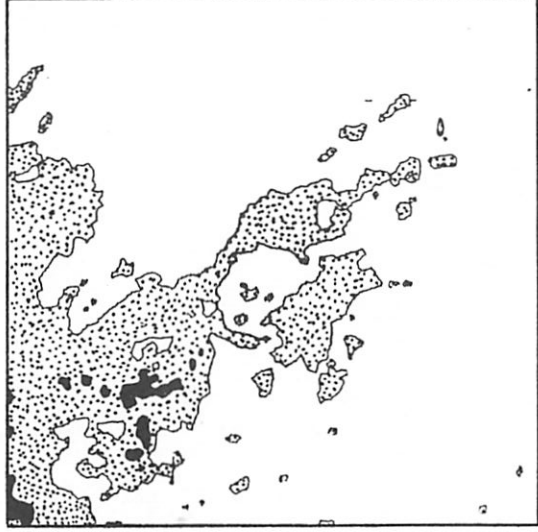
Figure 3-12 Continued.



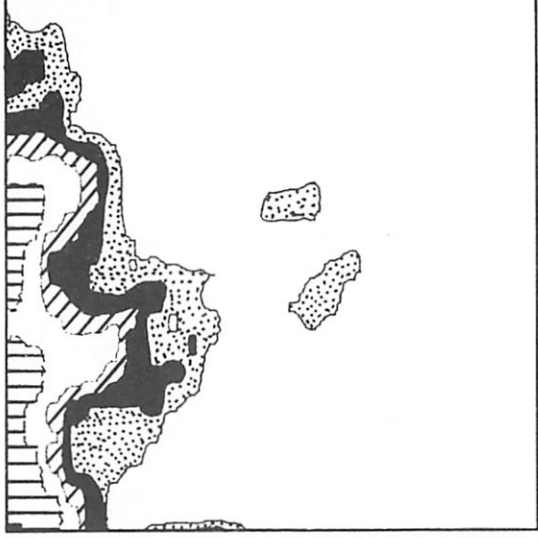
VIS 2315GMT



IR 2315GMT



VIS 2345GMT

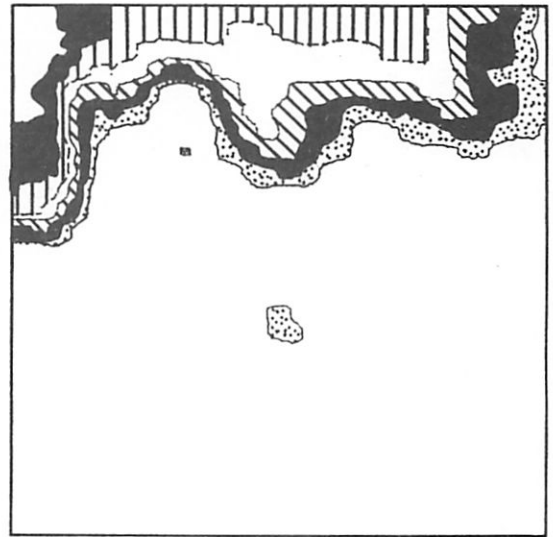


IR 2345GMT

Figure 3-12 Continued.



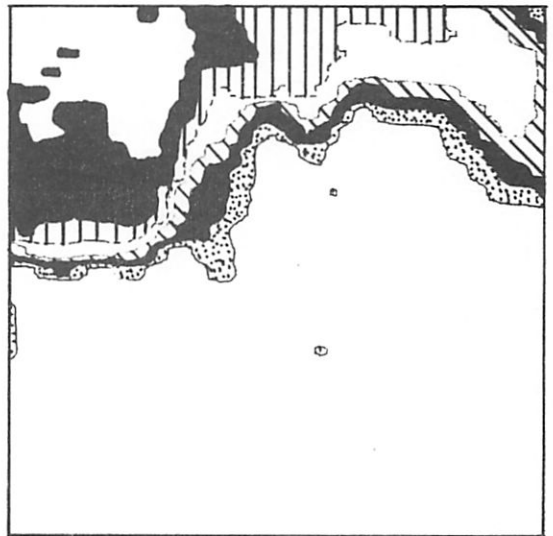
VIS 0015GMT



IR 0015GMT

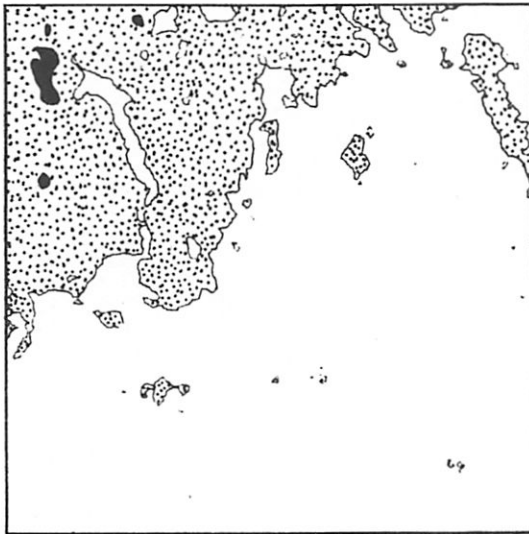


VIS 0045GMT

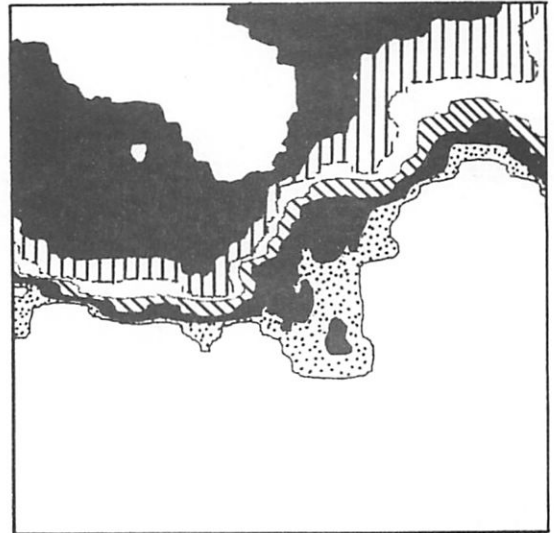


IR 0045GMT

Figure 3-12 Continued.



VIS 0115GMT



IR 0115GMT

VIS scale

Albedo

0.0 to 0.2	
0.2 to 0.4	
0.4 to 0.6	
0.6 to 0.8	

IR scale

Temperature (C)

$T > 0$	
$0 \geq T > -10$	
$-10 \geq T > -20$	
$-20 \geq T > -30$	
$-30 \geq T > -40$	
$-40 \geq T > -50$	
$-50 \geq T > -60$	
$-60 \geq T$	

Figure 3-12 Continued.

are much smaller compared to the number of clouds obtained from the visible radiance data in Section 3.1.1. The reason for this difference is the poor resolution of original IR radiance data, 5.84x11.68 km. The viewing region of a single IR pixel is equivalent to a 4x8 array of VIS pixels, as discussed in Section 2.4. As a result, many small clouds are lumped together and appear as a single cloud element in the IR data set. Despite the poor resolution of the IR data, they still provide good information concerning the temperature and height of the cloud top.

The minimum temperature observed in the temperature plots for the different times can be used to show the highest cloud top in the entire data set at the time. The maximum temperature, corresponding to the minimum IR count, can represent the surface temperature for the data set. Both the maximum and minimum temperatures and the corresponding height of the maximum cloud top, all derived from the satellite radiance data, are shown in Table 3-8 throughout the study period. The satellite-derived minimum temperature at 1745 GMT coincided with an extensive thunderstorm entering the study area (Figure 3-12). The thunderstorm rapidly moved southward from Lubbock into the study area. Meanwhile, the visible low clouds located in the west central portion of the area gradually dissipated. Later, at 2245 GMT, another thunderstorm complex entered the study area. By 0045 GMT, this thunderstorm dominated most of the cloud cover region with a maximum satellite-derived cloud top height of 15,100 m (49,500 ft). The last column of Table 3-8 shows the maximum

Table 3-8 Satellite-derived values of maximum and minimum temperature and maximum cloud top height in the study area. Also given are observed maximum radar echo heights.

TIME (GMT)	Max. temp. (°C)	Min. temp. (°C)	Max. cloud top (m)	Max. cloud top (ft)	Radar echo top (ft)
June 22					
1745	37	-17	7,300	24,000	22,000
1815	36	-16	7,100	23,500	
1845	39	-10	6,200	20,500	19,000
1945	40	-13	6,700	22,000	15,000
2015	40	- 9	6,100	20,000	
2045	39	- 6	5,700	18,500	*
2115	39	-10	6,200	20,500	
2145	37	-16	7,100	23,500	*
2215	36	-18	7,400	24,500	
2245	34	-40	10,300	34,000	35,000
2315	34	-42	10,700	35,000	
2345	32	-51	12,000	39,500	42,000
June 23					
0015	32	-70	15,100	49,500	
0045	30	-70	15,100	49,500	46,000
0115	28	-68	14,700	48,000	

\* no echo height was reported within the study region.

height of the radar precipitation echo obtained from NWS radar summary charts (Figure 2-5). Although no precipitation is reported in the study area at 2035 GMT and 2135 GMT, the other echo heights agree well with the satellite measurements. Since the satellite measurements are for the cloud top and radar detected the echo of the precipitation region, it is reasonable that satellite cloud top heights will be higher than the radar echo tops. Considering the variability of results reported in comparisons of satellite-derived cloud top heights and observed radar echo tops (Adler and Fenn, 1977; Waters et al., 1977), the agreement found in this study is quite satisfactory.

Table 3-9 shows the percentage of the cloud covered area with cloud top temperatures in different intervals. At 1745 GMT, for 1.4% of the study area the cloud height is over 6,200 m (20,500 ft), and for 10.9% of the area cloud heights occur between 4,800 m (15,500 ft) and 6,200 m. From Figure 3-12 it is seen that the coldest region was located between Big Spring and Post with a cloud top height of 7,300 m (23,500 ft). The other cold regions are located along the east boundary of study area with the cloud tops near 6,700 m (22,000 ft). From the cloud contour diagrams, one can follow the low temperature regions as they moved southwestward until 1815 GMT when there were only two low temperature regions with temperatures lower than -10C, corresponding to a height of 6,200 m. At 1945 GMT, two new

Table 3-9 Percentage of study area having radiance temperatures (T) in various intervals (C). Corresponding heights (h) are given in meters.

Time (GMT)	T $\geq$ 10 h $\leq$ 3700	10>T $\geq$ 0 3700<h $\leq$ 4800	0>T $\geq$ -10 4800<h $\leq$ 6200	-10>T $\geq$ -20 6200<h $\leq$ 7800	-20>T $\geq$ -30 7800<h $\leq$ 9100	-30>T $\geq$ -50 9100<h $\leq$ 11800	-50>T $\geq$ -70 11800<h $\leq$ 15100	-70>T 15100<h
June 22								
1745	72.3	15.4	10.9	1.4	0	0	0	0
1815	74.5	16.2	8.8	0.5	0	0	0	0
1845	77.5	16.6	5.9	0	0	0	0	0
1945	80.7	11.5	7.6	0.2	0	0	0	0
2015	82.5	11.8	5.7	0	0	0	0	0
2045	85.0	11.0	4.0	0	0	0	0	0
2115	85.5	12.3	2.2	0	0	0	0	0
2145	92.0	7.4	0.6	0	0	0	0	0
2215	91.0	6.8	1.6	0.6	0	0	0	0
2245	86.6	7.3	3.1	1.1	0.7	1.2	0	0
2315	77.0	8.6	4.6	3.7	2.4	3.7	0	0
2345	67.8	7.4	9.0	4.6	3.4	7.8	0	0
June 23								
0015	62.0	9.5	4.9	3.9	4.4	11.5	3.8	0
0045	53.8	8.5	4.1	2.9	3.9	12.5	14.2	0
0115	42.4	4.6	5.6	3.9	3.2	12.8	27.4	0

cold areas with heights over 6,200 m appeared to the west of Midland; however, they dissipated by 2015 GMT. After 2145 GMT, a large cloud region with very low cloud top temperatures began to enter the study region from the northwest. This one cloud area dominated the record of the lowest cloud top temperature after 2145 GMT. Referring to Table 3-9, it is seen that this is the only region with a temperature lower than  $-20^{\circ}\text{C}$  throughout the period. At 0115 GMT, 43% of the study area is enclosed by the  $-20^{\circ}\text{C}$  isotherm which was within one large low temperature region reaching to an altitude of 14,700 m (48,000 ft). The height of this layer is close to the tropopause height of 15,000 m (49,000 ft).

In previous satellite cloud studies, cirrus have been a special problem for the determination of cloud amount, height, and movement (Reynolds and Vonder Haar, 1977). The development, dissipation and movement of cirrus will be discussed, based on the assumption that cirrus have a cloud temperature below  $-20^{\circ}\text{C}$  and an albedo value less than 0.2. At the same time, there may be some deep vertically developed clouds with temperatures lower than  $-20^{\circ}\text{C}$ , but with an albedo larger than 0.2. The satellite-derived percentages of such deep vertical clouds and cirrus clouds are shown in Figure 3-13, which shows essentially no high clouds in the study area before 2215 GMT. After 2215 GMT, deep vertical clouds were observed and began to increase rapidly as a thunderstorm moved into the area from the northwest (Figure 3-12). After

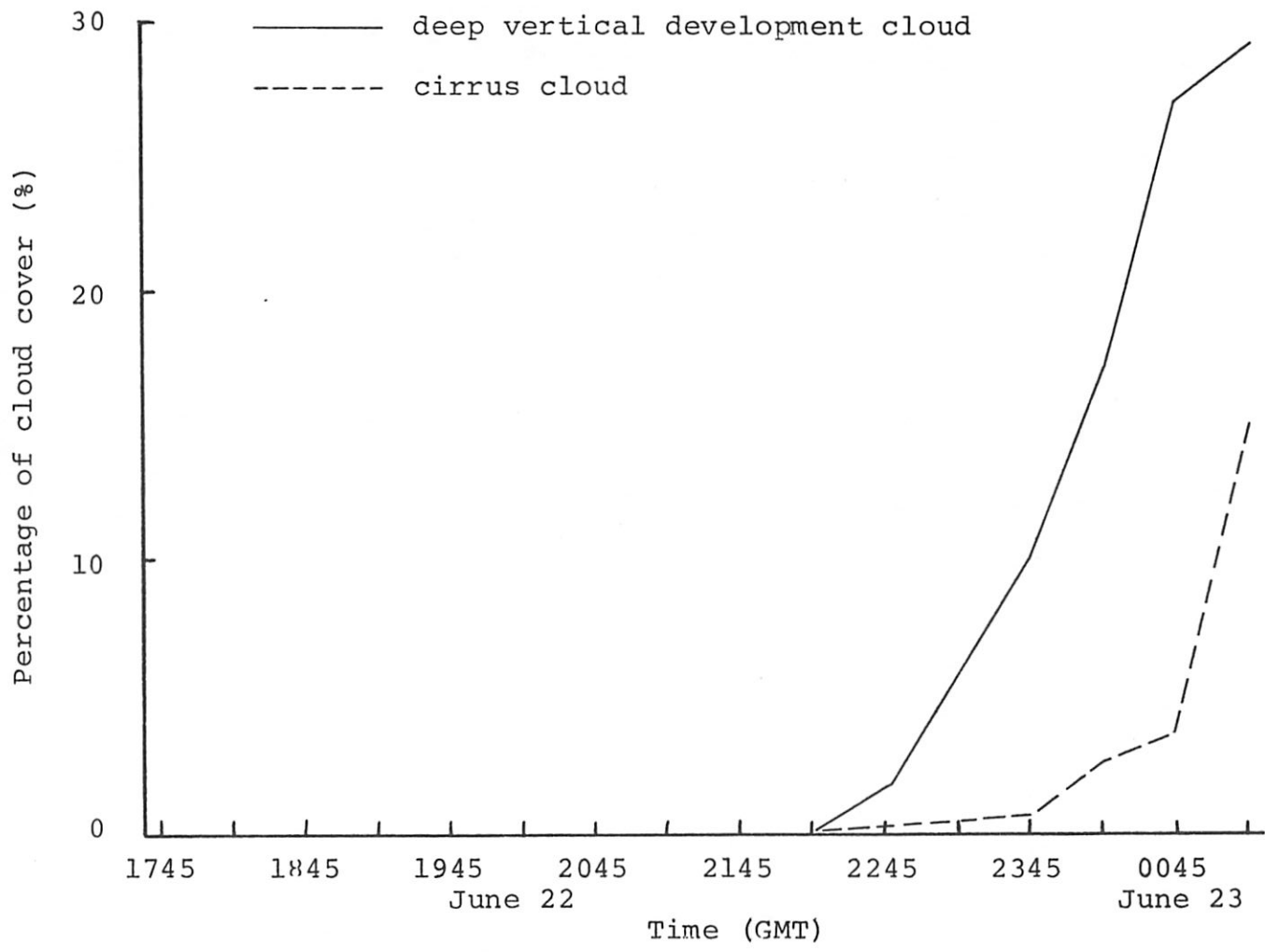


Figure 3-13 Percentages of cirrus and deep vertical development clouds observed within the study area.

2215 GMT, cirrus appeared and the two curves in Figure 3-13 increased until 0115 GMT, reaching maximum values of 15% cirrus and 29% deep vertical cloud cover over the study area.

Cloud observations by ground observers do not agree with the satellite-derived results. Hourly observations in the study area were taken at Abilene, Big Spring, Lubbock, Midland and San Angelo from 1700 GMT 22 June 1976 to 0300 GMT 23 June 1976. Clouds at 25,000 ft (7.6 km) were reported every hour at Abilene, Big Spring and Midland, every hour except 2300 and 0000 GMT at Lubbock, and every hour except 2200, 2300 and 0000 GMT at San Angelo. The temperature at 25,000 ft was approximately -17C (Figure 2-13), and the -20C temperature selected to discriminate high clouds occurred at 25,500 ft (7.8 km). The cirrus detection criterion of cloud top temperature below -20C and albedo less than 0.2 was clearly inadequate. It appears from the ground observations that the cirrus clouds detected late in the afternoon were thick anvils associated with approaching thunderstorms. Thin cirrus present earlier in the day went undetected. Efforts are continuing to overcome this problem.

#### 3.4 Satellite-tracked Cloud Movement

Cloud movement is estimated in this study through analysis of the satellite radiance data, and is compared with information obtained from satellite imagery and radar summaries as well as wind velocity obtained from rawinsonde data. The

estimation of cloud movement from photographic imagery is difficult, because of the need to match geographical features as well as cloud patterns solely by visual means. Cloud motions derived from radiance data benefit from accurate geographical locations based upon best-fit computations using several known landmarks and the capability to electronically overlay successive cloud patterns. Another difficulty common to both satellite-derived estimates and the radar summary values is that only a single motion vector was obtained to represent the total study area. Consequently, the values obtained cannot be expected to represent the movement of each cloud in the study area. When comparing results, it also should be remembered that the four observations are not made at the same time: the satellite imagery is given at hourly intervals starting at 1800 GMT, the radiance data are at intervals of one half hour beginning at 1745 GMT, the radar summaries occur at hourly intervals beginning at 1735 GMT, and the soundings occur at three hour intervals beginning at 1800 GMT.

The sounding data, obtained from Big Spring, Midland, Post, and Robert Lee, were used to construct a vertical wind profile. A high relative humidity layer in the atmosphere as observed by a rawinsonde is an area likely to support the formation of clouds. Cloud motion and the movement of the ambient air can deviate significantly from each other in some instances. However, evidence exists

that satellite-derived cloud motions and the corresponding rawinsonde winds generally agree within 6 to 7 m sec<sup>-1</sup> for speed and 40° for direction (Bauer, 1976; Hubert and Whitney, 1971). Therefore, the rawinsonde wind velocities to be compared with satellite-derived cloud motions were obtained from the layer with high relative humidity. This layer was located between 500 and 400 mb, the corresponding temperature is from -7 to -18C, and height is from 5,800 to 7,500 m (19,000 to 24,000 ft). In comparing wind velocity derived from the four individual stations with the averaged vector at the same time, most deviations of wind direction were found to be less than 15°. The individual deviation of wind speed was less than 1.5 m sec<sup>-1</sup>, or 5 km hr<sup>-1</sup>, from station to station. Therefore, an averaged wind velocity can be used to describe the wind field at the cloud layer.

The visible photographic images were available at one hour intervals from 1800 to 2200 GMT on 22 June 1976. Estimation of cloud motion from the images was accomplished by comparing locations of clouds in consecutive images as reported in a previous study (Jurica, 1977). The NWS also provides the movement of radar echoes at hourly intervals. In this study period, all movement was associated with individual radar echoes; no line or area echo movement is indicated on the radar summary charts.

The satellite radiance data were used to track and determine the cloud movement. Changes in cloud locations

were estimated by comparing two consecutive cloud plots. VIS and IR plots were used together to obtain the cloud movements. Two successive cloud pattern diagrams were overlaid to obtain the best match of cloud locations and low temperature regions. The cloud movement could then be determined by measuring the shift of the diagrams with time. The derived track of representative cloud movement for the area is given in Table 3-10 to show the direction and speed of movement at 30 min intervals.

Table 3-10 also shows the comparison of velocities obtained from satellite radiance data, photographic images, radar summary charts and rawinsonde data. The precision of measurement of direction of motion is estimated  $\pm 20^{\circ}$  for the imagery,  $\pm 10^{\circ}$  for radar summary charts, and  $\pm 5^{\circ}$  for satellite radiance data and sounding data studies. The precision of measurement of speed of motion is estimated  $\pm 15$  km/hr for the imagery,  $\pm 10$  km/hr for the radar summary charts, and  $\pm 5$  km/hr for satellite radiance data and sounding data. The direction of cloud movement obtained from the several data sources agree quite well. The largest deviation in direction occurred at 1845 GMT between the satellite data and the radar summary chart. Because of the loss of satellite radiance data at 1915 GMT, the radiance estimates of cloud motion at 1845 and 1945 GMT are not reliable. Generally, the speed obtained from satellite radiance data is the largest among the four. The radar echo speed is pretty close to the speed estimated from



satellite data, despite the fact that radar echoes indicate the movement of individual precipitation areas within clouds. The estimated cloud speeds obtained from the imagery did not agree well with those from the radiance data, especially from 1800 to 2000 GMT. The poor reliability of imagery speed estimations, caused by the very subjective nature in which they were obtained, may explain this deviation.

One factor which influences the reliability of satellite-derived cloud motions is the change with time which occurs in the cloud pattern. This was frequently observed, and can be associated with at least two processes. Development or dissipation of clouds between successive data sets will alter the cloud shapes. In addition, clouds at different levels can move at different velocities. This is particularly true regarding the motion of high-level cirrus clouds. After 2115 GMT the appearance of cirrus becomes a real factor in the estimation of cloud movement. In order to reduce this problem as much as possible, only those clouds with stable size and rather high albedo, and therefore relatively easy to track, were used to obtain the cloud velocity. Low level stratus or clouds with extremely variable size caused by rapid growth or dissipation were not used in the motion estimates because of the difficulty involved in tracking. In order to investigate such highly variable clouds, consecutive satellite radiance data at short-time intervals will be needed.

In this study, a single estimate was made to represent approximate cloud movement in the study region. The comparison of directions and speeds obtained from four data sources was given in Table 3-10. In view of the approximate nature of the measurements, the agreement is good. As mentioned before, on this particular case there was a general uniformity of air movement that does permit the comparison of the measurements from the different techniques. Under different conditions, the comparison of results could be less favorable, for example with a multi-level cloud system having movement in different directions at various levels.

Short-time interval, or rapid-scan, satellite radiance data should provide more precise movement, development, and dissipation information. In addition, the planned development of a technique to objectively match, in a statistical manner, the distribution of computer-derived brightness centers is expected to produce significantly more reliable cloud motion estimates in the near future.

## CHAPTER IV

### SUMMARY AND CONCLUSION

This report has presented an analysis technique based upon Geostationary Operational Environmental Satellite (GOES) radiance data and developed for the determination of cloud parameters. Fifteen sets of simultaneous satellite visible and infrared radiance data on 22 June 1976 were selected as a case study. Of principal interest is the cloud characteristics study which includes the analysis of cloud amount, brightness, albedo, and height as well as cirrus and cloud movement determination.

Comparing the radiance data and photographic imagery, a minimum cloud size of eight radiance data points, with an equivalent circular cloud diameter of 4.6 km, was found to match the smallest isolated cloud recognizable from the imagery. Under this constraint, a close agreement exists early in the afternoon between the number of clouds and percent cloud cover derived from the two forms of satellite data. Later in the day, imagery- and radiance-derived cloud numbers differ somewhat, apparently as a result of decreasing irradiance with increasing solar zenith angle. At the same time, the frequency distribution of brightness values narrows. As a result, it becomes more difficult to distinguish cloud from underlying non-cloud background late in the day. Through adjustment of the cloud/non-cloud threshold value, it was possible to overcome the solar

zenith angle problem in the radiance study. Therefore, the cloud counts derived from the radiance data are considered to be more reliable than those from the imagery.

Analyzing the cloud properties, it was found that the mean brightness, or albedo, of a cloud and its size are not highly correlated. This is to be expected considering the range of properties associated with various cloud types, from small isolated clouds with strong vertical development and high albedo values to large widespread stratus clouds with low albedo. An albedo versus visible radiance relationship obtained by calibration of the sensor at high sun conditions was used as a standard curve. Albedo curves for all other solar zenith angles were constructed based upon an albedo value of 0.2 for the cloud/non-cloud critical radiance value and albedo values of 0 and 1 for the minimum and maximum radiance values of 0 and 255, respectively.

Cloud height was determined through the joint use of infrared data and sounding data, and the results compared with radar summary charts. In general, the highest cloud tops obtained from infrared radiance data exceeded those derived from the radar echoes. Because the radar echo represents precipitation, it is reasonable to find the top of the radar echo lower than the top of the cloud.

Cirrus clouds were identified as regions where low cloud temperatures were associated with low albedo values. The detection of cirrus in this manner using satellite radiance data did not agree with ground observer reports. Further

research is required to establish a reliable technique for the detection of thin cirrus from satellite data.

Cloud movement was obtained by tracking the cloud pattern through successive data sets. Comparing the cloud movements obtained from several data sources -- satellite imagery, satellite radiance data, radar summary charts and rawinsonde data -- the radiance data can provide better information than the others. This is the case for two reasons: (1) greater spatial resolution permits more accurate location of individual cloud features, and (2) the high resolution of visible and infrared radiance values allows small changes in the clouds to be detected. In addition, if the time interval between satellite radiance data sets were reduced from 30 min to a shorter interval, there would be an excellent opportunity to study changes in cloud structure caused by interaction with the environment or surrounding clouds.

The work described here is an initial case study of cloud properties in the High Plains of Texas. The primary objective has been the development of techniques to determine convective cloud features using bispectral radiance data from geostationary satellites. The ability to detect such clouds, to count their number as a function of size, and to estimate their maximum vertical extent has been demonstrated. However, efforts to detect cirrus clouds and to reliably track cloud movement in an objective manner have not met with success. With additional effort, it is expected that these

techniques will be developed. As a result, the use of satellites in support of atmospheric water resource management in the High Plains will be enhanced.

## LIST OF REFERENCES

- Adler, R. F., and D. D. Fenn, 1977: Satellite-Based Satellite Intensity Parameters. Preprints of Tenth Conference on Severe Local Storms, Omaha, Nebraska, American Meteorological Society, 8-15.
- Bauer, K. G., 1976: A Comparison of Cloud Motion Winds with Coinciding Radiosonde Wind. Mon. Wea. Rev., 104, 922-931.
- Bristor, C. F., 1975: Central Processing and Analysis of Geostationary Satellite Data. NOAA Technical Memorandum NESS 64, U.S. Dept. of Commerce, Washington, D.C., 155 pp.
- Booth, A. L., and V. R. Taylor, 1969: Meso-scale Archive and Computer Products of Digitized Video Data from ESSA Satellite. Bull. Amer. Meteor. Soc., 50, 431-438.
- Dismachek, D. C., 1977: National Environmental Satellite Service Catalog of Products. NOAA Technical Memorandum NESS 88, U.S. Dept. of Commerce, Washington, D.C., 102 pp.
- Fleagle, R. G., and J. A. Businger, 1963: An Introduction to Atmospheric Physics. Academic Press. 346 pp.
- Gruber, A., 1973: Review of Satellite Measurements of Albedo and Outgoing Long-wave Radiation. NOAA Technical Memorandum NESS 48, U.S. Dept. of Commerce, Washington, D.C., 12 pp.
- Hubert, L. F., and L. F. Whitney, Jr., 1971: Wind Estimation from Geostationary-Satellite Pictures. Mon. Wea. Rev., 99, 665-672.
- Jurica, G. M., 1977: Cloud Characteristics in the Southern High Plains Derived from Satellite Imagery. Interim Report to the Texas Water Development Board. April, 31 pp.
- \_\_\_\_\_, 1978: Satellite Studies in the Texas HIPLEX Area. Interim Report to the Texas Department of Water Resources, April, 27 pp.
- List, R. J., 1966: Smithsonian Meteorological Tables. Sixth Revised Edition, Smithsonian Institution, 527 pp.
- Mosher, F. R., 1974: SMS Cloud Height. Space Science and Engineering Center, University of Wisconsin, 25 pp.

- NESS, 1976: Satellite Activities of NOAA 1975. NESS, U.S. Dept. of Commerce, Washington, D.C., 19 pp.
- \_\_\_\_\_, 1978: Satellite Activities of NOAA 1977. National Environmental Satellite Service, U.S. Dept. of Commerce, Washington, D.C., 21 pp.
- Park, S. U., D. N. Sikdar, and V. E. Suomi, 1974: Correlation Between Cloud Thickness and Brightness Using Nimbus 4 THIR Data (11.5  $\mu\text{m}$  Channel) and ATS 3 Digital Data. J. Appl. Meteor., 13, 402-410.
- Reynolds, D. W., and T. H. Vonder Haar, 1977: A Bispectral Method for Cloud Parameter Determination. Mon. Wea. Rev., 105, 446-457.
- Scoggins, J. R., et al., 1978: Mesoscale Characteristics of the Texas HIPLEX Area During Summer 1976. Final Report TWDB Contract No. 14-70020. Texas Department of Water Resources Publication No. LP-65, 343 pp.
- Smith, E. A., 1977a: Digital Imaging System used at Colorado State University. Interactive Video Displays for Atmospheric Studies, University of Wisconsin, 149-171.
- \_\_\_\_\_, 1977b: Private Communication. Dept. of Atmospheric Science, Colorado State University.
- Vonder Haar, T. H., 1970: Application of Simultaneous Infrared Radiation Measurements and Cloud Photographs from Satellite. J. Appl. Meteor., 9, 955-958.
- Waters, M. P., D. B. Miller, D. C. Dismachek, and R. M. Carey, 1977: Cloud Height and Change Analysis from Digital SMS/GOES Satellite Data. Preprints of Tenth Conference on Severe Local Storms, Omaha, Nebraska, American Meteorological Society, 42-47.